

---

# Magneto–Optical Effects from Band Topology in Kagome Magnets

---

Dissertation in Physics

for the degree Dr. rer. nat.  
at the University of Augsburg  
and Budapest University for Technology and Economics  
supervised by Sándor Bordács and István Kézsmárki

Submitted by  
**Felix Ludwig Schilberth**  
in August 2024



Date of the defense: 30.01.2025

Reviewer 1:	Prof. István Kézsmárki
Reviewer 2:	Prof. Christine Kuntscher
Reviewer 3:	Prof. Yoshinori Tokura

## Motivation

The characterisation of different states of matter through the mathematical discipline of topology is a relatively young field of solid state physics. Compared to the widely applied Landau theory which classifies condensed matter phases by an order parameter, spontaneously breaking underlying symmetries of the system, the topological classification relies on equivalence classes and the possibility to map the properties of different systems onto each other by small and slow (adiabatic) deformations, without inducing a quantum phase transition [1]. While the order parameter is a locally measurable quantity, e.g. the magnetisation, topological phases are distinguished by a global invariant, e.g. the Chern number. The first success of topology was the explanation of the integer quantum Hall effect in 1982 [2], while interest was significantly boosted after the year 2000 with the prospect of explaining the anomalous Hall effect in ferromagnets by both real- and momentum-space topological contributions [3, 4]. Focusing on electronic topology, subsequent theoretical efforts lead to the formulation of a periodic table of topological systems for gapped and gapless electronic phases depending on dimensionality and non-spatial symmetries [1], including topological insulators, Dirac and Weyl semimetals as well as topological superconductors. Although originally considered exotic phenomena, recent analysis estimates that more than 27% of known materials host some type of topological order [5]. Therefore, aside from potential technological applications in memory devices, spintronics and topological quantum computing [6, 7], investigating and engineering material systems which realise these quantum phases generates tremendous fundamental interest for understanding the interplay of single particle electronic properties, spin-orbit coupling, interacting (quasi)particles, magnetism and external stimuli such as strain and pressure or electromagnetic fields [8–10].

A material platform which provides an extremely versatile playground for the emergence and study of these phenomena is the kagome network. In this triangular lattice of corner sharing triangles, a plethora of exotic quantum states was theoretically predicted and experimentally observed, among them electronic and phononic flat-bands with enhanced correlations, charge density waves and topological superconductivity, as well as the quantum-spin-liquid state [8]. One of the earliest considered and most heavily investigated aspects is electronic topology under broken time-reversal symmetry, leading to a Chern insulator state and Weyl and nodal-line semimetals, for which the coupling with spin-orbit interaction produces highly unusual transport and optical properties that are the focus of this work.

Similar to the Haldane model for the quantum anomalous Hall state on the honeycomb lattice, imaginary hoppings also produce a quantised Hall conductance on a spin-chiral ferromagnetic kagome layer [11]. When such layers are stacked and coupled to form a 3D magnet, it can inherit the topological properties of its building block, resulting in a 3D topological-insulating or Weyl-semimetallic state [12]. This straightforward theoretical construction inspires the search for kagome lattice based materials realising these phases, although such realisations may be more complicated due to electronic correlations, finite-temperature effects or disorder. Central hallmarks of the presence of these states are the intrinsic

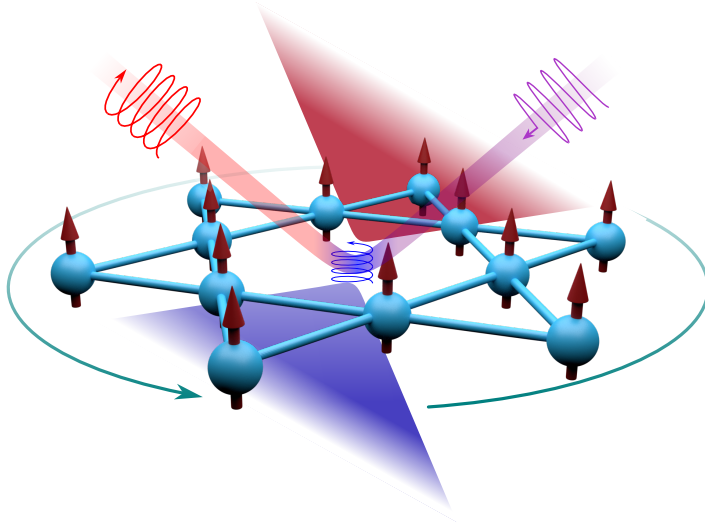


**Figure 1.**

Magneto–optical response in (gapped) kagome semimetals. Gapped linearly dispersing bands (dark blue and red) emerging from a magnetic kagome layer produce large anomalous Hall conductivity (green arrow) and optical activity, where incoming linear polarisation (purple) is turned elliptical upon reflection (red) with the other chirality (blue) absorbed by the bands (adapted from [8]).

anomalous Hall effect (AHE) and magneto–optical activity, which arise from the Berry curvature generated by the topological band structure in the presence of spin–orbit coupling. An artistic attempt to illustrate this concept is presented in Fig. 1. If generalised to finite frequencies, the two effects can be connected by the optical Hall conductivity which can be conveniently determined by measuring e. g. the magneto–optical Kerr effect (MOKE) in magnetic metals. Since the latter is experimentally accessible by analysing the polarisation state of light reflected from the surface of the kagome magnet, I use magneto–optical spectroscopy to investigate the topological properties of several kagome systems in this thesis.

The goals of this analysis are to (1) disentangle the AHE contributions of itinerant electrons and interband transitions to quantify the extrinsic and intrinsic proportions respectively, (2) from the multitude of bands for each material, identify the specific band structure features generating the intrinsic part to learn about the requirements for enhancing the anomalous response, (3) elucidate the role of spin–orbit coupling, (4) establish magneto–optical spectroscopy as a reliable tool to study topological band structures and to (5) monitor their variation through chemical pressure or external forces, e. g. doping or magnetic fields. The latter are predicted to provide an efficient control knob to vary the electronic band structure as both crystal symmetries and time–reversal may be altered by the applied field.

Along this line, the first chapter of this thesis shortly summarises the basic concepts of electronic topology and its implications for the response of kagome magnets, followed by an introduction to magneto–optical spectroscopy in Chapter 2. The last four chapters present the experimental results for a selection of kagome magnets. Chapters 3 and 5 investigate and compare the origin of the large AHEs in the archetypical kagome Weyl semimetal  $\text{Co}_3\text{Sn}_2\text{S}_2$  and the room temperature kagome magnet  $\text{Fe}_3\text{Sn}_2$ , while Chapters 4 and 6 respectively analyse how external magnetic fields manipulate the band structure in  $\text{Co}_3\text{Sn}_2\text{S}_2$  and how the peculiar metamagnetic phases of the kagome spin–ice material  $\text{HoAgGe}$  influence its magneto–optical response.

## Contents

<b>Motivation</b> . . . . .	<b>i</b>
<b>Table of Contents</b> . . . . .	<b>iv</b>
<b>List of Figures</b> . . . . .	<b>v</b>
<b>1. Electronic and Optical Properties of Topological Magnets</b> . . . . .	<b>1</b>
1.1. Electronic Topology in a Nutshell: The Su–Schrieffer–Heeger Model	1
1.2. Topological Properties of Kagome Magnets . . . . .	9
1.3. Signatures of Topology in Physical Observables . . . . .	16
<b>2. Experimental Methods for Magneto–Optical Spectroscopy</b> . . . . .	<b>25</b>
2.1. Infrared Spectroscopy . . . . .	25
2.2. Magneto–Reflection Experiments . . . . .	29
2.3. Magneto–Optical Kerr Effect Spectroscopy . . . . .	30
<b>3. Giant Magneto–Optical Response of a Nodal Line Resonance in</b> <b><math>\text{Co}_3\text{Sn}_2\text{S}_2</math></b> . . . . .	<b>39</b>
3.1. Reflectivity and Kerr Effect Spectra . . . . .	41
3.2. Optical Conductivity and its Anisotropy . . . . .	43
3.3. Decomposition of the Optical Hall Effect . . . . .	45
3.4. Fingerprints of the Nodal Line in the Conductivity Tensor . . . . .	47
<b>4. Field–Induced Reconstruction of the Nodal Loop in <math>\text{Co}_3\text{Sn}_2\text{S}_2</math></b> . . . . .	<b>49</b>
4.1. High–Field Magneto–Reflection Measurements . . . . .	51
4.2. Optical Conductivity in Magnetic Field . . . . .	52
4.3. Evolution of the Nodal Line . . . . .	53
<b>5. Signatures of a Helical Nodal Line in the Anomalous Hall Effect of</b> <b><math>\text{Fe}_3\text{Sn}_2</math></b> . . . . .	<b>57</b>
5.1. Reflectivity and MOKE Spectra . . . . .	59
5.2. Optical Conductivity Spectra . . . . .	59
5.3. Band and Momentum Decomposition . . . . .	62
5.4. Comparison and Outlook . . . . .	65
<b>6. Tracing Band Reconstructions across Metamagnetic Transitions in</b> <b><math>\text{HoAgGe}</math></b> . . . . .	<b>67</b>
6.1. Zero–Field Reflectivity . . . . .	70
6.2. Optical Conductivity and Conductivity Anisotropy . . . . .	71
6.3. Probing Metamagnetic States by Magneto–Reflection . . . . .	72
6.4. Optical Conductivity between the Plateau Phases . . . . .	74
<b>7. Summary</b> . . . . .	<b>77</b>
7.1. Thesis Points and Related Publications . . . . .	79
7.2. Full List of Publications . . . . .	80
<b>A. Appendix</b> . . . . .	<b>81</b>

<b>References</b> . . . . .	<b>91</b>
<b>Acknowledgements</b> . . . . .	<b>99</b>

## List of Figures

1.	Magneto–optical response in (gapped) kagome semimetals . . . . .	ii
1.1.	Schematic illustration of the Su–Schrieffer–Heeger model . . . . .	1
1.2.	Fully dimerised limits of the SSH model . . . . .	2
1.3.	Bands and edge states for a SSH model with 10 sites . . . . .	3
1.4.	Bulk band structure of the SSH model . . . . .	4
1.5.	Construction of a WSM from the SSH model . . . . .	5
1.6.	Bulk band structure of a WSM generalised from the SSH model . . . . .	5
1.7.	Band structure of a WSM ribbon . . . . .	6
1.8.	Band structures for different parameters $v, w_x$ and $w_y$ . . . . .	7
1.9.	$\mathbf{d}$ vector map for the WSM . . . . .	8
1.10.	The kagome network and its tight–binding band structure . . . . .	9
1.11.	Edge states on a kagome ribbon . . . . .	10
1.12.	Stacked TI model . . . . .	13
1.13.	Berry phase in the SSH–WSM . . . . .	14
1.14.	$AA$ –stacked kagome layers . . . . .	15
1.15.	Higher dimensional linear band degeneracies . . . . .	16
1.16.	$ABC$ –stacked kagome layers . . . . .	17
1.17.	The different contributions to the AHE . . . . .	17
1.18.	Weyl nodes in real materials . . . . .	19
1.19.	Frequency dependent Hall response of a Weyl node pair . . . . .	20
1.20.	The magneto–optical Kerr effect . . . . .	22
1.21.	Line shapes of the optical Hall effect . . . . .	23
2.1.	Working principle of a grating spectrometer . . . . .	27
2.2.	Schematic of a Bruker Vertex 80v FTIR for reflectivity measurements . . . . .	28
2.3.	Spectral artefacts for finite travel distance . . . . .	29
2.4.	Magneto–reflection setups . . . . .	30
2.5.	Lightpath for PEM–based MOKE spectroscopy . . . . .	31
2.6.	Polarisation modulation of the MOKE components . . . . .	32
2.7.	Exemplary calibrations for PEM measured MOKE components . . . . .	34
2.8.	Lightpath for FIR rotation measurements . . . . .	35
2.9.	Configuration of optical components for different frequency ranges . . . . .	36
2.10.	Summary of the MOKE spectroscopy setups . . . . .	37
3.1.	Topological properties of $\text{Co}_3\text{Sn}_2\text{S}_2$ . . . . .	40
3.2.	Reflectivities and Kerr parameters for $\text{Co}_3\text{Sn}_2\text{S}_2$ . . . . .	42
3.3.	Conductivity tensor for $\text{Co}_3\text{Sn}_2\text{S}_2$ . . . . .	44
3.4.	Momentum decomposition of the resonance in $\text{Co}_3\text{Sn}_2\text{S}_2$ . . . . .	46
3.5.	Optical anisotropy and Hall angle spectra of $\text{Co}_3\text{Sn}_2\text{S}_2$ . . . . .	47
4.1.	Symmetries and topology for in– and out–of–plane magnetic field in $\text{Co}_3\text{Sn}_2\text{S}_2$ . . . . .	50
4.2.	Magneto–reflectance in $\text{Co}_3\text{Sn}_2\text{S}_2$ . . . . .	51
4.3.	Magnetic field dependence of the conductivity spectra in $\text{Co}_3\text{Sn}_2\text{S}_2$ . . . . .	53

4.4. Evolution of the nodal loop upon reorienting the magnetisation to $\mathbf{M} \parallel a$ . . . . .	54
5.1. Topological properties of $\text{Fe}_3\text{Sn}_2$ . . . . .	58
5.2. Measured quantities for $\text{Fe}_3\text{Sn}_2$ . . . . .	60
5.3. Conductivity tensor elements for $\text{Fe}_3\text{Sn}_2$ . . . . .	61
5.4. Low-energy band and momentum decomposition for $\text{Fe}_3\text{Sn}_2$ . . . . .	63
5.5. Step edge band decomposition for $\text{Fe}_3\text{Sn}_2$ . . . . .	64
6.1. The peculiar transport properties of $\text{HoAgGe}$ . . . . .	68
6.2. Metamagnetic phases of $\text{HoAgGe}$ . . . . .	69
6.3. Reflectivity data for $\text{HoAgGe}$ . . . . .	70
6.4. Optical conductivity and anisotropy for $\text{HoAgGe}$ . . . . .	71
6.5. Magneto-reflectance data for $\text{HoAgGe}$ . . . . .	73
6.6. Magnetic field dependence of the conductivity spectra for $\text{HoAgGe}$ . . . . .	75
A.1. Evolution of the nodal loop upon reorienting the magnetisation to $\mathbf{M} \perp a$ . . . . .	82
A.2. Ground state MOKE spectra of $\text{HoAgGe}$ . . . . .	84

## Electronic and Optical Properties of Topological Magnets

This first chapter summarises the most important background information necessary to interpret the experimental results. In the first section, I give a short introduction to electronic topology and Weyl semimetals through a one-dimensional model and its generalisation. The second section describes the kagome lattice as a material platform and its topological properties. In the third section, we will see how the interplay of magnetic order and electronic topology influences transport properties and optical responses.

### 1.1 Electronic Topology in a Nutshell: The Su–Schrieffer–Heeger Model

Topological insulators (TIs) are one of the most heavily investigated material classes in the context of electronic topology. While being insulating in the bulk, they host conductive edge states as a direct consequence of their electronic band structure. The unusual properties of these edge states such as spin–momentum locking and the topological protection inspire applications, e. g. in next generation random access memory devices and topological quantum computing [6, 7]. The emergence of such a peculiar phase of matter can already be understood on the basis of a one-dimensional chain, the Su–Schrieffer–Heeger (SSH) model. The bulk part of this section introduces the model based on the lecture notes on TIs by Asbóth, Oroszlány and Pályi [13].

The SSH model is schematically illustrated in Fig. 1.1. It describes a finite one-dimensional lattice with  $N$  units, each consisting of two sites  $A$  and  $B$ . The remainder of the section is formulated for the choice of unit cell indicated by the dashed ellipse, for which electrons can hop between the two sites with an amplitude  $v$  within one unit cell, while they hop between two cells with  $w$ . Electron–electron interactions and the spin are neglected. For  $v \neq w$ , the hopping amplitudes are termed staggered and make the lattice bipartite. The blue and red shaded regions respectively indicate the left and right boundaries of the chain, potentially hosting edge states, meaning wavefunctions with highest weight at the boundary. In this setting, the single-particle real-space Hamiltonian is

$$\mathcal{H} = v \sum_{m=1}^N (|m, B\rangle\langle m, A| + h.c.) + w \sum_{m=1}^{N-1} (|m+1, A\rangle\langle m, B| + h.c.). \quad (1.1) \text{ SSH model}$$

The states  $|m, \alpha\rangle$  are labelled according to the lattice vectors via  $m \in 1, 2, \dots, N$  with the two different sites  $\alpha \in A, B$  and  $h.c.$  denotes the hermitian conjugate.

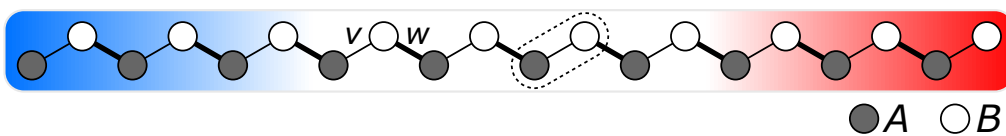
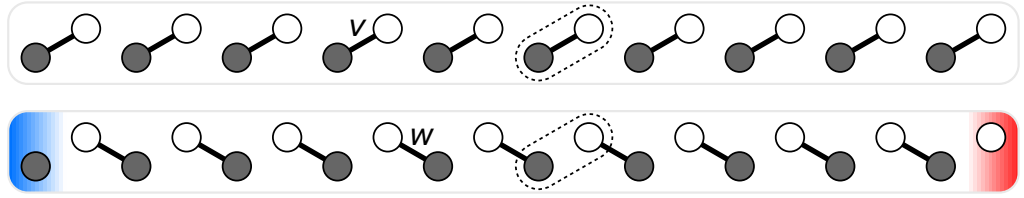


**Figure 1.1**

Schematic illustration of the Su–Schrieffer–Heeger model. Sites  $A/B$  are shown by grey/white circles [13].

**Figure 1.2**

Fully dimerised limits of the SSH model. Top: trivial limit  $v, w = 1, 0$ . Bottom: topological limit  $v, w = 0, 1$  with one edge state on each sublattice  $A$  (blue) and  $B$  (red) (adapted from [13]).



Before the evaluation of the Hamiltonian and the details of the electronic structure, let us investigate the possibility of edge states in the SSH model.

### 1.1.1 Edge States of the SSH model

In the SSH model, it is possible to give an intuitive picture of edge states by considering the fully dimerised limits of the chain and open boundary conditions. If either the intercell hopping  $v$  or intracell hopping  $w$  are set to zero, the chain breaks up into dimers, as illustrated in Fig. 1.2. The energy eigenstates are restricted to each dimer and are the even and odd superpositions of the states from each site with energies  $E = \pm 1$ , if the finite hopping amplitude is set to 1.

In the case  $w = 0$ , termed trivial limit, the Schrödinger equation becomes

$$\mathcal{H}(|m, A\rangle \pm |m, B\rangle) = \pm (|m, A\rangle \pm |m, B\rangle), \quad (1.2)$$

whereas in the so-called topological case,  $v = 0$ , the dimers are shared between two unit cells and we have:

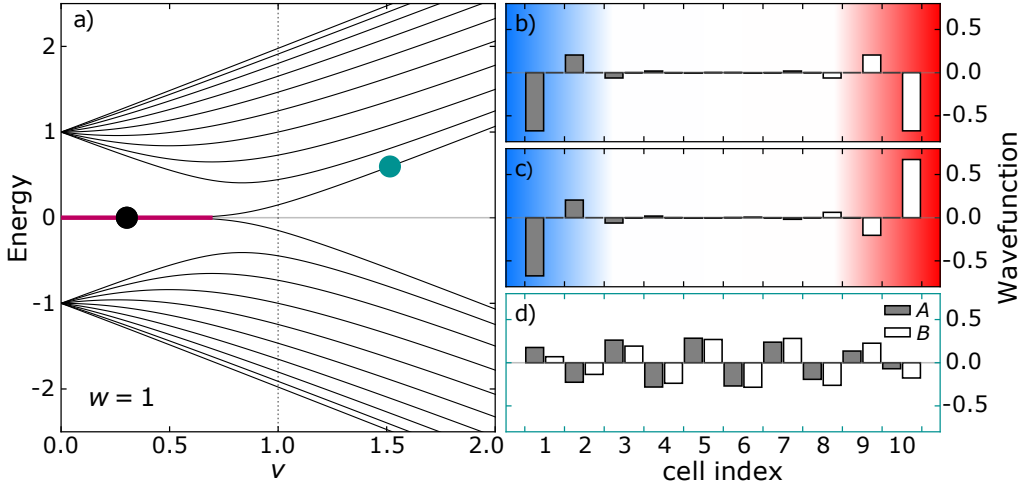
$$\mathcal{H}(|m, B\rangle \pm |m + 1, A\rangle) = \pm (|m, B\rangle \pm |m + 1, A\rangle). \quad (1.3)$$

However, this does not capture all states of the topological limit. At the boundaries, there are two states  $|1, A\rangle$  and  $|N, B\rangle$  which do not belong to any dimer and therefore form edge states. As we do not consider an onsite potential, these localised states have  $E = 0$ :

$$\mathcal{H}|1, A\rangle = \mathcal{H}|N, B\rangle = 0 \quad (1.4)$$

and therefore lie in the energy gap of the bulk states.

This property of the edge state persists even if we turn on a small  $v \neq 0$ . Figure 1.3 shows the energy of the states of an SSH model with 10 unit cells and  $w = 1$  as a function of  $v$ . The topological dimerised limit is obtained for  $v = 0$  in panel (a). For values of  $v \lesssim 0.75$ , we still obtain zero-energy edge states in the energy gap of the bulk as indicated by the purple line (doubly degenerate for edge states on each end). Here, states are coloured purple if they have dominant weight in the first four sites on each the edge, as illustrated in panels (b) and (c) which show the wavefunctions at the position of the black marker. Note, that the state on the left edge (blue) only has weight on the  $A$  sites, whereas the state on the right edge (red) is only non-zero on  $B$  sites, identical to the fully dimerised case. Since for  $v \neq 0$  the edge states are no longer sharply but exponentially localised on the boundaries, their wavefunctions hybridise forming symmetric and antisymmetric superpositions. The degeneracy of these states is lifted above a threshold value of  $v$ . At this point, where the gap is also closed, a topological phase transition occurs in the thermodynamic limit. If  $v$  gets even larger the chain becomes trivial. This case is indicated by the green marker in Fig. 1.3(a) for  $v > w$ . The states no longer have zero energy and they obtain bulk character, as shown in panel (d).

**Figure 1.3**

Bands and edge states for a SSH model with 10 sites. (a) Band structure for  $w = 1$  as function of  $v$ . The purple line indicates the presence of zero-energy edge states. (b,c) Wavefunctions of the two bands for the parameters at the black dot in (a) ( $v = 0.3$ ), showing the symmetric and antisymmetric hybridisation of the edge states on sublattices  $A$  (blue) and  $B$  (red). (d) Wavefunction for the point marked with green ( $v = 1.5$ ) with bulk character (adapted from [13]).

Note that the exact value of  $v$  where the states leave zero energy also depends on the system size  $N$ . For larger  $N$ , this point moves closer to  $v = w = 1$ .

From the above discussion, it seems that the energy of the edge state with respect to the bulk band gap plays an important role, so we will now consider the energy of the bulk states.

### 1.1.2 Bulk–Boundary Correspondence

From Eq. 1.1, we can obtain the bulk momentum–space Hamiltonian if we impose periodic boundary conditions. Then Eq. 1.1 becomes

$$\mathcal{H} = \sum_{m=1}^N (v|m, B\rangle\langle m, A| + w|(m \bmod N) + 1, A\rangle\langle m, B|) + h.c., \quad (1.5)$$

where the modulo operator  $\bmod$  closes the chain to a ring. In order to apply the Bloch–Theorem, it is necessary to split the basis  $|m, \alpha\rangle = |m\rangle \otimes |\alpha\rangle$  and represent the two–site basis by Pauli matrices

$$\sigma_x = \begin{pmatrix} 0 & 1 \\ 1 & 0 \end{pmatrix}, \quad \sigma_y = \begin{pmatrix} 0 & -i \\ i & 0 \end{pmatrix}, \quad \sigma_z = \begin{pmatrix} 1 & 0 \\ 0 & -1 \end{pmatrix}, \quad (1.6)$$

which delivers the bulk momentum–space Hamiltonian

$$\mathcal{H}(k) = \begin{pmatrix} 0 & v + we^{-ik} \\ v + we^{ik} & 0 \end{pmatrix} = \mathbf{d}(k)\hat{\sigma}. \quad (1.7)$$

The second equality introduces the  $\mathbf{d}$  vector representation, where  $\hat{\sigma}$  is a three–component vector with the three Pauli matrices and  $\mathbf{d}$  is given by

$$d_x(k) = v + w \cos k, \quad d_y(k) = w \sin k, \quad d_z(k) = 0. \quad (1.8)$$

This notation turns out to be useful, because the energy eigenvalues can be calculated from the absolute value of  $\mathbf{d}$ , as

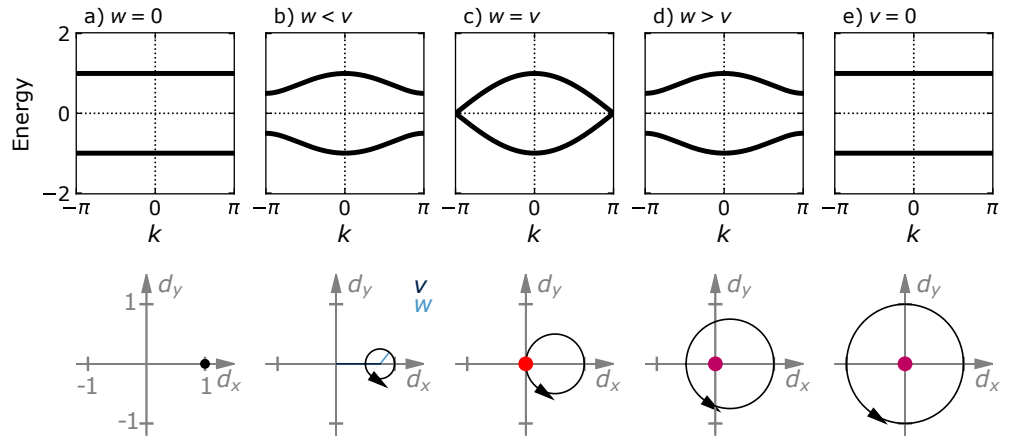
$$E(k) = \pm|\mathbf{d}(k)| = \pm\sqrt{v^2 + w^2 + 2vw \cos k} \quad (1.9)$$

and because  $\mathbf{d}(k)$  contains the topological information. It can be shown that the winding number  $\nu$  of the  $\mathbf{d}(k)$  vector around the origin of the  $d_x$ – $d_y$  plane is defined by

$$\nu = \frac{1}{2\pi} \int dk \left( \tilde{\mathbf{d}}(k) \times \frac{d}{dk} \tilde{\mathbf{d}}(k) \right)_z, \quad \text{with } \tilde{\mathbf{d}} = \frac{\mathbf{d}}{|\mathbf{d}|} \quad (1.10) \text{ Winding number}$$

**Figure 1.4**

Top row: Bulk band structure of the SSH model. For all parameter sets of  $v$  and  $w$ , two bands are obtained. Bottom row:  $\mathbf{d}$  vector representation for the same parameter sets. The red dot indicates that the origin lies on the loop for  $v = w$ , the purple dots highlight the origin within the loop (adapted from [13]).



and that it characterises the topological properties of the bulk. To illustrate this, Fig. 1.4 plots the energy eigenvalues and  $\mathbf{d}(k)$  for some combinations of  $v$  and  $w$ . From panel (a) to (e), we gradually move from the trivial to the topological limit of the SSH chain. For all cases of staggered hopping amplitudes, we obtain two bands with a distinct gap. For  $v = w$  in (c), the gap closes at the edge of the Brillouin zone (BZ), resulting in metallic behaviour.

In the bottom row, the corresponding  $\mathbf{d}(k)$  vectors are shown. We find that  $\mathbf{d}(k)$  traces a circle in the  $d_x$ - $d_y$  plane, whose centre is shifted along  $d_x$  by  $v$  and its radius is given by  $w$ , as indicated by the blue lines in panel (b). For the trivial (normal) insulators (NI) in Fig. 1.4(a) and (b), the circle lies far away from the origin of the plane resulting in  $\nu = 0$ . For the metallic case, the origin is a point on the circle indicated by the red dot and the winding number is undefined as  $|\mathbf{d}| = 0$ . In the TIs panel (d) and (e), the origin (purple dot) lies within the circle yielding  $\nu = 1$ .

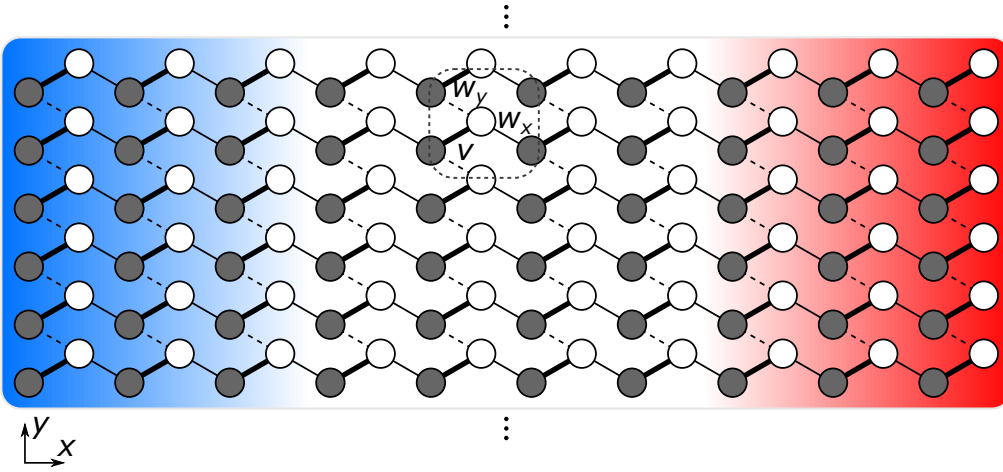
There are two important consequences from the above considerations: If (and only if) we find an edge state at the end of a finite SSH chain, we can immediately predict that the bulk winding number is non-zero and vice versa. This is an example for bulk-boundary correspondence of TIs, the topological information is always carried by both bulk and surface. Secondly, the transition from a TI to NI can only happen if the bulk band gap closes at some point in between. Therefore,  $\nu$  is a topological invariant which can only be changed if we induce a topological phase transition through a metallic state. Consequently, the edge states and winding number are protected by the bulk gap, leading to a strong robustness of these states against external forces, e. g. temperature, disorder or magnetic field, as long as the gap remains open. For the SSH model, this protection is ensured by the lattice being bipartite, represented by the existence of a chiral symmetry operation

$$\sigma_z \mathcal{H} \sigma_z = -\mathcal{H}. \quad (1.11)$$

This symmetry connects the two sites of the unit cell and forces the energy bands to be symmetric with respect to the Fermi energy. This requires  $d_z = 0$ , excluding e. g. different onsite potentials on sites  $A$  and  $B$ , which forces the  $\mathbf{d}$  vector to lie in the  $d_x$ - $d_y$  plane. This ensures that  $\nu$  is properly defined.

However, there are phases of matter, termed topological semimetals, where the bulk gap closes at distinct points in the BZ and we observe surface states nonetheless. This behaviour can also be understood based on the SSH model if we extend the dimension of the model to 2D.

## Topological protection

**Figure 1.5**

Construction of a WSM from the SSH model. Nearest neighbour SSH chains are coupled with an interchain hopping  $w_y$  between sites  $A$  and  $B$ . The dots at the top and bottom indicate extension to a ribbon (adapted from [13]).

### 1.1.3 Two–Dimensional Generalisation: Weyl–Semimetals

We can obtain a two–dimensional lattice model if we couple several SSH chains with a nearest–neighbour interchain hopping  $w_y$  (the former  $w$  becomes  $w_x$ ). This construction is illustrated in Fig. 1.5. Importantly, the interchain hopping again only connects two different sites  $A$  and  $B$ , so the lattice remains bipartite and the chiral symmetry defined in Eq. 1.11 is preserved. The corresponding bulk momentum–space Hamiltonian is obtained by extending Eq. 1.7 with  $w_y$  and  $k_y$

$$\mathcal{H}_{\text{WSM}}(\mathbf{k}) = \begin{pmatrix} 0 & v + w_x e^{-ik_x} + w_y e^{-ik_y} \\ v + w_x e^{ik_x} + w_y e^{ik_y} & 0 \end{pmatrix} = \mathbf{d}_{\text{WSM}}(k_x, k_y) \hat{\sigma}, \quad (1.12)$$

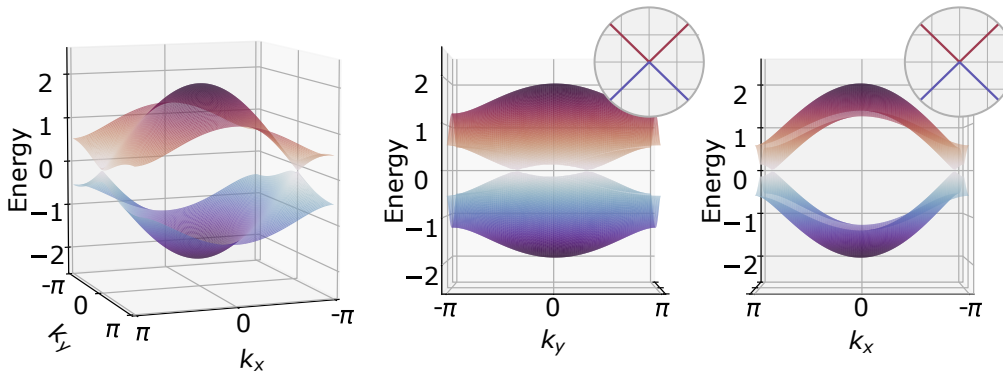
with the associated  $\mathbf{d}_{\text{WSM}}(k_x, k_y)$  vector

$$d_x = v + w_x \cos k_x + w_y \cos k_y, \quad d_y = w_x \sin k_x + w_y \sin k_y, \quad d_z = 0. \quad (1.13)$$

If  $w_y = 0$ , the system breaks apart into individual SSH chains, which depending on  $v$  and  $w_x$  can be either trivial or topological with a sharp transition at  $v = w_x$ . Most interestingly, we investigate the influence of a small  $w_y$  on a topological chain with  $v = 0.7$  and  $w_x = 0.9$  in the following. First, we can calculate the energy eigenvalues presented in Fig. 1.6.

We obtain two bands which are fully gapped except at two isolated points in the BZ where they touch each other. Their position can be best estimated from the axis projections. In the vicinity of these points termed as Weyl nodes the dispersion is linear as highlighted in the insets. As it will turn out later, the Weyl nodes, characteristic of the Weyl–semimetallic (WSM) phase, are topologically

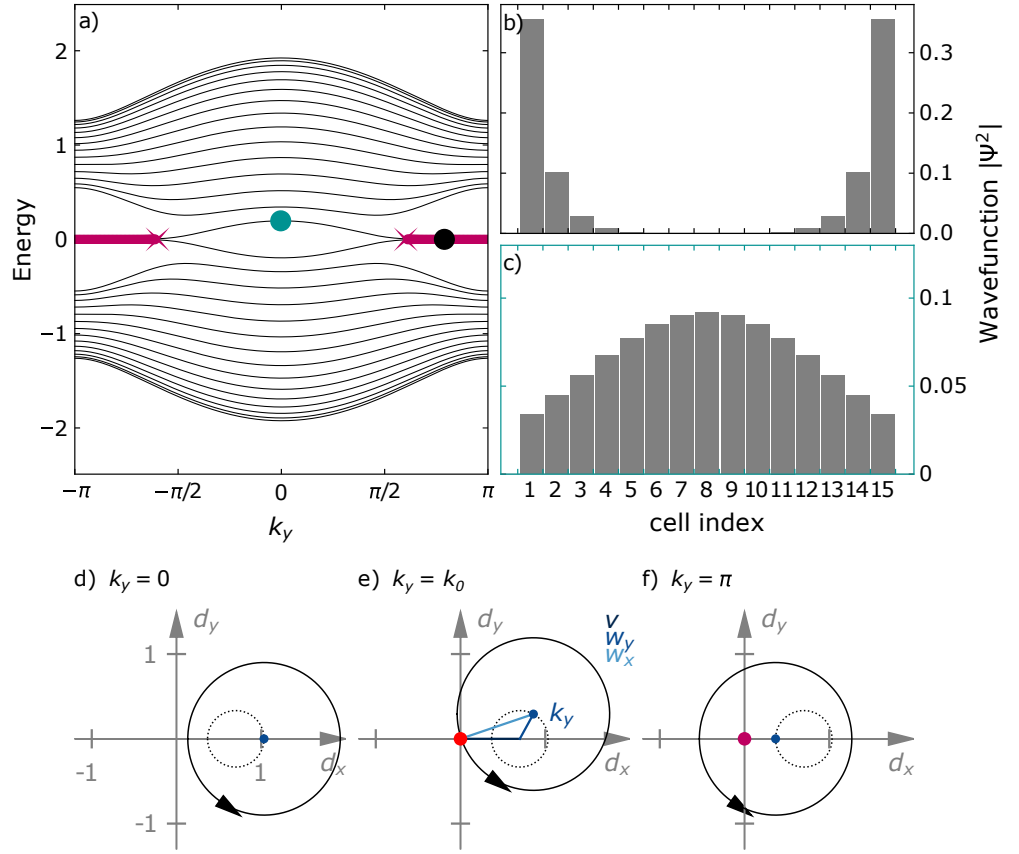
**Weyl node**

**Figure 1.6**

Bulk band structure of a WSM generalised from the SSH model for the parameters  $v, w_x, w_y = 0.7, 0.9, 1/3$ . Two gap closing points with linear dispersion (Weyl nodes) are obtained close to the BZ edge. The insets show cuts through these points (adapted from [13]).

**Figure 1.7**

Band structure of a WSM ribbon along  $k_y$  for the parameters  $v, w_x, w_y = 0.7, 0.9, 1/3$  for a width of 15 unit cells (a). Bands are coloured in purple if their wavefunction resides in the first 40% of sites counted from the edges. Around the edge of the BZ ( $k_y = \pm\pi$ ), a zero-energy edge state is obtained. Panel (b) shows the absolute square of the corresponding wavefunction at the black dot. In the BZ centre ( $k_y = 0$ ), there are no edge states (panel (c), green dot). (d–f) Corresponding  $\mathbf{d}$  vector representation at different  $k_y$ . The lengths of the hoppings are indicated by the blue lines in panel (e). The small dashed circle represents the path of the centre of the solid circle (small blue dot) as a function of  $k_y$ . (d)  $k_y = 0$ : The solid circle does not contain the origin, it is a NI. (e) The origin (red dot) lies on the solid circle, resulting in a closing of the gap (Weyl point). (f) The origin is contained in the solid circle, case of a TI (adapted from [13]).



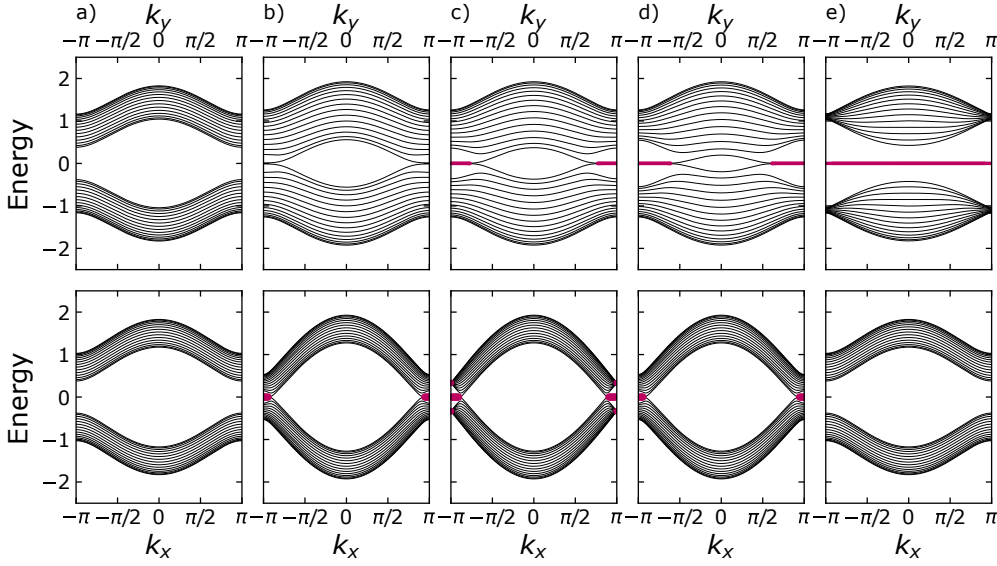
protected. These quasiparticles have their analogues in high energy physics, where Hermann Weyl proposed a model for chiral massless Fermions [14]. In the 3D case, the model reads

$$i\partial_t\Psi_{\pm} = \mathcal{H}_{\pm}\Psi_{\pm} \quad (1.14)$$

$$\mathcal{H}_{\pm} = \mp\mathbf{p} \cdot \hat{\sigma} \quad (1.15)$$

where the momentum operator  $\mathbf{p}$  can be either parallel or antiparallel to the spin defining a chirality for the Weyl Fermion. This property is associated with the notion of spin–momentum locking [9]. Although these particles have not been found isolated in nature, the linearly dispersing bands we have obtained produce quasiparticles with the corresponding properties in solids which will be investigated in this thesis.

Returning to the SSH–WSM, the bands are derived from topological SSH chains, so it is likely that edge states also exist here. In order to evaluate their presence, the band structure is calculated on a ribbon of finite width, as shown in Fig. 1.7. In this plot, bands are coloured in purple if their wavefunction is located within the first 40% of sites counted from the edges. This is the case for the zero-energy bands close to the BZ edge ( $k_y = \pm\pi$ ). An exemplary wavefunction at the black dot is shown in panel (b). In contrast, the same band has bulk character in the BZ centre (green dot, wavefunction in panel (c)). From this consideration, it seems that the system is either a NI or TI depending on the value of  $k_y$ . The two regions come in contact at the two points highlighted by crosses which are the Weyl nodes.

**Figure 1.8**

Band structures for  $w_y = 1/3$  and (a–e)  $v = [1.1, 0.9, 0.8, 0.7, 0.4]$   $w_x = [0.4, 0.7, 0.8, 0.9, 1.1]$ . States coloured in purple have more than 40% weight on the edges (compare Fig. 1.7). Panels (a) and (e) respectively show NI and TI phases, while (b–d) are Weyl semimetals with finite Fermi arcs (adapted from [13]).

In order to understand this behaviour, we can again consider the winding number of the  $\mathbf{d}_{\text{WSM}}(k_x, k_y)$  vector shown in Fig. 1.7(d–f). The values of the hopping parameters are indicated by the blue lines in panel (e). In Eq. 1.13,  $k_x$  describes a circle with radius  $w_x$  that is represented by the large solid circle in the figures. Its centre (small blue dot) is shifted from the origin by  $v$  and lies on the circle of  $k_y$  with radius  $w_y$ , indicated by the dashed line. For  $k_y = 0$  (panel (d)), the origin lies outside of the solid circle as in the case of a NI with  $\nu = 0$ . For  $k_y = k_0$  in (e), the origin is a point on the solid circle (red dot). Same as for the SSH chain, this results in a gap closing, here forming a Weyl node. In (f), the origin lies within the circle, yielding a TI with  $\nu = 1$ . The result is an edge state which spans only part of the BZ connecting the two Weyl nodes and is therefore termed as Fermi arc.

From the  $\mathbf{d}$  vector maps, we can deduce the different phases of this model. For  $w_x < v - w_y$ , the large circle can never contain the origin for any  $k_y$ , so the system is a NI. If  $v - w_y < w_x < v + w_y$  we obtain the WSM state described above whereas for  $v + w_y < w_x$  the system is a TI. In summary:

$$\begin{aligned} w_x < v - w_y & \quad \text{Trivial insulator} \\ v - w_y < w_x < v + w_y & \quad \text{Weyl–semimetal} \\ v + w_y < w_x & \quad \text{Topological insulator.} \end{aligned}$$

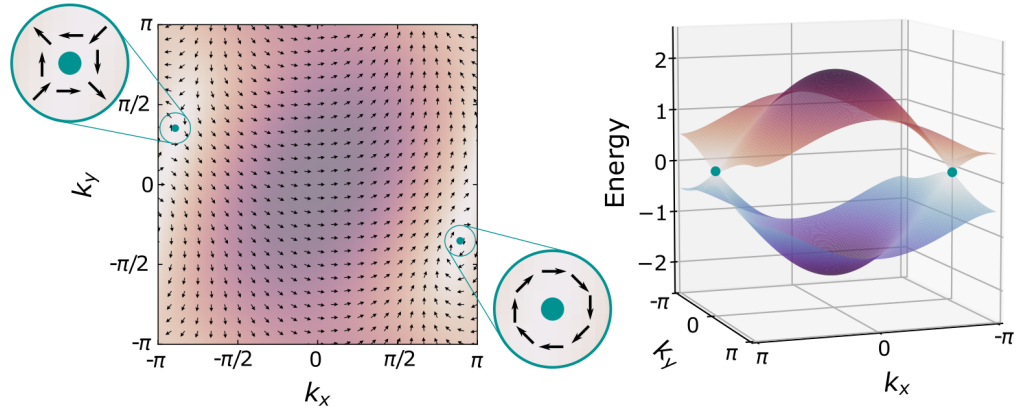
In order to illustrate the behaviour of the Fermi arcs for these cases, the band structure for several hopping parameters is plotted in Fig. 1.8. In panel (a), a NI without edge states is obtained. In (b), surface states appear on the edge of the BZ which expand towards the BZ centre in (c) and (d), all three corresponding to WSM states. Finally, the two arcs merge at  $k_y = 0$  resulting in a TI for (e). In the bottom row, only small fractions of surface states appear along  $k_x$  because  $v > w_y$  for all cases, leading to trivial chains.

As we see, the positions of the Weyl nodes change depending on the hopping parameters. They can be calculated from the condition  $\mathbf{d}(K_x, K_y) = 0$  (compare the triangle in Fig. 1.7(e)) which gives the defining equations

$$\begin{aligned} 0 &= v + w_x \cos K_x + w_y \cos K_y \\ 0 &= w_x \sin K_x + w_y \sin K_y. \end{aligned}$$

**Figure 1.9**

$\tilde{\mathbf{d}}$  vector map for the WSM with the parameters  $v, w_x, w_y = 0.7, 0.9, 1/3$ . The green dots mark the positions of the Weyl nodes calculated from Eq. 1.16. The insets show a magnified view of the local structures around the nodes. For the left node, the winding number is  $-1$ , for the right one  $+1$  leading to different topological charges (adapted from [13]).



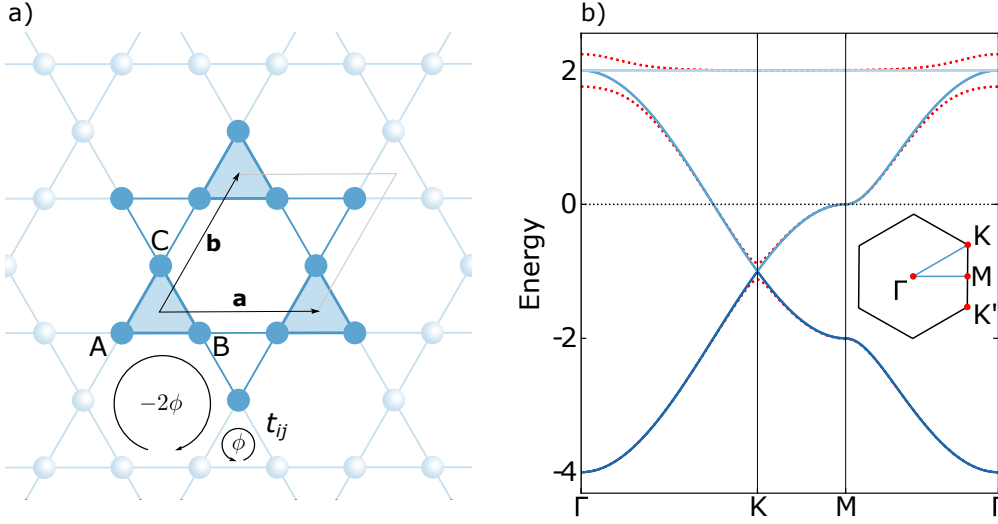
The solutions are

$$\begin{aligned}\cos K_x &= \frac{w_y^2 - v^2 - w_x^2}{2vw_x} \\ \cos K_y &= \frac{w_x^2 - v^2 - w_y^2}{2vw_y}.\end{aligned}\quad (1.16)$$

There is a second node, which due to inversion symmetry is located at  $(-K_x, -K_y)$ , so importantly, the total number of Weyl nodes is even. In Fig. 1.8(b), a pair of Weyl nodes is created at the BZ edge, which then travel through the BZ as we tune the hoppings and then annihilate with each other in (e). Aside from the symmetry consideration (which is not a necessary condition), this behaviour has an underlying topological reason that can be illustrated by plotting the  $\tilde{\mathbf{d}}$  vector in the  $k_x$ - $k_y$  plane as depicted in Fig. 1.9. For comparison, the bulk band structure is shown on the right. The green dots mark the positions of the Weyl nodes as calculated from Eq. 1.16. The overall vector field is rather featureless, except for two vortices around the position of the nodes. The insets magnify the local structures. The winding numbers around the nodes can be determined with a simple experiment: Take a finger and let it point in the direction of one of the arrows. Now go around the node anticlockwise and adjust your finger to the direction of the arrows one after the other. For the left node, this will rotate the finger one full turn in a clockwise direction, for the right node it will be anticlockwise, revealing integer winding numbers of  $-1$  and  $+1$ , respectively. This property is directly linked to opposite chiralities of the Weyl-quasiparticles. Their sum has to be zero, since the total winding number has to be conserved (zero as in the NI case where no nodes are present), leaving only the possibility to create nodes in pairs with opposite winding numbers. Consequently, these winding numbers serve as topological charges which protect the nodes, making an annihilation with the opposite partner the only possibility to reduce the number of nodes. This doubling theorem was originally proven by Nielsen and Ninomiya [15].

### Topological charge

Although the SSH model is conceptually simple, we have seen fundamental properties of topological matter. Ensured by bulk-boundary correspondence, protected edge states are a benchmark of the presence of non-trivial electronic topology. A WSM is an intermediate phase between NI and TI that can be created by stacking topologically non-trivial building blocks. For interchain hopping values in the specified range, this results in Fermi arcs spanning only part of the BZ and connecting pairs of nodes with opposite chiralities/topological charges.

**Figure 1.10**

The kagome network and its tight-binding band structure. (a) Unit cell of the kagome lattice with unit vectors  $\mathbf{a}$  and  $\mathbf{b}$  of the triangular lattice and the shaded triangles indicate the three-atomic basis. The parameters of the tight-binding model are illustrated. (b) Band structure of the kagome lattice for  $t_{ij} = t = -1$  and  $\phi = 0$ . Three bands are obtained, two of which form a 4-fold degenerate linear band crossing (Dirac point) at K (and K') and one band is flat (blue,  $\lambda_{SO} = 0$ ). The band degeneracies are gapped by  $\lambda_{SO} = 0.1$  (red dotted). The inset shows the hexagonal BZ with the high-symmetry points [11, 20].

In the above considerations, the topological features rely on the lattice models being bipartite, therefore possessing chiral symmetry [1, 13]. In general, if global symmetries like inversion and/or time-reversal are present, they force bands to be degenerate by an even number, e. g. by Kramer's theorem, thus Weyl points cannot appear as the minimal degeneracy of a band crossing would be four. Hence, in the scope of this thesis, we will consider systems with broken time-reversal symmetry when we investigate magnetic materials based on the kagome network.

## 1.2 Topological Properties of Kagome Magnets

Named after an Asian weaving pattern, the kagome lattice receives much attention in modern solid state physics as it can host a variety of quantum phenomena, ranging from frustrated magnetism over superconductivity to topological insulators and semimetals [16–18]. The general structure is presented in Fig. 1.10(a), showing its triangular Bravais lattice with three atoms in the basis. Since the structure is closely related to the honeycomb lattice, a linear band crossing is obtained at the K and K' points of the hexagonal BZ in a simple tight-binding model shown in panel (b), protected by inversion and time-reversal symmetry. Including spin, this crossing is a 4-fold degenerate Dirac point without chirality and does not possess a Fermi arc, compared to the formerly discussed Weyl nodes. In addition, there is a third, completely flat band emerging due to destructive interference of electron wavefunctions living on this peculiar lattice [19]. We will consider the topological properties of this system in the following.

### 1.2.1 Chern Insulators and Berry Phase

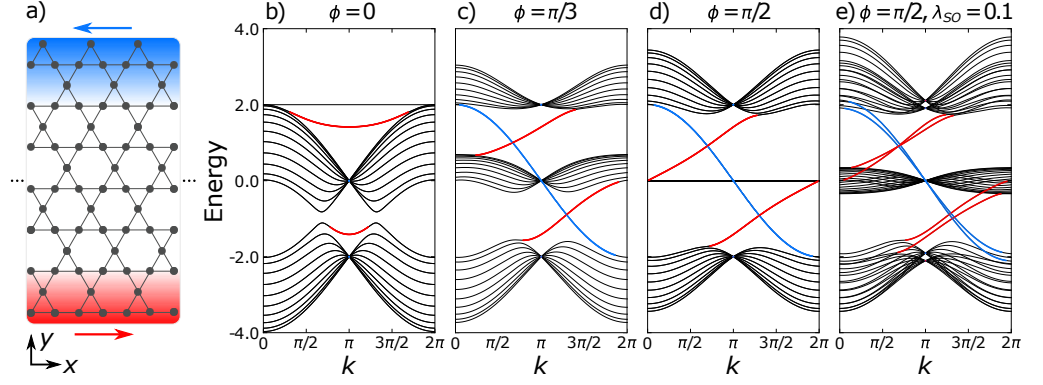
The Hamiltonian used for Fig. 1.10 reads as

$$\mathcal{H} = \sum_{\langle i,j \rangle, \sigma} t_{ij} e^{i\phi_{ij}/3} c_{i,\sigma}^\dagger c_{j,\sigma} + i\lambda_{SO} \sum_{\langle i,j \rangle} \left( c_{i,\uparrow}^\dagger c_{j,\uparrow} - c_{i,\downarrow}^\dagger c_{j,\downarrow} \right). \quad (1.17)$$

The angular bracket denotes nearest neighbours and  $c_{i,\sigma}^\dagger/c_{j,\sigma}$  are electron creation/annihilation operators on site  $i/j$  with spin  $\sigma$ ,  $t_{ij} = t$  is the hopping

**Figure 1.11**

Edge states on a kagome ribbon with 10 unit cells. (a) Schematic of the ribbon, (b–e) Band structures for  $t = -1$  for different values of  $\phi$  and  $\lambda$ . The states coloured in blue/red are located within the top/bottom 20% of sites. For  $\phi \neq 0$ , edge states are present in the bulk band gap with blue/red states always having negative/positive slopes, resulting in unidirectional electron propagation as indicated by the arrows in panel (a). Spin-orbit coupling lifts the degeneracy, but does not gap the edge states [21].



amplitude and  $\phi_{ij} = \phi$  is a geometric phase factor. The second term introduces Kane–Mele spin–orbit coupling which gaps all band touching points at  $\Gamma$  and  $K$  (red-dotted lines in Fig. 1.10(b)) [11, 20, 21]. Conceptually, the complex hopping amplitude may be induced by non-collinear magnetic order with canted local spins on each site  $A$ – $C$  interacting with the electron. If it hops along a closed loop, e.g.  $A \rightarrow B \rightarrow C \rightarrow A$ , its wavefunction obtains an additional phase  $\phi$  which encodes the vector potential induced by the three local moments via their scalar spin chirality hence breaking time–reversal symmetry [11].

In order to illustrate the effects of the complex phase  $\phi$ , Fig. 1.11 plots the band structure of a ribbon with 10 unit cells along  $y$  for different values of  $\phi$ . Panel (a) shows a schematic of the ribbon from the kagome lattice with the top and bottom edges coloured in blue and red. In (b–e), states are respectively coloured if their weight lies within the top or bottom 20% of sites on the ribbon. In (b) with  $\phi = 0$ , two edge states are present, but they do not lie in the bulk band gap centred around  $E = -1$ . If the Fermi energy is in the gap, the system therefore is a NI. Cases (c) and (d) are different: For  $\phi \neq 0$ , time–reversal symmetry is broken which gaps the Dirac crossing and we find edge states in both bulk band gaps. Hence, we obtain TIs for accordingly tuned Fermi energy. Due to the broken time–reversal symmetry in 2D, this class of TIs are called Chern insulators. In (e), finite spin–orbit coupling is included which breaks the degeneracy, but is unable to gap the edge states, illustrating their robustness.

As we have seen in the SSH model, the presence of edge states predicts a bulk topological invariant by bulk–boundary correspondence, which we need to find for a Chern insulator. To do so, we can take a look at the evolution of the state of the electron if it propagates through the vector potential of the local spins. Its state vector will acquire a phase factor  $e^{i\gamma_n}$ , called Berry phase [22, 23], which for a path  $\partial S$  in a general parameter space spanned by coordinates  $\mathbf{s}$  can be written as

$$\text{Berry phase} \quad \gamma_n = \int_{\partial S} d\mathbf{s} \cdot \mathcal{A}_n(\mathbf{s}), \quad (1.18)$$

where  $\mathcal{A}_n(\mathbf{s})$  is termed the Berry connection or Berry vector potential defined by

$$\begin{aligned} \mathcal{A}_n(\mathbf{s}) &= i\langle n(\mathbf{s}) | \nabla_{\mathbf{s}} | n(\mathbf{s}) \rangle \\ &= i\langle n, \mathbf{k} | \nabla_{\mathbf{k}} | n, \mathbf{k} \rangle \quad \text{for Bloch electrons.} \end{aligned} \quad (1.19)$$

The states  $|n(\mathbf{s})\rangle$  form a complete orthonormal basis for the Hamiltonian  $\mathcal{H}(\mathbf{s})|n(\mathbf{s})\rangle = \varepsilon_n(\mathbf{s})|n(\mathbf{s})\rangle$  [23]. In our example, this can be the evolution of Bloch states  $|n, \mathbf{k}\rangle$  in the BZ, in which case  $n$  becomes the band index and  $\mathbf{s}$  is the crystal momentum  $\mathbf{k}$ . If we now integrate the Berry phase for a closed loop, its state vector will come back to the original point, hence  $\gamma_n = 2\pi \cdot C_n$  with  $C_n \in \mathbb{Z}$ . The Chern number  $C_n$  is the topological invariant we are looking for: It is zero for a NI, but finite in the TI. It can be calculated directly for each band via

$$C_n = \frac{1}{(2\pi)^2} \int_{\text{BZ}} \mathcal{B}_n(\mathbf{k}) d^2\mathbf{k}, \quad (1.20) \text{ Chern number}$$

where we write the Berry phase as a flux density rather than a vector potential, which leads to the definition of the Berry curvature

$$\mathcal{B}_n(\mathbf{s}) = \nabla_{\mathbf{s}} \times \mathcal{A}_n(\mathbf{s}), \quad (1.21)$$

$$\mathcal{B}_n(\mathbf{k}) = \nabla_{\mathbf{k}} \times i \langle n, \mathbf{k} | \nabla_{\mathbf{k}} | n, \mathbf{k} \rangle, \quad (1.22)$$

inspired by Stokes theorem  $\int_{\partial S} \mathcal{A} ds = \int_S \nabla_{\mathbf{s}} \times \mathcal{A} d^2\mathbf{s}$  [13].

Let us evaluate this invariant for the bands of the kagome model in Fig. 1.11(c) and (d), where the integration is performed over the entire BZ. Importantly, the Chern number is properly defined only if the bands are separated by gaps, so in the present example, we can evaluate this number for the three groups of overlapping bands centred around  $E \approx 2, 0, -2$  (upper, middle, lower). It can be shown that the sum of Chern numbers for the middle bands is always zero, irrespective of  $\phi$ , while for the upper and lower bands

$$C_{\text{upper, lower}} = \pm \text{sgn}(\sin \phi) \quad (1.23)$$

holds, resulting in  $C_{\text{upper, lower}} = \pm 1$  for (c) and (d) [11]. Hence, if the Fermi energy lies in a gap, the sum of Chern numbers of the occupied bands is always 1 which is the reason for the existence of edge states. This is a characteristic behaviour of a Chern insulator [13]. Compared with the zero-energy edge states in the SSH model, we now obtain dispersive behaviour, hence these states contribute to conduction which we investigate in the following.

### 1.2.2 Quantum Anomalous Hall Effect

For all energies in the band gaps of the Chern insulators in Fig. 1.11, we find a pair of edge states residing on opposite sides of the bulk. Interestingly, the blue bands always have a negative slope while it is positive for the red states. Since the group velocity of the electron wave can be calculated by  $\mathbf{v}_n = 1/\hbar \partial E_n / \partial \mathbf{k}$ , the electrons which are confined to the edge propagate in a unidirectional conduction channel, as indicated by the arrows in panel (a). This is a direct consequence of broken time-reversal symmetry in this system, which prohibits the inversion of the velocity.

If we also make the sample finite in the  $x$  direction, a single channel forms which circles all around the full edge of the system. Now we apply an electric field  $\mathbf{E}$  to the system. This will modify the group velocity resulting in

$$\mathbf{v}_n = \frac{1}{\hbar} \frac{\partial E_n(\mathbf{k})}{\partial \mathbf{k}} - \frac{e}{\hbar} \mathbf{E} \times \mathcal{B}_n(\mathbf{k}) \quad (1.24)$$

where the second term is denoted as anomalous velocity [23]. The Berry curvature takes the role of a fictitious magnetic field, leading to a perpendicular component

of the velocity as in the normal Hall effect. This is one key how topological phenomena can manifest in physical quantities [3, 10]. As a result, we can calculate the Hall conductivity for our two-dimensional example which yields

### Quantum anomalous Hall effect

$$\sigma_{xy} = \frac{e^2}{h} \int_{\text{BZ}} \frac{d^2\mathbf{k}}{(2\pi)^2} \mathcal{B}_n(\mathbf{k}) = \frac{e^2}{h} \cdot C_n, \quad (1.25)$$

expressing a conductance quantised by the Chern number in units of the conduction quantum  $e^2/h$ . This is known as the quantum anomalous Hall effect (QAHE) [23, 24]. In contrast to the quantum Hall effect of a 2D electron gas which relies on the Landau quantisation in very clean samples, no external fields are required here as the conductivity is directly encoded in the band structure of the system.

In summary, an individual kagome layer with broken time-reversal symmetry can host a Chern insulating phase with topologically protected, unidirectional edge states which manifest in physical observables like the off-diagonal conductivity via the Berry curvature. As a side note, the Berry phase can also be defined in real-space and is non-zero e.g. in non-collinear magnets showing spin chirality as in skyrmion lattices. The Hall effect arising from these real-space structures is generally termed topological Hall effect (THE).

Similar to the discussion of the SSH model, we now have a  $n$ -dimensional TI. In Sec. 1.1.3, we have seen that it is possible to construct a  $n + 1$ -dimensional WSM from such a system by stacking and coupling which we will next consider for 2D layers.

### 1.2.3 From Chern-Insulators to Weyl-Semimetals

A minimal model for the formation of a magnetic WSM from stacked TI layers was proposed by Balents and Burkov [12, 25]. The general setup is a multilayer heterostructure of TIs and NIs, shown in Fig. 1.12(a).

Each of the TI layers possesses 2D Dirac surface states which determine the low-energy properties, e.g. they could be Chern insulators. First, let us take a look at a single TI layer that can be described by

$$\mathcal{H} = v_F \tau^z (\hat{z} \times \boldsymbol{\sigma}) \cdot \mathbf{k} + \Delta_S \tau^x + b \sigma^z, \quad (1.26)$$

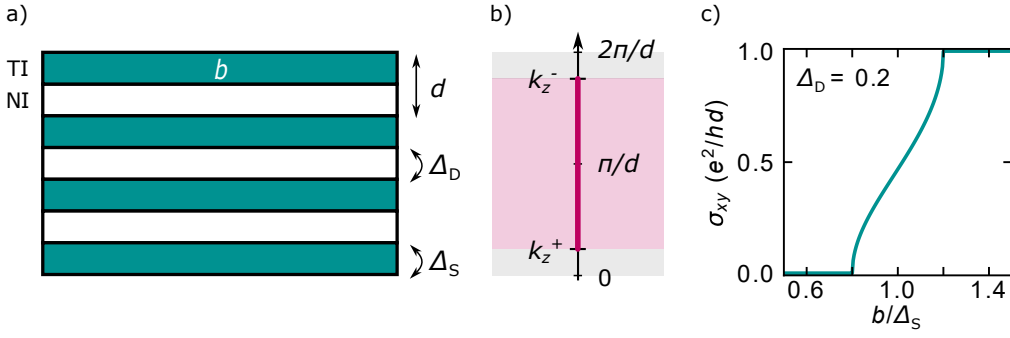
where  $v_F$  is the Fermi velocity of the Dirac nodes,  $\boldsymbol{\sigma}$  are the Pauli matrices for the spin,  $\hat{z}$  is the surface normal.  $\Delta_S$  is the intralayer hopping amplitude from the top to the bottom surface which are allocated to the second set of Pauli matrices  $\boldsymbol{\tau}$ , while  $b$  denotes the spin exchange splitting, hence the corresponding term breaks time-reversal symmetry. This can be brought to a diagonal form, yielding

$$\mathcal{H}_{\pm} = v_F (\hat{z} \times \boldsymbol{\sigma}) \cdot \mathbf{k} + m_{\pm} \sigma^z \quad (1.27)$$

which describes massive 2D Dirac Fermions with effective masses  $m_{\pm} = b \pm \Delta_S$  and hence a gap between positive and negative energy bands [25]. If the Fermi energy lies in that gap, the system has a Hall conductivity of

$$\sigma_{xy}^{\pm} = \frac{e^2}{2h} \text{sgn}(m_{\pm}). \quad (1.28)$$

If the TI layers are Chern insulators, this corresponds to a Chern number of  $\pm 1$  by comparison with Eq. 1.25. The factor  $1/2$  is included to resolve contributions from the top and bottom surface. If the gap closes for  $m_{\pm} = 0$  and reopens

**Figure 1.12**

Stacked TI model. (a) The model and its parameters. (b) Weyl nodes at  $k_z^\pm$  and their connecting Fermi arc (purple). To show a continuous arc,  $k$  values beyond the first BZ are used. The purple/grey shades indicate topological/trivial regions. (c) Quantum Hall phase transition as function of  $b/\Delta_S$  (adapted from [9, 12]).

below this critical ratio of  $b/\Delta_S$ , this conductivity vanishes resulting in a NI. This behaviour is identical to what we have seen for the SSH model in Fig. 1.4, with a direct transition from a NI to TI through a metallic state at one critical point. In the present case this is accompanied by a quantum Hall transition from  $\sigma_{xy} = 0$  to  $\sigma_{xy} = e^2/h$ .

Now we turn to the stack and couple different TI layers with NI spacers with a hopping amplitude  $\Delta_D$  across them along the stacking direction  $z$  and a total periodicity  $d$ , as shown in Fig. 1.12(a). This modifies the above Hamiltonian to

$$\mathcal{H} = v_F \tau^z (\hat{z} \times \boldsymbol{\sigma}) \cdot \mathbf{k} + [\Delta_S + \Delta_D \cos(k_z d)] \tau^x - \Delta_D \sin(k_z d) \tau^y + b \sigma^z \quad (1.29)$$

which after diagonalisation again yields Eq. 1.27, but with a modified mass  $m_\pm = b \pm \sqrt{\Delta_S^2 + \Delta_D^2 + 2\Delta_S \Delta_D \cos(k_z d)} = b \pm \Delta(k_z)$ . Because of the explicit  $k_z$  dependence, the critical value of  $b/\Delta(k_z)$  can now be reached for certain points  $k_z^\pm$  in the BZ, yielding Weyl nodes for

$$k_z^\pm d = \pi \pm k_0 = \pi \pm \arccos\left(\frac{\Delta_S^2 + \Delta_D^2 - b^2}{2\Delta_S \Delta_D}\right), \quad (1.30)$$

if  $|\Delta_S - \Delta_D| < b < \Delta_S + \Delta_D$ . These points are depicted in Fig. 1.12(b) ( $k_x = k_y = 0$ ). Again, this resembles what we have seen in Fig. 1.8: For  $b$  smaller than the lower critical value, the system is a NI. At this value, two Weyl nodes form at  $k_z = \pi/d$  which travel through the BZ in opposite direction upon increasing  $b$  until they annihilate at the higher critical value at  $k_z = 0$ . So again, the WSM phase broadens the transition from NI (grey) to TI (purple region). This broadening is also reflected in the Hall conductivity which is shown in Fig. 1.12(c). As before,  $\sigma_{xy} = 0$  in the trivial phase, while it takes the value of  $e^2/hd$  of a 3D-TI for large  $b$ . It can be shown that in the WSM phase, the conductivity takes the value of

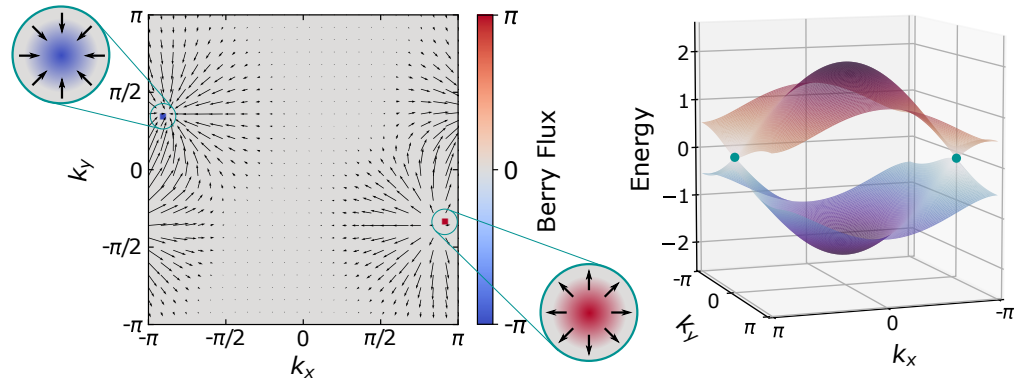
$$\sigma_{xy} = \frac{e^2}{h} \frac{k_0}{\pi} \quad (1.31)$$

and therefore depends only on the momentum-space separation  $2k_0$  of the nodes, making the conductivity vary continuously between the two critical values [25]. Consequently, in the search for topological semimetals with large anomalous Hall response, a large Weyl node separation is desirable.

We expect that the separated nodes span a Fermi arc in the surface BZ (purple line in Fig. 1.12(b)) which becomes the surface state of the 3D-TI at the higher critical value of  $b$ . Hence, if we consider a plane for any  $k_z$  in the purple region, e. g.  $\pi/d$ , we find a topological charge of 1 for the occupied band, so the 2D Hamiltonian representing that plane is a 2D-TI. Similarly, for any  $k_z$  in the grey region (e. g.  $k_z = 0$ ), the charge is 0 and the 2D Hamiltonian trivial. Consequently,

**Figure 1.13**

Berry phase in the SSH–WSM. Two Berry phase hot spots of opposite sign are present in the system, exactly at the locations of the Weyl nodes. The band structure is shown for comparison. The vector field displays the distribution of Berry curvature, though smoothed significantly to make the local structures visible. Consequently, one of the nodes is a source, the other a sink of Berry curvature.

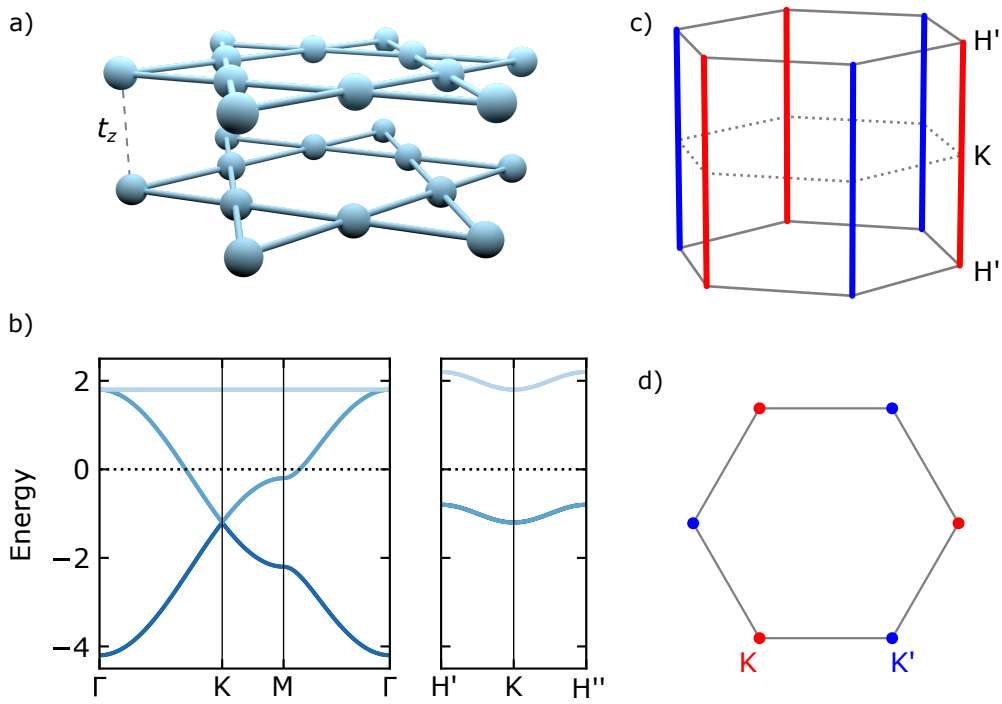


a source of Berry curvature must lie between these two planes accounting for this difference which is provided by the presence of a Weyl point [9]. To gain intuition, we can reconsider the WSM based on the SSH model from Sec. 1.1.3 and calculate the distribution of Berry curvature in the 2D–BZ. This is shown in Fig. 1.13. The Berry flux (integrated Berry phase per plaquette) is zero everywhere in the BZ, except for the position of the Weyl nodes, where it takes the value of  $\pi$  with opposite sign for the two nodes. This reveals the opposite topological charge of the nodes and the doubling theorem discussed before, now in the language of Berry phase [15]. The vector map shows the corresponding Berry curvature, but significantly smoothed so that the local structures are resolved. As a result, one of the nodes is a sink, the other a source of Berry curvature. Fig. 1.13 also shows that if we integrate over the entire BZ as we did for the Chern insulator, the sum of the topological charges adds up to zero. Consequently, if we consider a gapless semimetal, we have to look at isolated Fermi surfaces to determine topological charges, thus integrating only locally in their vicinity [1]. Hence, we get charges of  $-1$  for the blue and  $+1$  for the red node when integrating on a circle (a sphere in 3D) around each node, respectively. Comparing with the expression for the anomalous velocity in Eq. 1.24, this shows that the Weyl points can be interpreted as monopoles of the fictitious magnetic field in momentum–space, thus we expect signatures of the nodes in transport properties which we will consider in Sec. 1.3 [9, 10].

Summing up, we have found that a 3D–WSM phase can emerge from stacked 2D–TI layers. Its Hall conductivity takes a transitional value between the NI and TI phase and is determined by the separation of the nodes acting as momentum–space monopoles of Berry curvature. So far, we have investigated these topological properties purely theoretically. Regarding material realisations, the shandite  $\text{Co}_3\text{Sn}_2\text{S}_2$  was proposed to be a WSM generated by stacking kagome Chern insulator layers, similar to the above considerations [18]. We will investigate the magneto–optical response of this compound in Chapters 3 and 4. However, it turns out that this is not the only possibility to create a 3D topological semimetal from kagome layers, so we will consider another option next.

### 1.2.4 Nodal Line Semimetals

As a starting point, let us use simple kagome layers with in–plane hopping  $t$  ( $\phi = 0$ ,  $\lambda_{\text{SO}} = 0$ ) and stack them along the  $z$  direction such that the lattice sites are aligned. This results in a so–called *AA*–stack as shown in Fig. 1.14(a), where nearest neighbour hopping  $t_z$  from  $A \rightarrow A$ ,  $B \rightarrow B$ ,  $C \rightarrow C$  is used

**Figure 1.14**

*AA*-stacked kagome layers. (a) Structure with in-plane hopping  $t = -1$  and out-of-plane hopping  $t_z = 0.1t$ . (b) In-/out-of-plane band structure. (c) Hexagonal BZ, the coloured points mark where the lower two bands touch. (d) 2D projection along  $k_z$ . The 4-fold degenerate band touching persists all along  $H'-K-H''$ , forming a straight nodal line (adapted from [26]).

for coupling, preserving the hexagonal symmetry. For weak interlayer hopping  $t_z = 0.1t$ , the in-plane band structure in panel (b) is unmodified, still showing the Dirac node at the  $K$  point. However, the out-of-plane dispersion reveals that this degenerate point persists along  $k_z$ , following the  $H'-K-H''$  line. The same behaviour is obtained at  $K'$ . As a result, the red and blue colours in panels (c) and (d) indicate where the lower two bands touch. Consequently, we do not obtain a 0D isolated node, but a 1D nodal line [26].

This is one example how to obtain higher dimensional nodal features in a simple lattice model. In general, it is even possible to obtain 2D nodal planes, as Fig. 1.15 summarises. Because of their higher dimensionality, these extended crossings usually require additional protecting symmetries. While the simple 0D nodes are generically stable as long as translation symmetry is preserved [1], the stability of nodal lines and planes requires additional crystal symmetries such as mirror planes or even non-symmorphic screw axes as in the case of MnSi [27, 28]. Thus, when perturbations like spin-orbit coupling or symmetry breaking external fields are included, these features can be gapped out completely, e. g. to a TI phase, or leave a set of 0D nodes behind, resulting in a WSM. Nevertheless, the former nodal feature can concentrate Berry curvature even when gapped, as long as the gap is not too large [26]. Thus, they can still contribute significantly, e. g. to anomalous Hall conductivity.

As long as the protecting symmetry is preserved, changing other symmetries can at most alter the shape of the nodal line. An illustrative example is shown in Fig. 1.16. Compared to the *AA*-alignment of kagome planes, now the electrons from the *A* site of one layer can only hop to *B* and *C* sites on the neighbouring plane, resulting in an *ABC*-stack, as displayed in panel (a). This reduces the symmetry from hexagonal to rhombohedral, but for better comparability we keep using the hexagonal reciprocal unit cell. In contrast to the *AA*-stack, this stacking order also modifies the in-plane band structure displayed in panel (b). The former flat band acquires a dispersion and the two lower bands are gapped

### Nodal line semimetal

along  $H'-K-H''$ . Nevertheless, the band crossing survives as it is shifted away from  $K$  and  $K'$  points towards  $M$ . As shown in panel (c), this shift is  $k_z$ -dependent thus produces a nodal line which winds helically around  $H'-K-H''$ . The 2D projection in panel (d) reveals that the winding direction is opposite for  $K$  and  $K'$  as result of these points being time-reversed partners. When magnetic order and spin-orbit coupling are included, these lines are gapped to a quantum anomalous Hall insulating or WSM phase for out-of-plane/in-plane ferromagnetic moments, respectively [26]. So again, we can obtain a 3D topological semimetal from a stack of kagome layers. A material for which this mechanism was suggested to produce topological properties is  $Fe_3Sn_2$ , where kagome bilayers form an  $ABC$ -stack. Due to the bilayer nature, each  $K$  and  $K'$  point hosts a double helix formed by two nodal lines [26]. We will investigate the optical response of this peculiar feature in Chapter 5.

So, in order to understand the experimental signatures of the discussed topological band structures, we will next consider which observables can be influenced by topological states in magnetic materials.

### 1.3 Signatures of Topology in Physical Observables

In the previous section we have already seen at several points that non-trivial band topology can leave signatures in the Hall conductivity. Although the theoretical considerations leading to these signals are relatively straightforward in simple models with only few bands, their direct experimental observation may be challenging in actual material systems, so we review these effects in more detail in the following. In addition, we will see that magneto-optical responses are closely related and that their investigation can provide additional insight into the topological properties.

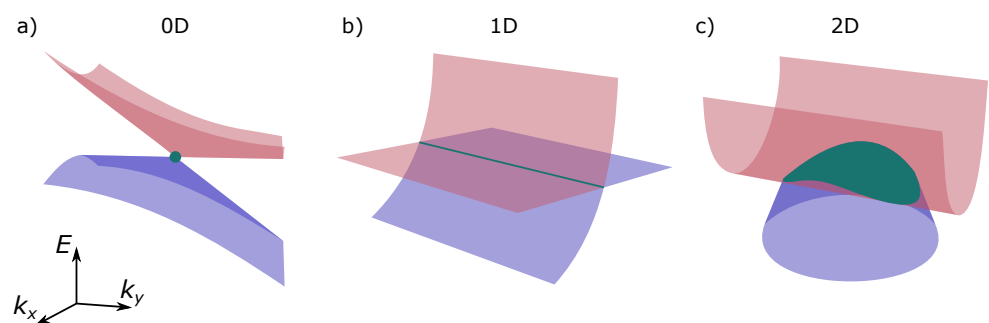
#### 1.3.1 Anomalous Hall Effect

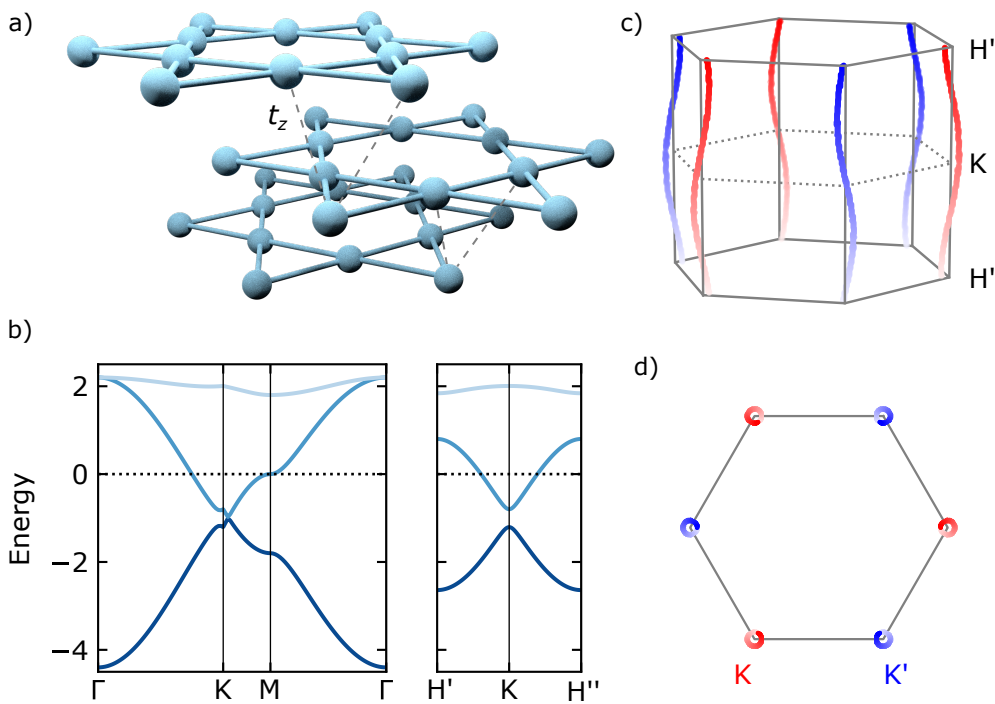
During his experiments on electric transport in magnetic field in conducting materials, Edwin Hall found that the emergent transverse voltage, subsequently termed Hall effect, is about one order of magnitude larger in ferromagnetic iron than in non-magnetic materials [29]. The general configuration is shown in Fig. 1.17(a). In a non-magnetic metal, the Hall resistivity  $\rho_{xy}$  scales linearly with the external field  $H$ , while it shows saturation in ferromagnets due to the magnetisation  $M$ , which leads to an additional Hall constant

$$\rho_{xy} = R_0 H + R_s M. \quad (1.32)$$

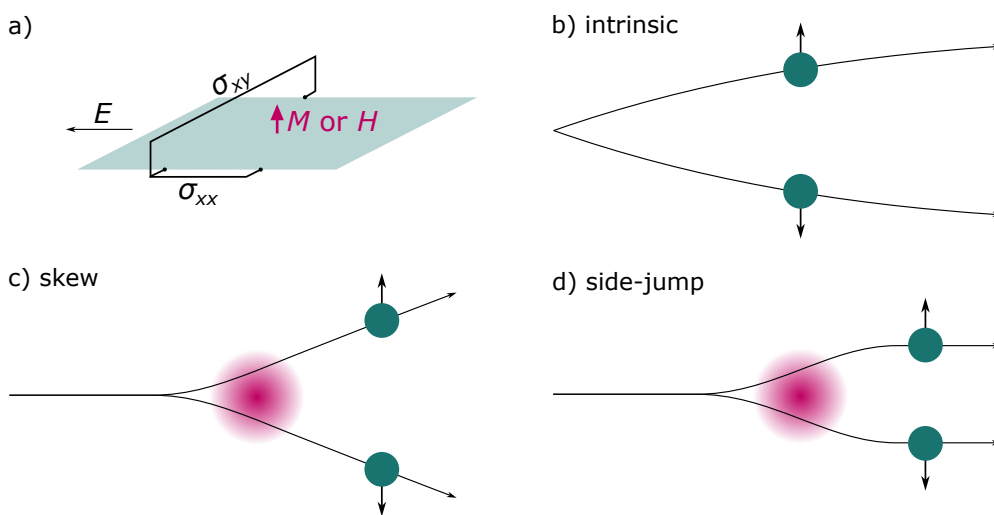
**Figure 1.15**

Higher dimensional linear band degeneracies. The point node (a) can be generalised to a 1D nodal line (b) or even a 2D nodal plane (c). At every point marked in green, the two bands touch with linear dispersion.



**Figure 1.16**

*ABC*-stacked kagome layers. (a) Structure with in-plane hopping  $t = -1$  and out-of-plane hopping  $t_z = 0.1t$ . (b) In-/out-of-plane band structure. (c) Hexagonal reciprocal unit cell, the coloured points mark where the lower two bands touch. (d) 2D projection along  $k_z$ . The 4-fold degenerate band touching winds around the  $H'-K-H''$  line. For the *ABC*-model, the band touching is shifted away from the K point, resulting in a nodal line winding along  $k_z$  in a helical fashion. The 2D-projection shows circles around K and the slight colour gradient reveals the opposite winding direction for K and K' (adapted from [26]).

**Figure 1.17**

The different contributions to the AHE. (a) General geometry of a Hall effect measurement. (b) Intrinsic (Berry phase) contribution. Magnetic impurities (diffuse purple) can lead to spin dependent extrinsic scattering of electrons (green) via skew (c) or side-jump mechanisms (d) (adapted from [3]).

This unusual behaviour coined the term anomalous Hall effect (AHE). Because of the quantum mechanical nature of this phenomenon and the underlying topological mathematical framework, it took until the change of millennia to develop a physical understanding. Based on the review by Nagaosa *et al.* [3], we will summarise the most important concepts in the following.

Experimental studies on magnetic metals indicated that the anomalous Hall resistivity should depend on the diagonal resistivity  $\rho_{xx}$  by a power law  $R_s \propto \rho_{xx}^\beta$ . One main source of the AHE involves skew scattering from magnetic impurities as proposed by Smit [30]. This mechanism predicts  $\beta = 1$  for  $\sigma_{xy}^{\text{skew}}$ . A second possibility  $\sigma_{xy}^{\text{sj}}$  was introduced by Berger which considers side-jumps of scattered electrons leading to  $\beta = 2$  [31]. Both are extrinsic mechanisms as they rather depend on impurities than on intrinsic material properties. A first attempt to describe the unusual nature of the AHE from band theory was performed by Karplus and Luttinger [32], who found that electrons in a perfect crystal with

applied electric field acquire a perpendicular velocity in the presence of spin–orbit coupling, predicting an exponent  $\beta = 2$ . Consequently, it is not possible to distinguish e. g. intrinsic and side–jump contributions solely by static magneto–transport experiments. Later, this finding could be equivalently reformulated in the framework of Berry curvature, yielding the anomalous velocity from Eq. 1.24. Because it depends only on the crystal Hamiltonian, this is termed the intrinsic contribution  $\sigma_{xy}^{\text{int}}$  to the AHE. All three mechanisms are summarised in Fig. 1.17(b–d). Since there may exist other scattering sources and in order to unambiguously define the above mechanisms, it is convenient to look at their dependence on the lifetime  $\tau$  of the Bloch state. While the intrinsic mechanism does not depend on the lifetime, skew scattering is defined as the linearly dependent contribution  $\propto \tau$ . Historically, all other dependencies and possible contributions are summarised under the side–jump conductivity, which therefore contains also other microscopic possibilities beside the mechanism from panel (d) [3].

If a material possesses a large anomalous Hall conductivity, it is therefore usually unclear whether the dominant mechanism is intrinsic or extrinsic. Magneto–transport experiments can give a first indication but require phenomenological scaling functions, which analyse the dependence of the Hall conductivity on the diagonal conductivity by a power law [33, 34], but their applicability may depend on sample properties or quality. A more rigorous decomposition of the AHE can be obtained by taking a closer look at the definition of the intrinsic conductivity which in the linear response framework can be calculated directly employing the Kubo formula

$$\begin{aligned} \text{Intrinsic AHE} \quad \sigma_{xy}^{\text{int}} &= e^2 \hbar \sum_{n,n'} \int \frac{d\mathbf{k}}{(2\pi)^3} \frac{\langle n, \mathbf{k} | p_x | n', \mathbf{k} \rangle \langle n', \mathbf{k} | p_y | n, \mathbf{k} \rangle}{(\epsilon_n(\mathbf{k}) - \epsilon_{n'}(\mathbf{k}))^2} \cdot (f_n(\mathbf{k}) - f_{n'}(\mathbf{k})) \\ &= -\frac{e^2}{\hbar} \sum_n \int \frac{d\mathbf{k}}{(2\pi)^3} f_n(\mathbf{k}) \mathcal{B}_n^z(\mathbf{k}), \end{aligned} \quad (1.33)$$

where the second identity makes the relation to the Berry curvature explicit [3].  $|n, \mathbf{k}\rangle$  denote the occupied Bloch state with eigenenergy  $\epsilon_n(\mathbf{k})$ , the connected Fermi function  $f_n(\mathbf{k})$  and the momentum operators  $p_{x,y}$ . The above equation contains information about interband transitions at finite energies, the static intrinsic Hall effect is therefore defined as the zero–energy extrapolation of this response. In this thesis, we will employ this definition experimentally by measuring

**Optical Hall effect** the optical Hall effect  $\sigma_{xy}(\omega)$  with broadband magneto–optical spectroscopy. This allows experimental application of the Kramers–Kronig relation

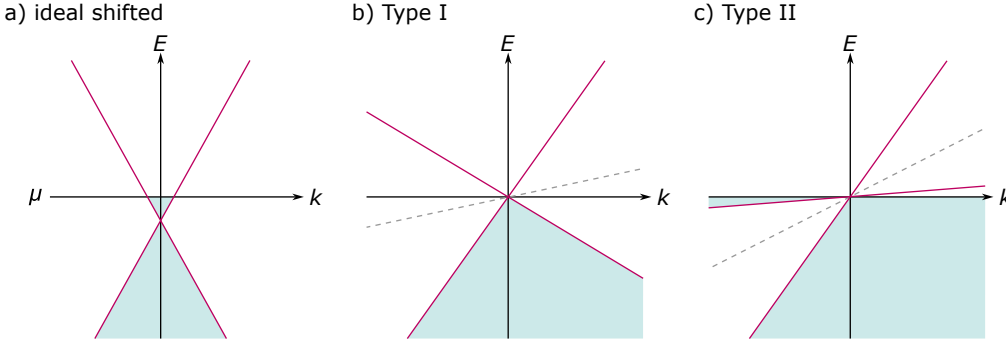
$$\text{Re } \sigma_{xy}(0) = \frac{2}{\pi} \mathcal{P} \int_0^\infty d\omega' \frac{\text{Im } \sigma_{xy}(\omega')}{\omega'} \quad (1.34)$$

with the angular frequency of the light  $\omega$  and thereby a separation of the intrinsic Hall conductivity from extrinsic scattering mechanisms which only involve conduction electrons at the Fermi level.

Previously, we have only determined the static intrinsic AHE response of a WSM (Fig. 1.12), so naturally the question arises how the frequency dependent response looks like.

### AHE of WSMs

In a previous section, we have found that the dc AHE response of a WSM takes the form of Eq. 1.31. This is valid for a pair of identical nodes which are located

**Figure 1.18**

Weyl nodes in real materials. (a) Symmetric Weyl cone described by  $\mathbf{p} \cdot \hat{\sigma}$  with the degenerate point shifted away from the Fermi energy. The green shading indicates the filled states. (b) Type I WSM: The term  $p_0 \cdot \mathbb{1}$  introduces a tilt of the cone which in the extreme case (c) turns to a type II WSM with electron and hole pockets on either side of the degeneracy (adapted from [36]).

directly at the Fermi level. If we include a finite interband response in this setting, the frequency dependent Hall conductivity takes the form

$$\text{Re } \sigma_{xy}(\omega) = \frac{e^2 k_0}{h\pi} + \frac{e^2}{6v_F^2 h\pi} \frac{k_0}{k_c^2 - k_0^2} \omega^2 \quad (1.35)$$

showing an  $\omega^2$  dependence [35].  $v_F$  is the Fermi velocity and  $k_c$  is a cutoff wavevector measured from the position of the node along the node separation. These terms can be considered as a “universal” AHE response of a WSM since they only depend on the separation of the nodes  $k_0$ .

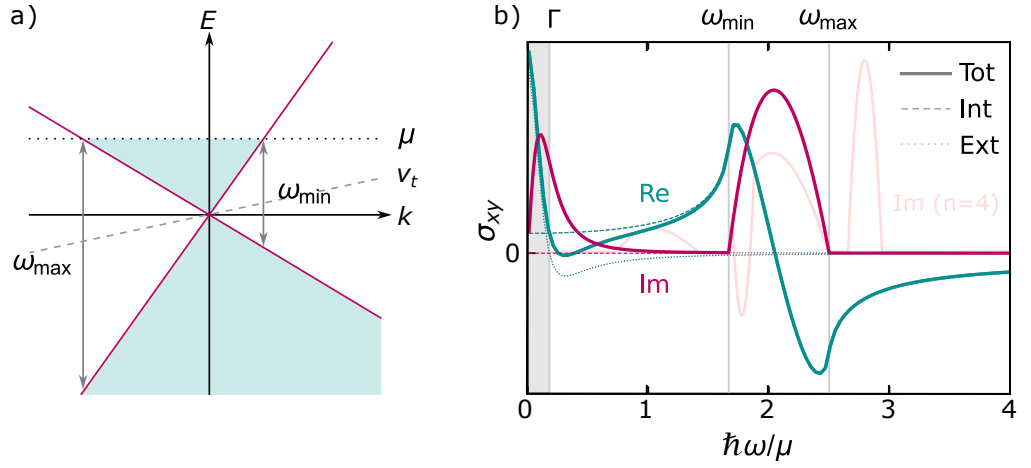
However, it turns out that for real materials, the above situation is highly idealised. Therefore, we need to take a look at more general characteristics of Weyl nodes first. So far, we were investigating systems whose low-energy physics could be described by the Weyl points of the form introduced by Eq. 1.15. In a general material, the bands which form the Weyl node do not necessarily have to lie at the Fermi energy, but the degenerate point can be shifted away by a chemical potential  $\mu$ . In addition, the ideal symmetric form of the node dictated by  $\mathbf{p} \cdot \hat{\sigma}$ , as shown in panel (a) of Fig. 1.18, is not protected in a lattice. For example, crystal field anisotropy can lead to an additional term  $p_0 \cdot \mathbb{1}$  which introduces a tilt of the Weyl cone as illustrated in panel (b). This version is termed type I WSM with the symmetric node being one representative. In extreme cases, the cone can be overtilted producing an electron and hole pocket on either side of the node (panel c), leading to a finite Fermi surface and a type II WSM [9]. Since the tilt and shift together produce different frequency scales on either side of the node, it is especially interesting to investigate interband transitions, as we will see in the following.

We consider a single type I Weyl node which is shifted from the Fermi level in energy by  $\mu$ , as sketched in Fig. 1.19 [37]. Due to the tilt, the free states on the two sides of the node become accessible at different energies  $\omega_{\min}$  and  $\omega_{\max}$ . They can be calculated using  $\hbar\omega_{\min,\max} = 2\mu/(1 \pm |\alpha_t|)$  with the tilt parameter  $\alpha_t = v_t/v_F$  where  $v_t$  is the tilt velocity, determined e.g. from the dashed line in panel (a) [36]. As a result, the node is type I (type II) if  $|\alpha_t| < 1$  ( $> 1$ ). The resulting intrinsic anomalous Hall response for a pair of nodes with opposite tilt and same chemical potential are shown in Fig. 1.19(b) by the dashed spectra (Int). The imaginary part is

$$\text{Im } \sigma_{xy}(\omega) = \text{sgn}(\alpha_t) \frac{e^2 \omega}{6h v_F} \left[ \frac{1}{\alpha_t^2} \left( \frac{1}{8} - \frac{\mu}{2\hbar\omega} + \frac{\mu^2}{2\hbar^2 \omega^2} \right) - \frac{1}{8} \right], \quad \omega_{\min} < \omega < \omega_{\max} \quad (1.36)$$

**Figure 1.19**

Frequency dependent Hall response of a type I Weyl node pair with  $\alpha_t = \pm 0.2$ . (a) Band structure under consideration. The green shading indicates the filled states according to the chemical potential  $\mu = 1$ . Due to the tilt, two frequencies  $\omega_{\min}$  and  $\omega_{\max}$  exist where Pauli-blocking is overcome. (b) Intrinsic off-diagonal response for these nodes (Int), extrinsic contributions below the scattering rate  $\Gamma$  (Ext) shaded in grey and total optical Hall effect (Tot) spectrum (adapted from [37, 39, 40]).



and zero everywhere else [36]. This can be intuitively understood by viewing it as the dissipative part of the response. In the interval  $\omega < \omega_{\min}$ , all transitions are blocked due to the Pauli principle, so no absorption is possible. Because of Onsager symmetry, the Hall response is odd in momentum relative to the node  $\sigma_{xy}(\omega, \mathbf{k}) = \sigma_{yx}(\omega, -\mathbf{k})$  and consequently, the contributions above  $\omega_{\max}$  cancel upon integration [37]. Hence, the only finite response comes from the intermediate region where the transitions to unoccupied states are not symmetric in  $\mathbf{k}$ . This is also the reason why this term does not appear for the ideal symmetric node [38]. The sign of the peak is determined by the product of signs of the chemical potential, the tilt parameter and the chirality. If the Weyl nodes differ in chemical potential and tilt, the total response is the sum of the individual nodes. As an example, the faint purple line in panel (b) is the response of a system of four nodes with arbitrary combination of parameters ( $\mu = 0.5, 0.9, 1, -1.4$ ,  $\alpha_t = 0.3, 0.05, 0.2, 0.05$  and  $\chi = 1, -1, 1, -1$ ) [37]. In this respect, the contribution of a nodal line can be viewed as a sum of individual nodes, depending on the evolution of the tilt and chemical potential along the line. The results for type II Weyl nodes are omitted here for brevity, but may be found in Ref. 36.

The real part can be calculated by Kramers–Kronig transformation and has a static and a frequency dependent component as

$$\begin{aligned}
 \text{Re } \sigma_{xy}(\omega) &= \text{Re } \sigma_{xy}^{\text{dc}} + \text{Re } \sigma_{xy}^{\text{ac}}(\omega) = \\
 &= \frac{e^2 k_0}{h\pi} + \frac{e^2 \mu}{h^2 v_F} \left[ \frac{2}{\alpha_t} + \frac{1}{\alpha_t^2} \ln \left( \frac{1 - \alpha_t}{1 + \alpha_t} \right) \right] + \\
 &+ \text{sgn}(\alpha_t) \frac{e^2 \mu}{h^2 v_F} \left[ \frac{-1}{\alpha_t^2} \ln \left( \frac{|\omega_{\max}^2 - \omega^2| \omega_{\min}^2}{|\omega_{\min}^2 - \omega^2| \omega_{\max}^2} \right) \right. \\
 &\left. + \left( \frac{\mu}{2\hbar\omega\alpha_t^2} + \frac{\hbar\omega}{8\mu} \frac{1 - \alpha_t^2}{\alpha_t^2} \right) \ln \left( \frac{|\omega_{\max} - \omega|(\omega_{\min} + \omega)}{|\omega_{\min} - \omega|(\omega_{\max} + \omega)} \right) - \frac{1}{|\alpha_t|} \right].
 \end{aligned} \tag{1.37}$$

$$\tag{1.38}$$

The first term is the universal response from the node separation obtained before with a correction due to the tilt and energy shift in the second term of the dc response [36]. The frequency dependent response shows two resonant structures at the limiting frequencies, but also extrapolates to  $\omega \rightarrow 0$  with finite magnitude (dashed line in panel (b)). In this case, the signs of the chemical potential, the tilt parameter and the chirality do not influence the universal term, but the

resonant peaks may be flipped. Additionally, the above results do not consider a free carrier intraband (Drude) contribution which can influence the  $\omega \rightarrow 0$  range, as shown by the grey shaded area in Fig. 1.19(b) [36, 39, 40]. Since these free carriers are responsible for the extrinsic contributions to the AHE (Ext), the frequency scale provided by the scattering rate  $\Gamma$  of the Drude peak can separate the intrinsic contributions to the total spectrum unambiguously. In addition, the finite frequency peak and resonant structures provide clear spectroscopic signatures for Weyl nodes in  $\sigma_{xy}(\omega)$ . So next, we will discuss an experimental probe to measure the frequency dependent Hall conductivity.

### 1.3.2 Magneto–Optical Activity

In a crystal with cubic symmetry, Neumann’s principle dictates a dielectric tensor of the form  $\hat{\varepsilon} = \varepsilon \cdot \mathbb{1}$  due to the isotropy along all spatial directions [41]. Applying a magnetic field, e.g. along the  $z$  axis of the crystal, reduces the symmetry leading to a modified permittivity

$$\hat{\varepsilon} = \begin{pmatrix} \varepsilon_{xx} & \varepsilon_{xy} & 0 \\ -\varepsilon_{xy} & \varepsilon_{xx} & 0 \\ 0 & 0 & \varepsilon_{zz} \end{pmatrix} \quad (1.39)$$

which will determine the light propagation in the material by Maxwell’s equations

$$\left. \begin{aligned} \mathbf{k} \times \mathbf{E} &= \omega \mu_0 \mathbf{H} \\ \mathbf{k} \times \mathbf{H} &= -\omega \varepsilon_0 \hat{\varepsilon} \mathbf{E} \end{aligned} \right\} \rightarrow \mathbf{k} \times (\mathbf{k} \times \mathbf{E}) = k_0^2 \hat{\varepsilon} \mathbf{E}. \quad (1.40)$$

with  $k_0^2 = \omega^2 \mu_0 \varepsilon_0$ . For  $\mathbf{k} \parallel z$  and  $\mathbf{E}$  in the  $xy$  plane,  $\mathbf{k} \cdot \mathbf{E} = 0$  and with  $N^2 = \mathbf{k}^2 / k_0^2$  it follows

$$N^2 \mathbf{E} = \hat{\varepsilon} \mathbf{E}. \quad (1.41)$$

From this eigenvalue equation, we obtain the refractive indices

$$N_z^2 = \varepsilon_{zz} \quad (1.42)$$

$$N_{\pm}^2 = \varepsilon_{xx} \pm i\varepsilon_{xy}. \quad (1.43)$$

$N_z$  describes the optical properties for an electric field linearly polarised along the  $z$  axis. By contrast, the modes in the  $xy$  plane have left and right circularly polarised eigenvectors which take the form

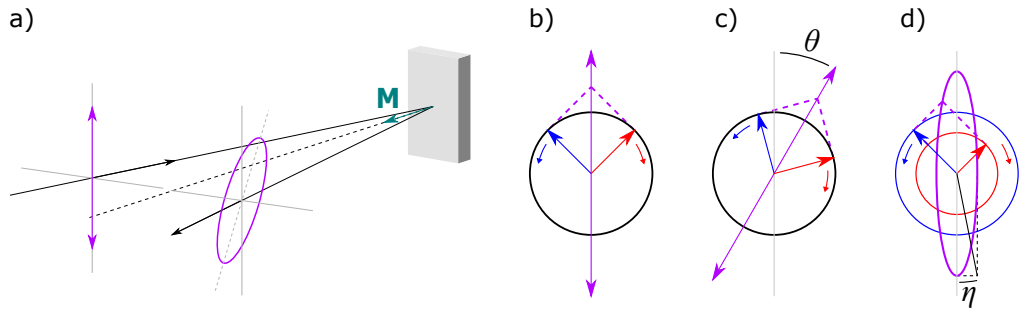
$$\mathbf{s}_{\pm} = \frac{1}{\sqrt{2}} \begin{pmatrix} 1 \\ \pm i \end{pmatrix}. \quad (1.44)$$

As a consequence, the difference in the real part of the refractive index between these two modes produces magnetic circular birefringence (MCB), while the anisotropy in the imaginary part causes magnetic circular dichroism (MCD) which are the signatures of magneto–optical activity. If we consider a magnetic material where time–reversal symmetry is broken (also in combination with translations), these effects appear naturally even without external field because of the finite off–diagonal tensor elements [42].

One phenomenon derived from these considerations is the polar magneto–optical Kerr effect (MOKE) sketched in Fig. 1.20(a). In 1877, John Kerr found that upon reflection from a magnetic surface, an originally linearly polarised light beam becomes elliptical with rotated principle axis [43]. In order to understand

**Figure 1.20**

The magneto-optical Kerr effect. (a) Upon reflection from a magnetic surface, a formerly linearly polarised light beam becomes elliptical with rotated principle axis. (b–d) Rotation  $\theta$  and ellipticity  $\eta$  can be related to MCB and MCD, respectively (adapted from [42]).



this effect, we can decompose the linear polarisation into two circularly polarised components with the same magnitude (panel b). The different refractive indices  $N_{\pm}$  for the two components will lead to different reflectivities  $r_{\pm}$  derived from the Fresnel formula for normal incidence as

$$r_{\pm} = \frac{N_{\pm} - 1}{N_{\pm} + 1}. \quad (1.45)$$

Without loss of generality, we choose an incident polarisation in the Cartesian basis  $\mathbf{E}_{\text{in}} = E_0(1, 0)$ . Because the Fresnel equation gives the reflectivities for the circular eigenmodes, we need to do a basis transformation into the circular reference frame provided by the eigenvectors  $\mathbf{s}_{\pm}$  according to

$$\hat{U} = (\mathbf{s}_+ | \mathbf{s}_-) = \frac{1}{\sqrt{2}} \begin{pmatrix} 1 & 1 \\ i & -i \end{pmatrix} \Rightarrow \hat{U}^{-1} = \frac{1}{\sqrt{2}} \begin{pmatrix} 1 & -i \\ 1 & i \end{pmatrix}. \quad (1.46)$$

The reflected field can then be calculated from

$$\mathbf{E}_{\text{ref}} = \hat{U} \begin{pmatrix} r_+ & 0 \\ 0 & r_- \end{pmatrix} \hat{U}^{-1} \mathbf{E}_{\text{in}} = \frac{E_0}{2} \begin{pmatrix} r_+ + r_- \\ i(r_+ - r_-) \end{pmatrix} = E_0 \begin{pmatrix} r_x \\ r_y \end{pmatrix}, \quad (1.47)$$

yielding the change of the polarisation state by

$$\tan \phi_K = \frac{r_y}{r_x} \approx -\theta + i\eta = \frac{i(r_+ - r_-)}{r_+ + r_-} = \frac{i(N_+ - N_-)}{N_+ N_- - 1} \quad (1.48)$$

with the approximation for small angles.  $\theta$  and  $\eta$  are the Kerr rotation and ellipticity, respectively. The former is related to a phase difference between the two circular polarisations (MCB), while the latter is caused by an absorption difference (MCD), as illustrated in Fig. 1.20(c) and (d). Since both angles are usually small, typical values for  $\theta$  and  $\eta$  are below  $1^\circ$ , justifying the above approximation [42] (MOKE is typically termed giant for angles larger than  $1^\circ$ ). We can express the complex Kerr rotation in terms of the dielectric tensor elements, which under the assumption of a weakly absorbing medium yields

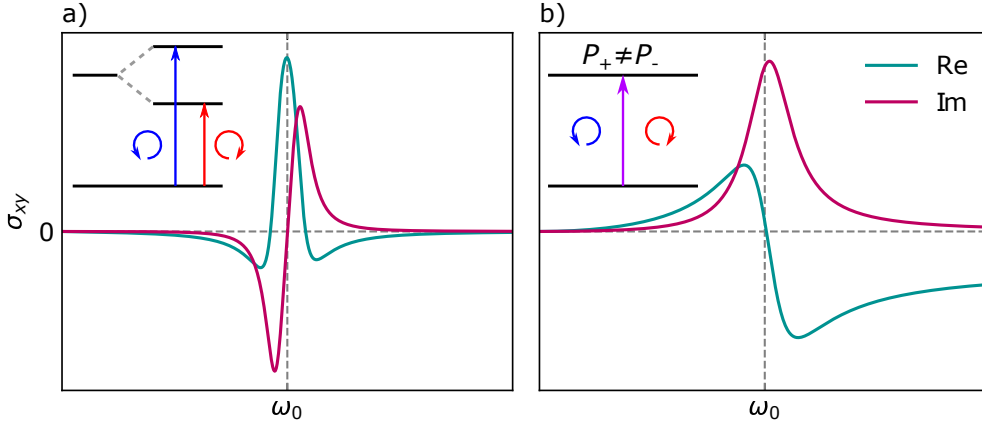
$$\theta + i\eta = -\frac{\varepsilon_{xy}}{(\varepsilon_{xx} - 1)\sqrt{\varepsilon_{xx}}} \quad (1.49)$$

or analogously with the conductivity tensor using  $\varepsilon_{\alpha\beta} = \delta_{\alpha\beta} + \frac{i}{\varepsilon_0\omega}\sigma_{\alpha\beta}$  as

**Magneto-optical Kerr effect**

$$\theta(\omega) + i\eta(\omega) = -\frac{\sigma_{xy}(\omega)}{\sigma_{xx}(\omega)\sqrt{1 + i\frac{1}{\varepsilon_0\omega}\sigma_{xx}(\omega)}} \quad (1.50)$$

where we make the dependence on the light frequency explicit.

**Figure 1.21**

Line shapes of the optical Hall effect. (a) When a spin and orbitally allowed transition is split by magnetism and spin–orbit coupling, the absorption difference for the two circular components causes a diamagnetic line shape. (b) If the energy remains the same but the transition matrix elements  $P_{\pm}$  become different, we obtain a paramagnetic line shape (adapted from [45]).

Eq. 1.50 enables the calculation of the optical Hall conductivity  $\sigma_{xy}(\omega)$  from measurements of the diagonal conductivity and the Kerr effect over a broad range of light frequencies and therefore is one of the central formulas for this thesis. We will see an introduction to the measurement techniques in Sec. 2.1 and 2.3. Hence, if Weyl points determine the off–diagonal response, we are able to measure the spectroscopic signatures from Fig. 1.19 which makes magneto–optical spectroscopy a suitable tool to investigate the interplay of electronic band topology with magnetism.

However, not only the presence of Weyl nodes produces a finite off–diagonal response. From the above considerations, a finite  $\sigma_{xy}$  and the presence of MCD and MCB are linked, so it is instructive to rewrite the Kubo formula in terms of the circular momentum operators  $p_{\pm} = p_x \pm ip_y$ . For Re  $\sigma_{xx}$  and Im  $\sigma_{xy}$  this yields [44]

$$\text{Re } \sigma_{xx} = \frac{e^2 \pi}{4m^2 V} \sum_{\mathbf{k}, n, n'} \frac{|f(\varepsilon_n(\mathbf{k})) - f(\varepsilon'_n(\mathbf{k}))|}{\hbar \omega_{nn'}} \delta(\omega - \omega_{nn'}) \cdot \left[ |\langle n, \mathbf{k} | p_+ | n', \mathbf{k} \rangle|^2 + |\langle n, \mathbf{k} | p_- | n', \mathbf{k} \rangle|^2 \right] \quad (1.51)$$

$$\text{Im } \sigma_{xy} = \frac{e^2 \pi}{4m^2 V} \sum_{\mathbf{k}, n, n'} \frac{|f(\varepsilon_n(\mathbf{k})) - f(\varepsilon'_n(\mathbf{k}))|}{\hbar \omega_{nn'}} \delta(\omega - \omega_{nn'}) \cdot \left[ |\langle n, \mathbf{k} | p_+ | n', \mathbf{k} \rangle|^2 - |\langle n, \mathbf{k} | p_- | n', \mathbf{k} \rangle|^2 \right]. \quad (1.52)$$

Focusing on  $\sigma_{xy}$ , Eq. 1.52 provides two possibilities for a finite optical Hall effect: Either the transition energies for  $p_+$  and  $p_-$  are different or their matrix elements. Both options are sketched in Fig. 1.21 in panels (a) and (b), respectively [45]. When a spin and orbitally allowed transition, e. g. a charge transfer excitation, is split by the exchange field together with spin–orbit coupling, a double transition with so–called diamagnetic line shape can be observed in  $\sigma_{xy}$  (panel a). Because of the absorption difference for the two circular photons, this causes a derivative structure around the central frequency in the imaginary part. By contrast, the single transition or paramagnetic line shape (panel b) shows a peak at  $\omega_0$  due to the different matrix elements  $P_{\pm} = \langle n, \mathbf{k} | p_{\pm} | n', \mathbf{k} \rangle$ . This may appear for spin and electric dipole forbidden transitions, e. g. between crystal field levels. Because of the forbidden character, these contributions are usually weaker [45, 46].

With these considerations, it is clear that a general optical Hall effect spectrum may have topological (intrinsic) as well as trivial (extrinsic) contributions. Hence, the assignment of features and line shapes requires detailed knowledge of the momentum dependent band structure, which can be provided by *ab initio* calculations. An introduction to the theoretical framework is beyond the scope of this thesis, but we will see how the symbiosis with the experiment can provide deep insights into the nature of the AHE in materials in Chapters 3 and 5. So next, we will introduce the measurement techniques which provide the basis for this type of investigation.

## Experimental Methods for Magneto–Optical Spectroscopy

In this chapter, we will review the experimental techniques necessary for magneto–optical spectroscopy. After a short section introducing the measured quantities, we will see how to deduce the diagonal conductivity tensor elements as function of temperature and magnetic field. Then, we will cover a polarisation modulation technique for sensitive detection of the Kerr parameters and a method to extend these spectra into the far–infrared range. The combination of these techniques will yield broadband optical Hall effect spectra, which we will analyse in the subsequent chapters for several materials potentially hosting electronic band structure with non–trivial topology.

### 2.1 Infrared Spectroscopy

Generally, for light propagation in matter, any process which couples to the electromagnetic wave can modify the propagation in the respective material. Derived from Maxwell’s equation, this coupling can be described phenomenologically by the complex refractive index which includes a dispersive component that modifies the wavelength and velocity of light, and a dissipative component related to absorption. Instead of the refractive index, the optical conductivity or the dielectric function may be used alternatively. There are a variety of different excitations which can contribute to the material response, among them

- ▷ magnons,
- ▷ lattice vibrations,
- ▷ free charge carriers,
- ▷ excitons,
- ▷ interband absorption,
- ▷ transitions from core levels,

all of which have an associated energy scale that can be analysed by optical spectroscopy with light waves of up to near ultraviolet frequencies [47]. The photon energy, (angular) frequency, wavenumber or wavelength may be used interchangeably. Depending on the strength of absorption, we require measurements of the light transmitted through or reflected from the surface of the sample. Since all of the materials investigated in this thesis are metallic, only the reflectivity spectroscopy will be discussed further.

We have already seen the Fresnel formula which relates the reflectivity to the refractive index

$$r = \frac{N - 1}{N + 1} = \sqrt{R}e^{i\phi}. \quad (2.1)$$

Because detectors for visible and infrared frequencies are only able to measure the light intensity, but not the phase  $\phi$ , they can only provide the reflectance  $R$ . In order to separate the characteristics of the spectrometer from the sample,

reflectivity measurements require a reference spectrum recorded on an ideal mirror. For this purpose, noble metals like gold and silver with reflectivity close to unity are usually used. From the intensity spectra of the sample and the mirror, the sample reflectance can then be calculated as

$$R = \frac{I_{\text{sam}}}{I_{\text{ref}}} = |r|^2. \quad (2.2)$$

Unfortunately, this measurement does not give access to the phase spectrum  $\phi$  which is required for the determination of the complex  $N$ . In order to obtain it, we can use the Kramers–Kronig relations which connect the real and imaginary parts of the optical constants due to causality [47]. For the phase they yield

$$\phi(\omega) = -\frac{\omega}{\pi} \int_0^\infty \frac{\ln [R(\omega')] - \ln [R(\omega)]}{\omega'^2 - \omega^2} d\omega'. \quad (2.3)$$

Since the boundaries of the integral are not accessible experimentally, we need to perform broadband measurements and then rely on extrapolation for  $R$ . In the  $\omega \rightarrow 0$  limit, the Hagen–Rubens relation  $R \propto 1 - 8\sqrt{\epsilon_0\omega/\sigma_0}$  dependence is reasonable for metals, with the vacuum permittivity and dc conductivity  $\epsilon_0$  and  $\sigma_0$ , respectively, while we can use a power law  $R \propto \omega^{-\alpha}$  at high frequencies [48]. With the complex reflectivity determined and neglecting the contribution of the magnetic permeability, we can calculate the complex refractive index from Eq. 2.1 which gives access to the other optical constants like the dielectric function via  $N = \sqrt{\epsilon}$  and the conductivity  $\epsilon = 1 + \frac{i}{\epsilon_0\omega}\sigma$ .

Here, it is important to note that the optical constants are tensorial quantities. The effective value of the dielectric constant or conductivity is therefore determined by the geometry of the measurement system. If we consider a sample with tetragonal symmetry and  $z \parallel c$ , the permittivity tensor reads as

$$\hat{\epsilon} = \begin{pmatrix} \epsilon_{xx} & 0 & 0 \\ 0 & \epsilon_{xx} & 0 \\ 0 & 0 & \epsilon_{zz} \end{pmatrix} \quad (2.4)$$

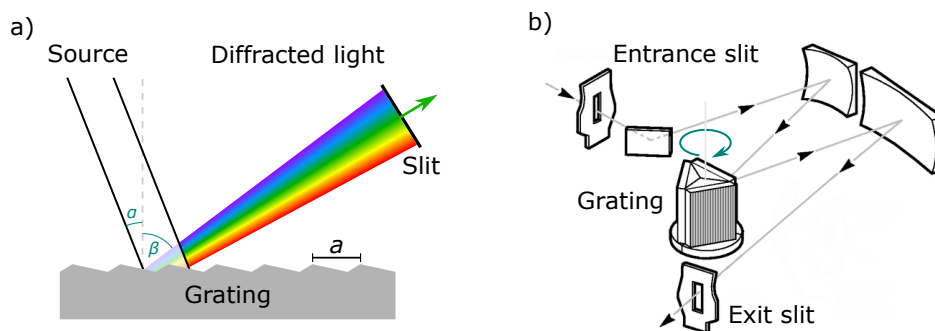
which yields two eigenvalues for the refractive index  $N_{1,2}^2 = \epsilon_{xx}$  and  $N_3^2 = \epsilon_{zz}$ . Hence, if the incoming light is polarised in the  $ab$  plane of the crystal, we can measure  $\epsilon_{xx}$  (and therefore  $\sigma_{xx}$ ). For polarisation along the  $c$  axis, we determine  $\epsilon_{zz}$  ( $\sigma_{zz}$ ). The correct alignment of the crystallographic axes must be ensured during the sample preparation to avoid mixing the eigenvalues in the measurement.

So next, we need to obtain the intensity spectra  $I_{\text{sam}}(\omega)$  and  $I_{\text{ref}}(\omega)$  experimentally.

### 2.1.1 Grating Spectrometer

Conceptually, the most simple type of spectrometer relies on a monochromator. A dispersive element like a prism or grating splits the incoming wavelengths spatially, which can then be selected by a slit. This is schematically shown for a grating spectrometer in Fig. 2.1(a). Here, the path difference between neighbouring grooves of the grating must be an integer multiple of the wavelength in order to obtain constructive interference. Hence, the grating equation is

$$a(\sin \alpha - \sin \beta) = m\lambda \quad (2.5)$$

**Figure 2.1**

(a) Working principle of a grating spectrometer. The light from the source is split due to different diffraction angles for every wavelength. A slit selects the wavelength for the experiment (b) Schematic lightpath for the Oriel Instruments Cornerstone 260 used during the experiments. The wavelengths are scanned by rotation of the grating (adapted from [49]).

where  $a$  is the lattice constant of the grating,  $\alpha$  and  $\beta$  are the angles of incoming and diffracted beam with respect to the grating normal and  $m$  the diffraction order [49]. The wavelength can be scanned e. g. by rotating the grating, as employed in the Oriel Instruments Cornerstone 260 spectrometer used during the experiments, which is schematically shown in panel (b). With the monochromated beam, we can then determine  $I(\omega)$ . In the grating equation, we only considered interference from neighbouring sites. Taking the other grooves into account sharpens the diffraction peak, hence the wavelength resolution becomes better with increasing density of lines on the grating. As the slit will eventually select a section of the diffracted beam, the experimental resolution will be determined by its width [49].

This spectroscopic technique has two major disadvantages. Firstly, it is slow because the intensity can only be measured for one wavelength at a time. Secondly, the intensity of the source is distributed over all diffraction orders  $m$ , so only a fraction will eventually be used for the experiment. This limits the application to wavelength ranges where high intensity light sources like halogene or gas discharge lamps are available which are typically near-infrared (NIR), visible (VIS) and near-ultraviolet (UV) [47]. An alternative approach which overcomes both drawbacks is Fourier spectroscopy.

### 2.1.2 Fourier Spectroscopy

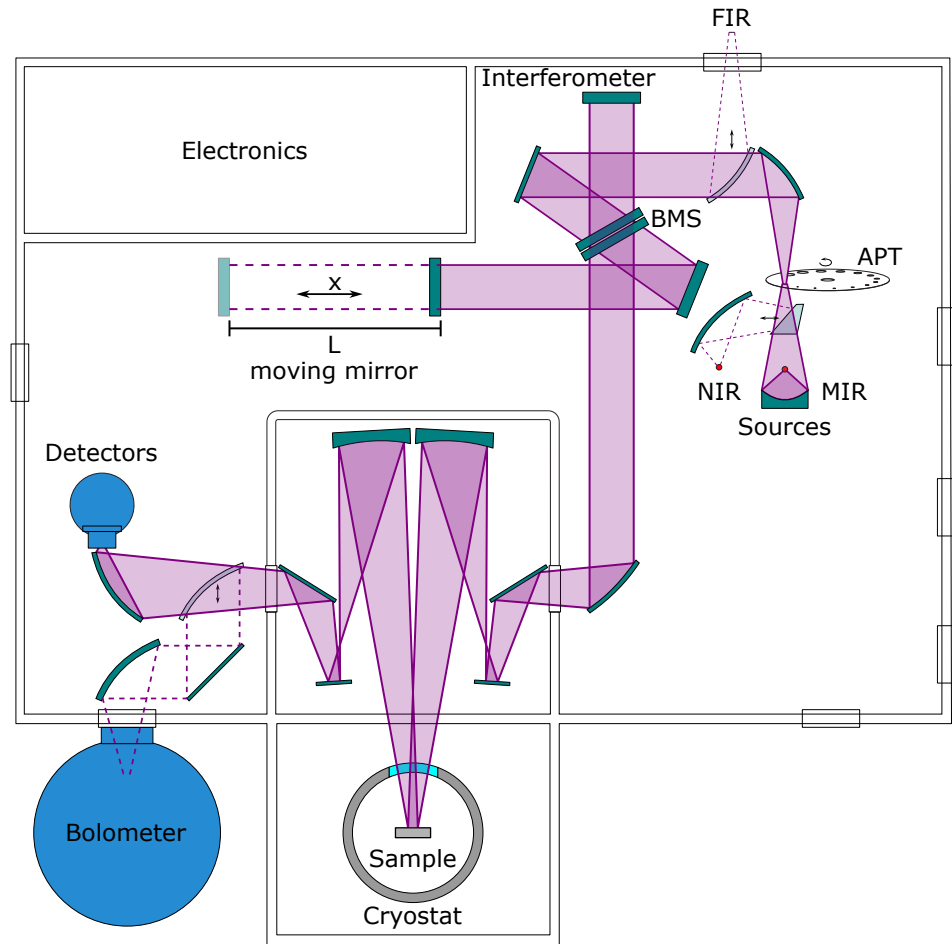
In a Fourier transform infrared (FTIR) spectrometer, an interferometric approach is taken for detection of  $I(\omega)$ . Because it does not suffer from the above loss of intensity, this technique can also cover the far- and mid-infrared (FIR, MIR) spectral ranges. The operation principle is based on a Michelson interferometer, as for example realised in the Bruker Vertex 80v, schematically shown in Fig. 2.2(a). The light from the broadband sources is guided to the interferometer, where it is separated into two (equal) parts by a beamsplitter (BMS). One of the arms is terminated by a standing mirror, while the other arm has a moving mirror that can travel in direction  $x$  for a total distance  $L$ . The corresponding beam acquires an additional phase shift of  $e^{i(\omega/c)2x}$ . The position of the mirror is recorded via a HeNe reference laser. Afterwards, the beamsplitter recombines the two beams which are subsequently guided to the sample and detector.

If the source has a spectrum  $S(\omega)$ , the intensity on the detector is obtained from interference of the two arms as

$$I(x) = \int_{-\infty}^{\infty} S(\omega) \cos\left(\frac{\omega}{c}2x\right) d\omega \quad (2.6)$$

**Figure 2.2**

Schematic of a Bruker Vertex 80v FTIR configured for reflectivity measurements. The light provided by the sources is guided to the Michelson interferometer where it is separated by a beam-splitter (BMS). The interferometer arms have one standing and one moving mirror that can travel along  $x$  by a total distance  $L$ . After the two beams interfere, the light is guided to the sample by a mirror array and after reflection to the detector chamber. An external bolometer may be used for FIR measurements. The aperture (APT) controls the spot size and the available intensity (adapted from [50]).

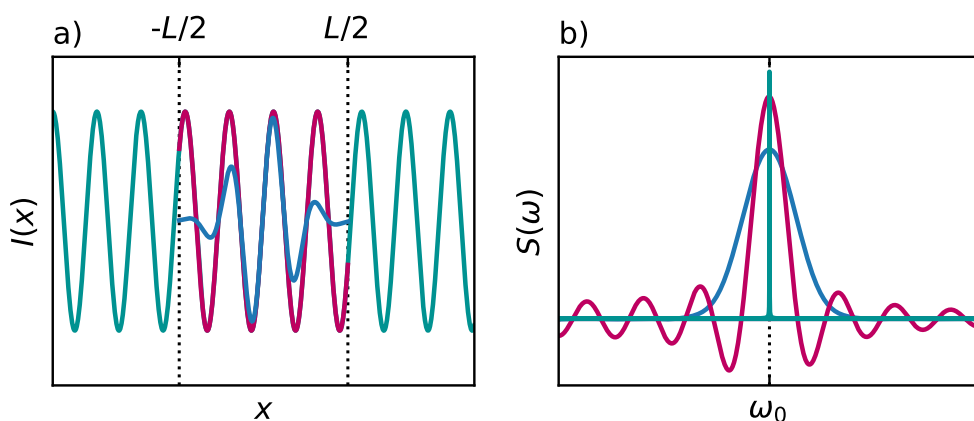


which is called the interferogram and has the form of a cosine Fourier transform of the source spectrum. Therefore, we can calculate the source spectrum from the inverse transformation

$$S(\omega) = \int_{-\infty}^{\infty} I(x) \cos\left(\frac{\omega}{c} 2x\right) dx. \quad (2.7)$$

and get the spectrum at all frequencies simultaneously. With the sample or reference mirror in the lightpath, we thereby obtain  $I_{\text{sam}}(\omega)$  and  $I_{\text{ref}}(\omega)$  [51].

The application of the above ideal formulas is limited in an actual experiment. First of all, it is not possible to measure  $I(x)$  on an infinite range, as the mirror can only travel by  $L$ . This provides a limit to the frequency resolution as illustrated in Fig. 2.3. Panel (a) shows the interferogram for a monochromatic light source if the mirror could travel infinite distances (green) or only finite  $L$  (purple). The corresponding Fourier transforms are shown in panel (b). We obtain the single frequency  $\omega_0$  of the monochromatic source for infinite integration boundaries. For the limited case however, this line is broadened in a  $\sin x/x$  fashion. The full width at half maximum (FWHM) of this peak will therefore determine the frequency resolution, hence, we need to set  $L$  according to the sharpest spectral features to be properly resolved. In a similar fashion, the smallest step size  $\Delta x$  of the travelling mirror will provide an upper bound for measurable frequencies by the Nyquist theorem. In addition, the stepping turns the Fourier integral to a sum over discrete  $x$ , which can cause aliasing at high frequencies and must be taken into account for operation towards the UV [47, 51].

**Figure 2.3**

Spectral artefacts for finite travel distance. (a) The interferogram of a monochromatic light source ( $\omega_0$ ) is a cosine wave (green), finite  $L$  cuts a section (purple). (b) Fourier transforms: For infinite limits, the result is a delta peak at  $\omega_0$  (green) which is smeared by finite  $L$  to a  $\sin x/x$  shape including oscillations around the baseline (purple) that need to be corrected by apodisation, e.g. with a Gaussian (blue).

Another source of error from finite  $L$  can be seen in panel (b). Next to the sharp central peak additional oscillations appear around the baseline of the purple spectrum. The occurrence of these “feet” around any sharp spectral feature results from the abrupt cutoff of  $I(x)$  at the travel limits. In order to avoid them, the interferogram can be multiplied by a window function e.g. a Gaussian (blue in panel a) to obtain smooth boundaries, although this also slightly affects the resolution in (b). This process is called apodisation [47, 51].

Despite these difficulties, FTIR spectroscopy is the most commonly used tool for broadband optical spectroscopy from FIR to UV frequencies. This requires a proper configuration of the optical elements. Usually, FTIR systems are equipped with a variety of different sources, beamsplitters, windows and detectors for ideal measurement conditions in the respective range [51]. A summary of optical components and materials used may be found in Fig. 2.9.

As in magnetic materials the band structure and the free carrier response may change upon applying external magnetic fields, performing reflectivity measurements with varying field strength may give additional insights into the response functions and the coupling between electronic structure and magnetism. The following section discusses a setup where the sample can be placed in magnetic field in a FTIR spectrometer.

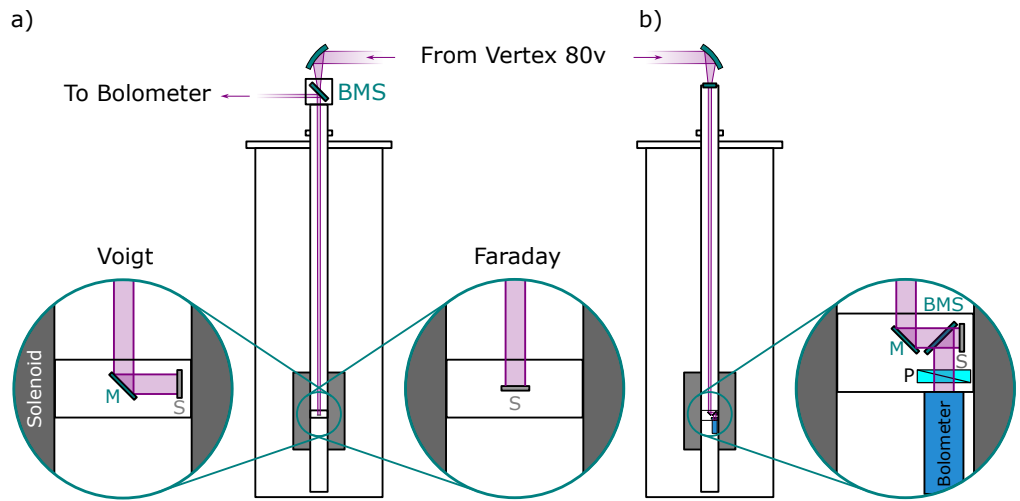
## 2.2 Magneto–Reflection Experiments

During the PhD, I assembled a setup coupling a Bruker Hyperion FTIR microscope to a 5 T Oxford optical magnet, which is in principle able to cover the relevant frequency and field ranges for the study presented in Chapter 6 (compare Appendix A.1). Initial measurements on this new setup were unfortunately inconclusive since a relatively high noise level in the FIR and parasitic cryostat motion in field compromised the reliability of the data. Therefore, and due to the necessity to apply higher fields for  $\text{Co}_3\text{Sn}_2\text{S}_2$ , magneto–reflection experiments were performed during research visits at the LNCMI Grenoble in the lab of Milan Orlita.

Schematics of the available setups are shown in Fig. 2.4. The light from a globar or mercury lamp in a Vertex 80v spectrometer is coupled into a light pipe by a parabolic mirror, which guides the beam into a solenoid. This can either be a resistive coil for fields up to 34 T or a superconducting solenoid able to produce magnetic fields up to 16 T. The sample holder can be configured for both Faraday

**Figure 2.4**

(a) Schematic of the magneto–reflection setup in Voigt and Faraday configuration with an external bolometer. The light from a Vertex 80v is guided through a beamsplitter (BMS) into the solenoid, where a mirror (M) in the sample holder selects the configuration. (b) Setup for polarised reflection measurements in Voigt configuration. In the sample holder, a mirror (M) and beamsplitter (BMS) guide the light via the sample (S) and a polariser (P) to an internal bolometer.



and Voigt configurations with an external bolometer (panel a). Due to spatial limitations, polarised reflectivity measurements can only be performed in Voigt configuration (panel b), hence the light is reflected from a mirror (M) before passing through a beamsplitter (BMS) onto the sample (S). The beamsplitter guides the reflected light through a polariser (P) to the internal bolometer. The probe is filled with a small amount of helium as exchange gas which ensures proper thermalisation of sample and detector at 4 K.

We measure the magnetic field dependence of the intensity with respect to the zero–field spectrum used as a reference, resulting in  $R(B)/R(0)$  spectra. Since the bolometer response also has a small field dependence, the measurement is repeated using a gold mirror instead of the sample. The  $R(B)/R(0)$  spectra were corrected with these as reference, assuming that the reflectivity of gold has a negligible field dependence. By using KRS–5 and wiregrid polarisers in combination with KBr and Si beamsplitters, the FIR–MIR range between 12 – 500 meV could be covered in these experiments.

So far, the introduced measurement techniques only detected the intensity changes of the reflected light. In the following, we will consider methods to monitor the polarisation state in addition.

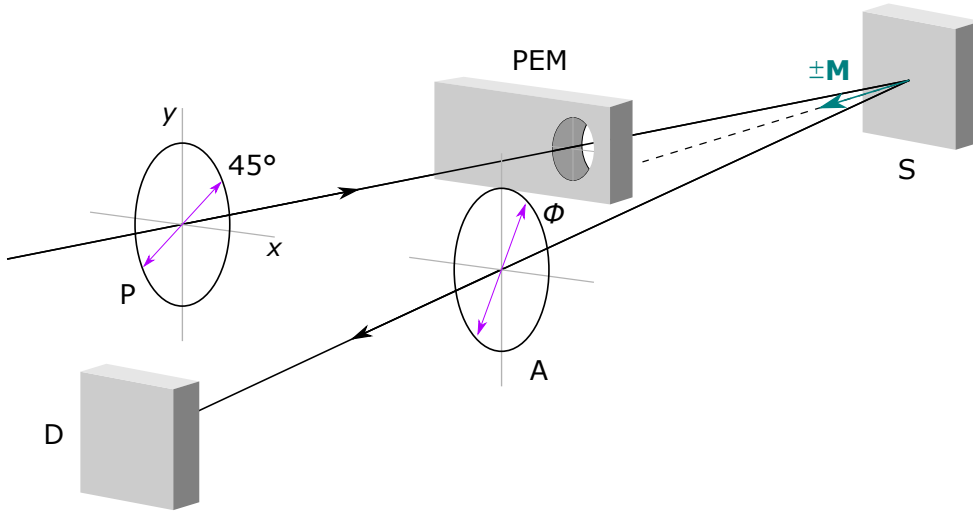
## 2.3 Magneto–Optical Kerr Effect Spectroscopy

In order to calculate the optical Hall effect spectra, we need to measure both Kerr parameters over a broad energy range. In principle, the same spectroscopic techniques introduced above can be employed, but we need additional optical components which enable the detailed analysis of the polarisation state. We consider two possibilities in the following.

### 2.3.1 MOKE Measurement with a Photoelastic Modulator

One convenient way to measure both Kerr parameters simultaneously with high precision uses a photoelastic modulator (PEM) as a polarisation modulation component. This method was originally proposed by Sato in Ref. 52 and the schematic lightpath is shown in Fig. 2.5.

The incoming light is polarised at  $45^\circ$  with respect to the optical axis of the PEM by a polariser P producing  $\mathbf{E}_P = E_0/\sqrt{2}(1, 1)$ . The PEM contains

**Figure 2.5**

Lightpath for PEM–based MOKE spectroscopy. A polariser (P) set at  $45^\circ$  provides the input polarisation for the photoelastic modulator (PEM). After reflection from the sample (S), an analyser (A) set to angle  $\phi$  selects one projection of the electric field before the detector (D) measures the intensity. Two measurements for  $\pm M$  are antisymmetrised to obtain the MOKE parameters odd in field (adapted from [52]).

an isotropic crystal which is turned birefringent by periodically applied strain, providing a retardation of the form

$$\delta = \delta_0 \sin \omega_0 t \quad (2.8)$$

for the  $y$  axis which alternates the electric field continuously between left and right circular polarisation states (compare Fig. 2.6(a,b)). In matrix form, this element is represented by  $\begin{pmatrix} 1 & 0 \\ 0 & e^{i\delta} \end{pmatrix}$ . After reflection from the sample with the reflectivities  $r_+$  and  $r_-$  for the eigenstates known from Sec. 1.3.2, an analyser at angle  $\phi$  projects one linearly polarised component whose intensity is measured by the detector. Thus the electric field at the detector is given by

$$E = (\cos \phi \quad \sin \phi) \frac{1}{\sqrt{2}} \begin{pmatrix} 1 & 1 \\ i & -i \end{pmatrix} \begin{pmatrix} r_+ & 0 \\ 0 & r_- \end{pmatrix} \frac{1}{\sqrt{2}} \begin{pmatrix} 1 & -i \\ 1 & i \end{pmatrix} \begin{pmatrix} 1 & 0 \\ 0 & e^{i\delta} \end{pmatrix} \frac{E_0}{\sqrt{2}} \begin{pmatrix} 1 \\ 1 \end{pmatrix} \quad (2.9)$$

which turns into

$$E = \frac{E_0}{2\sqrt{2}} (\cos \phi \quad \sin \phi) \begin{pmatrix} r_+(1 - ie^{i\delta}) + r_-(1 + ie^{i\delta}) \\ i [r_+(1 - ie^{i\delta}) - r_-(1 + ie^{i\delta})] \end{pmatrix} = \frac{E_0}{2\sqrt{2}} [r_+(1 - ie^{i\delta})e^{i\phi} + r_-(1 + ie^{i\delta})e^{-i\phi}]. \quad (2.10)$$

We introduce the short notations  $2R = r_+^2 + r_-^2$ ,  $\Delta R = r_+^2 - r_-^2$  and  $\Delta\vartheta = \vartheta_+ - \vartheta_-$  ( $r_\pm = |r_\pm| e^{i\vartheta_\pm}$ ) and write the intensity proportional to the absolute square of the electric field as

$$I \propto |E|^2 = \frac{E_0^2 R}{4} [1 + 2\eta \sin \delta + \sin(2\theta + 2\phi) \cos \delta] \quad (2.11)$$

with the condition that  $\Delta R/R \ll 1$ . For this equation, we used that

$$\theta + i\eta = -\frac{1}{2}\Delta\vartheta + i\frac{1}{4}\frac{\Delta R}{R}. \quad (2.12)$$

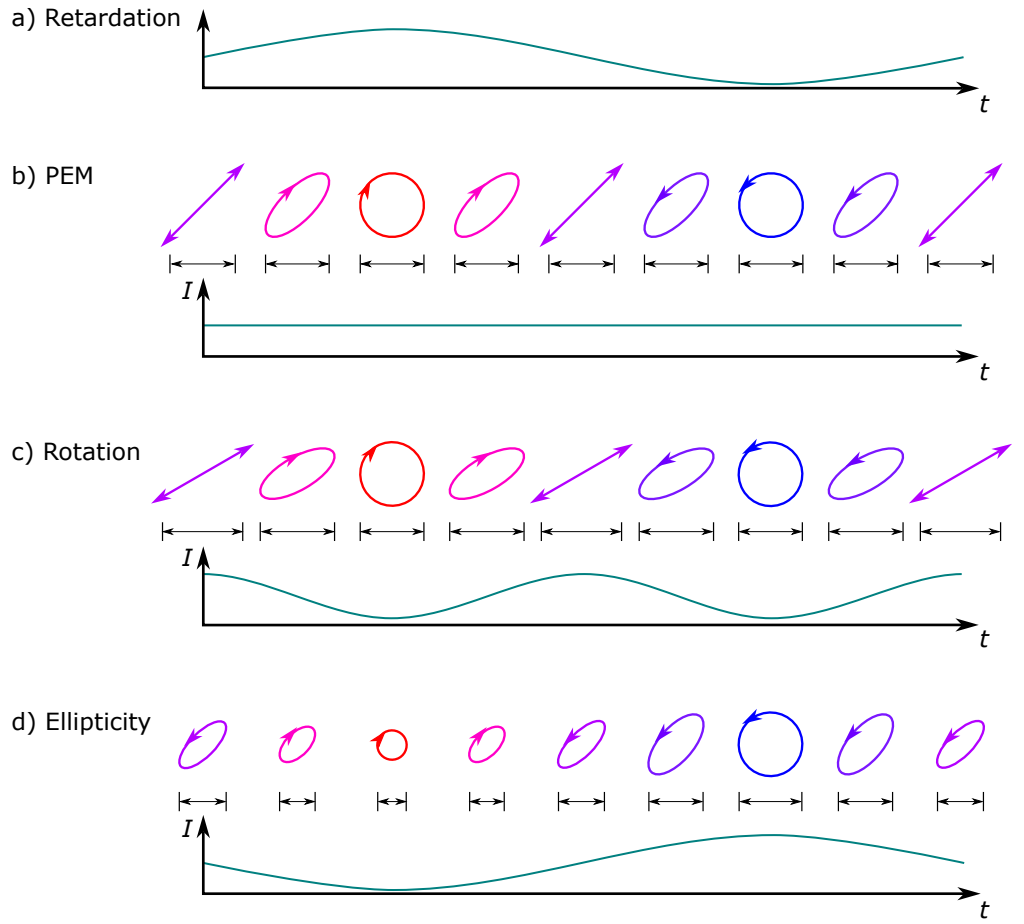
We can now insert Eq. 2.8 and expand the intensity using the Jacobi–Anger identities

$$\sin(\delta_0 \sin \omega_0 t) = 2J_1(\delta_0) \sin \omega_0 t \dots \quad (2.13)$$

$$\cos(\delta_0 \sin \omega_0 t) = J_0(\delta_0) + 2J_2(\delta_0) \sin 2\omega_0 t \dots \quad (2.14)$$

**Figure 2.6**

Polarisation modulation of the MOKE components. (a) represents one period of retardation, which produces the polarisation sequence after the PEM shown in the first row in panel (b). The second and third row present the horizontal projection by the analyser and the resulting modulation of the intensity. Consequently, panels (c) and (d) explain how rotation and ellipticity influence the polarisation state and thus produce intensity signals proportional to the  $2\omega_0$  and  $\omega_0$  components, respectively (adapted from [52]).



where the  $J_i$ s are the  $i$ th order Bessel functions which yields the following Fourier series for the detector intensity

$$I = I(0) + I(\omega_0) \sin \omega_0 t + I(2\omega_0) \sin 2\omega_0 t + \dots \quad (2.15)$$

with

$$I(0) = I_0 R [1 + J_0(\delta_0) \sin(\Delta\vartheta + 2\phi)] \quad (2.16)$$

$$I(\omega_0) = a I_0 \Delta R J_1(\delta_0) \quad (2.17)$$

$$I(2\omega_0) = b I_0 R J_2(\delta_0) \sin(\Delta\vartheta + 2\phi). \quad (2.18)$$

Here,  $a$  and  $b$  are constant prefactors depending on the transfer function of the preamplifiers. By using a Lock–In detection, we can now measure the  $\omega_0$  and  $2\omega_0$  intensities, beside the dc. Assuming only small phase shifts  $\Delta\vartheta$  and setting the analyser angle to small values  $\phi \approx 0$ , the ratios of the intensity components become

$$\frac{I(\omega_0)}{I(0)} = A J_1(\delta_0) \eta \quad (2.19)$$

$$\frac{I(2\omega_0)}{I(0)} = B J_2(\delta_0) (\theta + \phi) \quad (2.20)$$

with constants  $A$  and  $B$  summarising the prefactors including sensitivities for the detection and amplification system. Fig. 2.6 explains why the  $\omega_0$  and  $2\omega_0$  components represent ellipticity and rotation, respectively. During one period of

retardation, displayed in panel (a), the PEM produces the polarisation sequence between the two circular polarisations as shown in panel (b). With the analyser picking up e. g. the horizontal component of the polarisation, this modulation does not alter the detector intensity. By contrast, if the sample shows MOKE, panels (c) and (d) show how rotation and ellipticity influence the polarisation state and thereby produce the intensity modulations at  $2\omega_0$  and  $\omega_0$ , respectively.

However, there is one additional peculiarity to take into account. Non–magnetic phenomena such as linear birefringence of optical components like lenses or windows in the lightpath can also influence the polarisation state and need to be separated from the MOKE contribution. Onsager relations require that the off–diagonal conductivity is odd under time–reversal, therefore, in general, the Hall conductivity is measured in two time–reversed states [53]. For the present case of a ferromagnet this implies measurement with reversed magnetisation

$$\sigma_{xy}(\mathbf{M}) = -\sigma_{xy}(-\mathbf{M}). \quad (2.21)$$

By Eq. 1.50, this translates to the Kerr parameters being antisymmetric in the magnetisation. Thus, in order to obtain the MOKE signal, we need to antisymmetrise two measurements with  $\pm\mathbf{M}$  as indicated in Fig. 2.5.

Because of the prefactors  $AJ_1(\delta_0)$  and  $BJ_2(\delta_0)$ , we need to calibrate the antisymmetrised data. For the rotation, this can be achieved by manually rotating the analyser by an angle  $\pm\phi_0$ , thus simulating the intensity change of a rotation by that angle. Dividing the intensity difference by  $\phi_0$  therefore gives the calibration according to

$$\left[ \frac{I(2\omega_0)}{I(0)} \Big|_{+\phi_0} - \frac{I(2\omega_0)}{I(0)} \Big|_{-\phi_0} \right] / 2\phi_0 = BJ_2(\delta_0). \quad (2.22)$$

For the ellipticity, the calibration works similarly, but we have to insert another retarding element, e. g. a quarter–wave plate into the lightpath behind the PEM. The total retardation therefore becomes

$$\delta = \delta_\lambda + \delta_0 \sin \omega_0 t \quad (2.23)$$

with  $\delta_\lambda = \pi/2 \cdot \lambda/\lambda_0$ , where  $\lambda_0$  is the wavelength where the quarter–wave plate has a retardation of exactly  $\pi/2$ . This modifies Eqs. 2.16 and 2.17 according to:

$$I(0)' = \frac{1}{2} I_0 R [1 \pm J_0(\delta_0) \cos \delta_\lambda] \quad (2.24)$$

$$I(\omega_0)' = \mp AI_0 R J_1(\delta_0) \sin \delta_\lambda \sin \omega_0 t \quad (2.25)$$

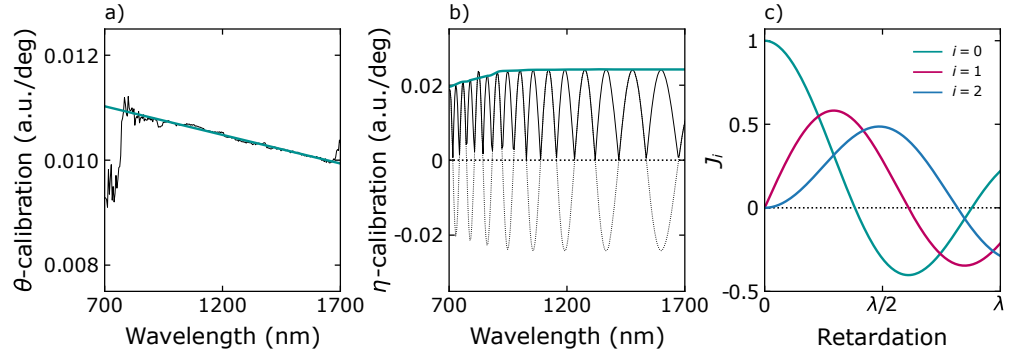
So now, rotation of the analyser by an angle  $\pm\phi_0$  yields an intensity difference determining the prefactor  $AJ_1(\delta_0)$ , calibrating the ellipticity with

$$\left[ \frac{I(\omega_0)'}{I(0)'} \Big|_{+\phi_0} - \frac{I(\omega_0)'}{I(0)'} \Big|_{-\phi_0} \right] / 2\phi_0 = AJ_1(\delta_0). \quad (2.26)$$

The above considerations hold for both monochromatic and broadband sources. In the latter case, we obtain a calibration value for every wavelength. Fig. 2.7(a) and (b) show exemplary calibration curves for the NIR–range for rotation and ellipticity. The black spectra represent the measured intensity difference for rotated analyser divided by the angle and the green curve the deduced calibration. For the ellipticity, the  $\sin \delta_\lambda$  term introduces a parasitic oscillation (dashed), that we compensate by using the envelope function of the absolute value.

**Figure 2.7**

Exemplary calibrations for PEM measured MOKE components. (a,b) The black spectra are the measured intensity differences divided by the angle while the green curves are the resulting calibrations. For the ellipticity, we have to take the envelope function of the absolute value due to oscillations coming from the quarter-wave plate. (c) The three Bessel functions appearing in prefactors.



Panel (c) shows the three Bessel functions that appear in the prefactors. For optimal sensitivity for the rotation, the retardation should be set to the maximum of  $J_2$  around  $\lambda/2$ , while for the ellipticity the optimum of  $J_1$  would be around  $0.29\lambda$ . For simultaneous measurements, a compromise of  $0.4\lambda$  can be used.

This technique works well in the MIR–VIS range because of readily available industrial PEM devices. As it turns out, there is no commercially available PEM–option for the FIR, so we need to consider a different detection mechanism for this range.

### 2.3.2 FIR–Rotation Measurements

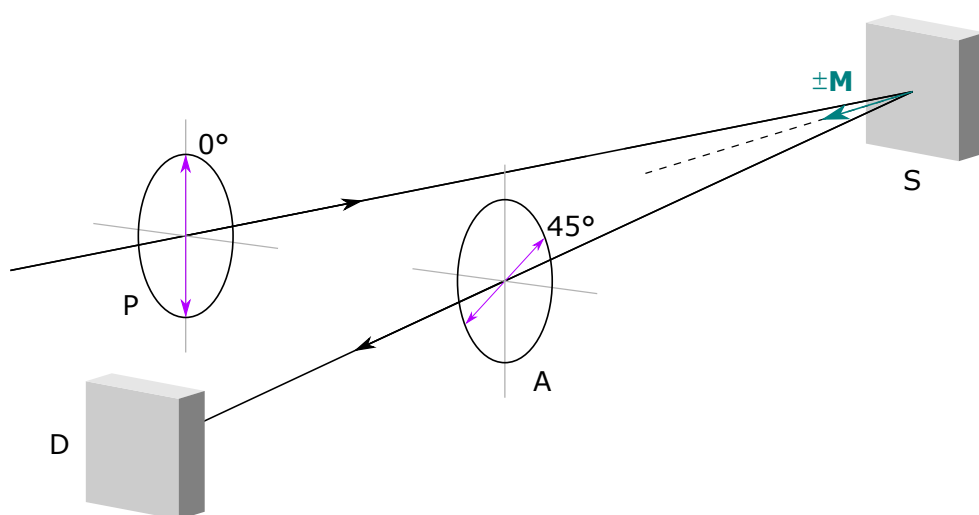
In order to gain information on bands closer to the Fermi energy, we would like to extend the MOKE spectra to the FIR range. Although the sensitivity is smaller than for PEM–based techniques, we employ a setup with fixed polarisers of high extinction ratio with the schematic lightpath shown in Fig. 2.8. The polariser P provides an incoming polarisation of the form  $\mathbf{E}_{\text{in}} = E_0(1, 0)$ , so with the analyser set at an angle  $\phi$ , the electric field on the detector is

$$\begin{aligned} E &\propto \begin{pmatrix} \cos \phi & \sin \phi \end{pmatrix} \begin{pmatrix} \cos \theta & -\sin \theta \\ \sin \theta & \cos \theta \end{pmatrix} \begin{pmatrix} 1 \\ i \tan \eta \end{pmatrix} \\ &= \cos \phi + \sin \phi (\theta + i\eta). \end{aligned} \quad (2.27)$$

Consequently, with the intensity being proportional to the square of the field and under the assumption that the Kerr parameters are small thus neglecting higher than linear order terms, we find

$$\begin{aligned} I &\propto |E|^2 \propto |\cos \phi + \theta \sin \phi + i\eta \sin \phi|^2 \\ &\approx \cos^2 \phi + \theta \sin(2\phi). \end{aligned} \quad (2.28)$$

Thus, the intensity is linearly proportional to the rotation with the highest sensitivity for  $\phi = 45^\circ$ . To get the rotation odd in field, we again antisymmetrise measurements for opposite fields. As before, the calibration is performed by manual rotation of the analyser. Unfortunately, we do not have access to the ellipticity in this measurement scheme, but we can recover it using the Kramers–Kronig relationship. Because of the broadband nature of our experiments, we can simultaneously fit the rotation and ellipticity spectra with an oscillator model in the software Reffit [54]. With a satisfactory fit of the measured ranges, we can deduce the shape of the ellipticity also in the FIR. With this method, we can push the low–frequency cutoff down to 25 meV, depending on the overall detector intensity determined by sample characteristics such as dimensions as well as the

**Figure 2.8**

Lightpath for FIR rotation measurements. Polariser (P) and analyser (A) are set at  $45^\circ$  relative orientation before and after the sample (S) with detector (D) measuring the transmitted intensity. Again, two measurements for opposite fields are antisymmetrised.

magnitude of the MOKE and reflectivity. After introduction to the measurement principles, next we summarise the experimental setups.

### 2.3.3 MOKE–Spectroscopy Setups

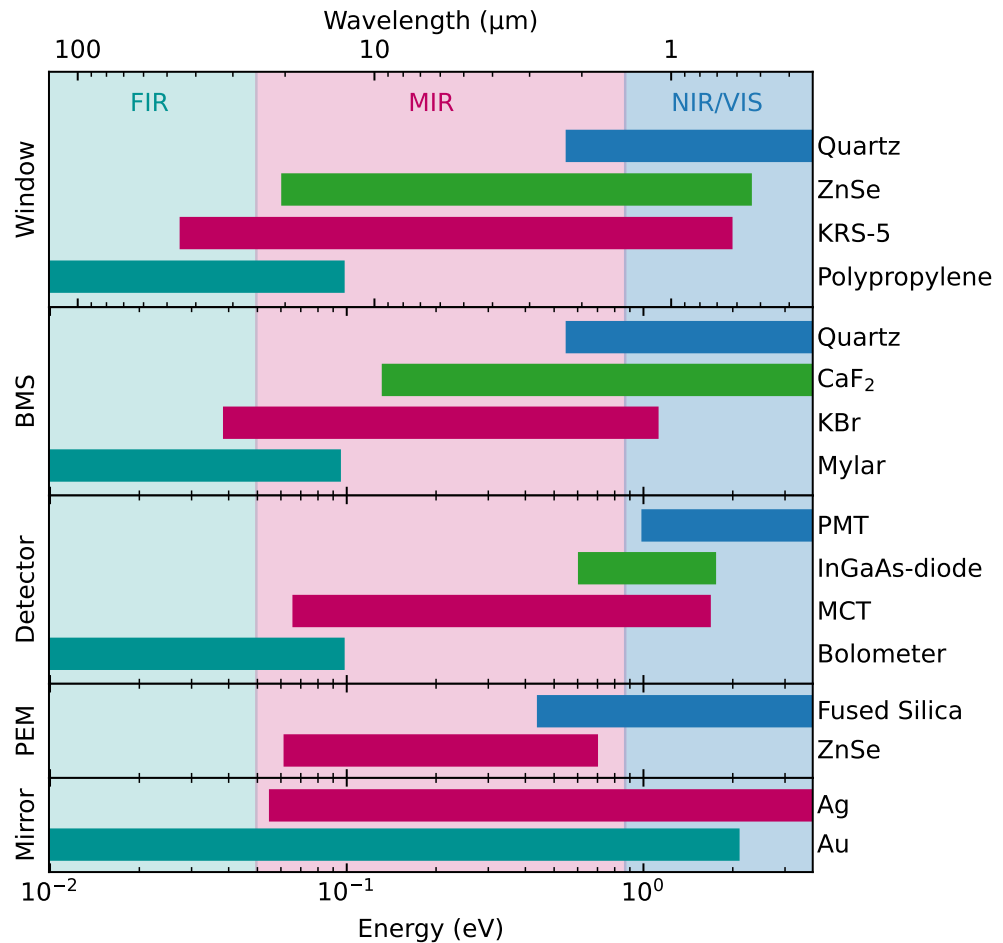
The polarisation modulation technique can be used in combination with monochromator or FTIR spectrometers. Due to available equipment, both techniques are employed. A summary of the optical components and materials used is shown in Fig. 2.9, grouped to the corresponding frequency range by the colour code. All setups are summarised in Fig. 2.10.

The NIR/VIS spectrometer employs an Oriel Instruments Cornerstone 260 grating monochromator (panel a). The light from a Xenon or a halogene lamp for VIS/NIR, respectively, is turned monochromatic by the grating. Subsequently, the beam is collimated by an array of lenses, made from BK7 glass or  $\text{CaF}_2$ , and shaped by an iris aperture (APT), before passing into the polarisation modulation setup. This consists of an initial polariser (P) set at  $45^\circ$ , the PEM (Hinds PEM 90, fused silica), an optional quarter–wave plate for the ellipticity calibration and an analyser (A), located after the sample (S). The polarisers are Glan–Thompson prisms made of Quartz. The sample is placed in an Oxford cryostat for temperature dependent recording which is equipped with a Quartz window and small NdFeB permanent magnets that provide 300 mT at the sample position and can be flipped by a rotation mechanism. The intensity is measured with a photomultiplier (PMT) or InGaAs diode. The detector signal is passed to a multimeter for the dc spectrum and two Lock–In amplifiers, set to measure the  $\omega_0$  and  $2\omega_0$  modulated components. The setup is operated from a PC with custom Labview software for data acquisition. Since all three intensity components necessary for evaluating the Kerr parameters are recorded simultaneously, only two measurement runs for opposite magnetic fields are needed at each temperature.

For the MIR setup, a Varian 670–IR spectrometer is used (panel b). It is based on a similar Michelson interferometer as the Vertex 80v. The source is a SiC globar, whose light is guided to an output port of the spectrometer housing, where the polarisation modulation setup is attached. Two off–axis parabolic mirrors collimate the light followed by the same arrangement of optical components from before, but now made from ZnSe (yellow). The polarisers are evaporated wiregrids on a ZnSe substrate and the light intensity is detected by a HgCdTe (MCT)

**Figure 2.9**

Configuration of optical components for the different frequency ranges indicated by the background shades. The colour encodes the range a device or material is typically used in. There is no commercial PEM solution for the FIR which makes the fixed polariser setup necessary.

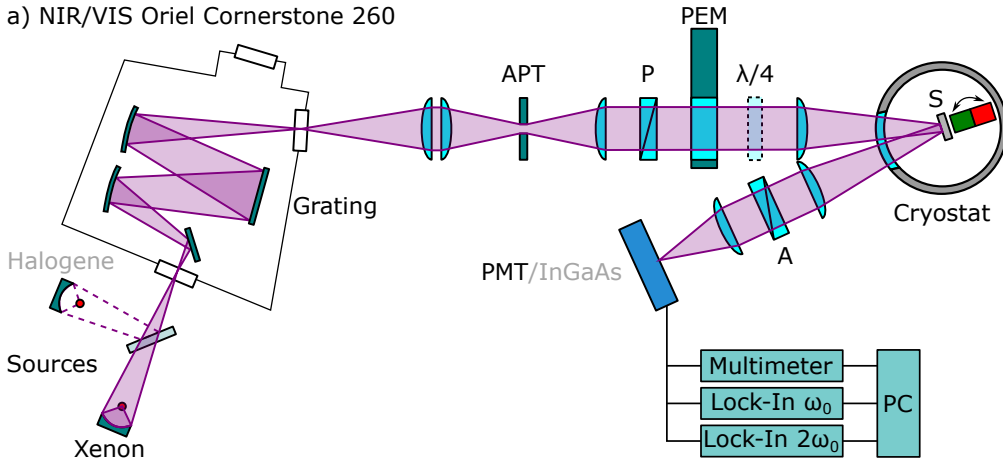


detector. Its signal is passed back to the spectrometer to record the interferogram. On a second input, a Lock-In amplifier is attached to demodulate at local oscillator frequencies to either  $\omega_0$  or  $2\omega_0$  providing the respective interferogram. Since the interferometer does not have a third input, the two components cannot be recorded simultaneously, so four measurement cycles are necessary per temperature to obtain the full information. The lightpath is placed in an acrylic box flushed with nitrogen to remove sharp absorption lines of water and  $\text{CO}_2$ .

In the FIR, we cannot use the polarisation modulation method, so a fixed polariser setup is attached to the output of the interferometer (panel c). The polarisers are wiregrids on a polypropylene substrate and the window is made from KRS-5 (red). Off-axis parabolic mirrors were used to guide the light and a bolometer operated at 4 K is the detector. Since the intensity is directly proportional to the Kerr rotation, the detector signal is fed directly to the spectrometer. Again, two measurements per temperature for opposite fields are recorded.

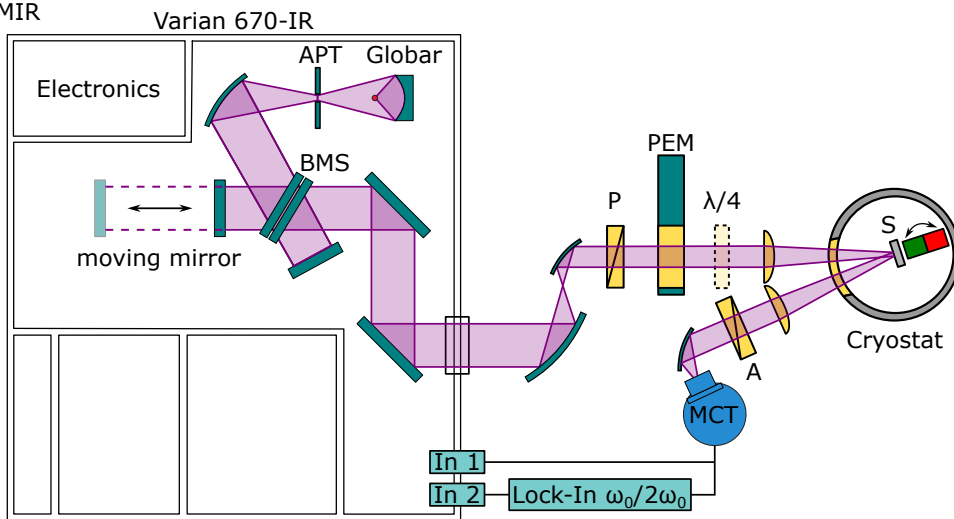
With the techniques described in this chapter, we are able to measure the full conductivity tensor in an energy range from 25 meV to 4 eV. This is the range where we would expect topological signatures of the band structure, especially in the optical Hall effect. So finally, we turn to the results of these experiments for kagome magnets.

a) NIR/VIS Oriel Cornerstone 260

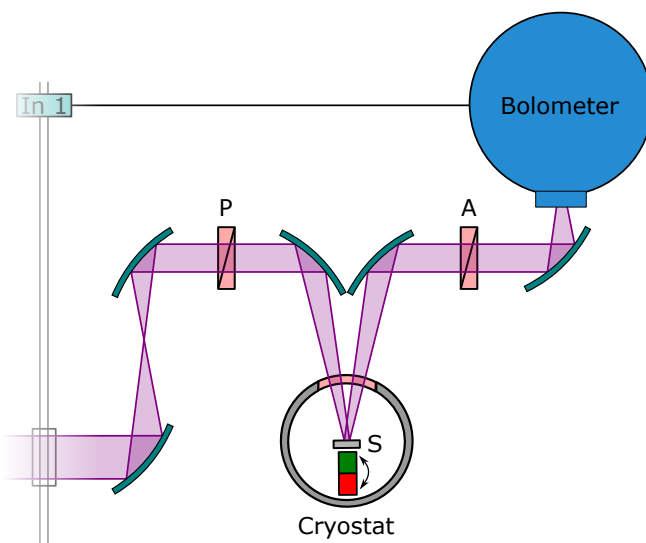
**Figure 2.10**

Summary of the MOKE spectroscopy setups. (a) The NIR/VIS spectrometer employing a Oriel Instruments Cornerstone 260. The operating principle is described in the main text. The abbreviations are: iris aperture (APT), polariser (P), quarter-wave plate ( $\lambda/4$ ), analyser (A) and sample (S). The blue colour of the optical components indicate their fabrication from Quartz glass and its derivatives. (b) The MIR setup based on a Varian 670-IR FTIR. In principle, the same optical components are used, but here made from ZnSe (yellow). (c) The FIR lightpath is also attached to the Varian FTIR. The optical components are shown in red because of the used KRS-5 window and polypropylene polarisers.

b) MIR



c) FIR





## Giant Magneto–Optical Response of a Nodal Line Resonance in $\text{Co}_3\text{Sn}_2\text{S}_2$

Previously, we have seen that a WSM phase can arise in materials composed of stacked ferromagnetic kagome layers. A prototypical example for this construction is the shandite  $\text{Co}_3\text{Sn}_2\text{S}_2$ , for which we investigate the magneto–optical properties in this chapter. Here, the  $ab$  plane Co kagome layers are stacked along the  $c$  axis in an  $ABC$ –fashion, resulting in the space–group  $R\bar{3}m$  [55]. A representative section of the crystal structure is shown in Fig. 3.1(a). Below  $T_C = 177$  K,  $\text{Co}_3\text{Sn}_2\text{S}_2$  becomes an easy–axis ferromagnet with the moments of the Co atoms pointing along the  $c$  axis. Originally, anomalies in the magnetisation and susceptibility as well as muon spin resonance ( $\mu\text{SR}$ ) spectra suggested an in–plane antiferromagnetic component just below the transition temperature [56, 57], whereas recent neutron diffraction and MOKE microscopy results show that the domain configuration changes instead [58, 59]. We therefore do not expect any topological Hall effect from real–space Berry curvature.

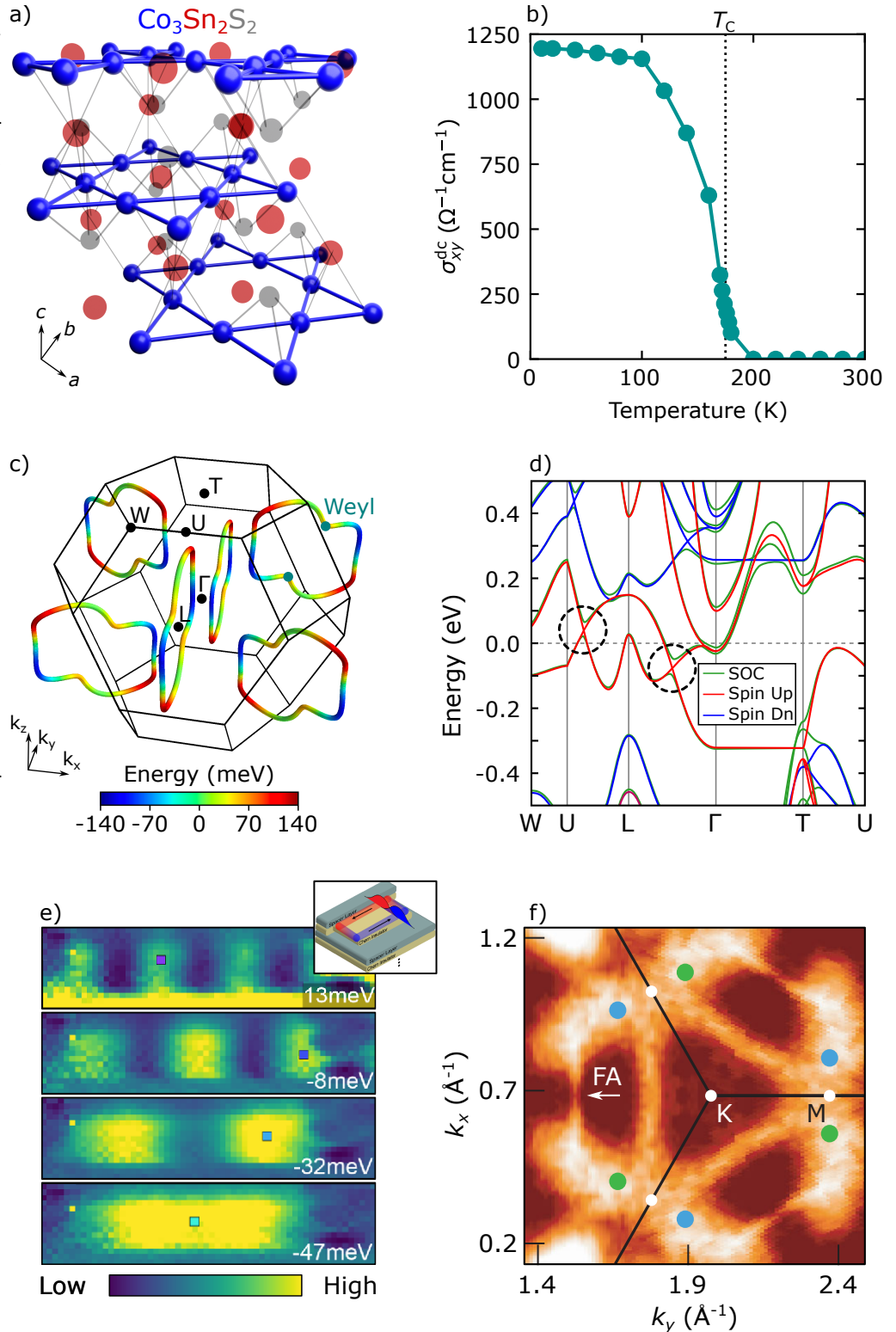
The non–trivial electronic topology under broken time–reversal symmetry was heavily investigated in this material. The band structure obtained from non–relativistic density functional theory (DFT) calculations along high–symmetry directions is presented in Fig. 3.1(d) which reveals a closed nodal line formed by the two red spin up bands around the Fermi energy. The evolution of the loops on high–symmetry planes of the BZ is shown in panel (c), where the colouring encodes the position of the crossing relative to Fermi energy  $E_F$ . When spin–orbit coupling (SOC) is included, each nodal line is gapped to a remaining pair of Weyl points at positions indicated in (c), about 60 meV away from  $E_F$  [60–62]. On the surface, linear band degeneracies were observed in angle resolved photoemission spectroscopy (ARPES) studies which also suggest the existence of Fermi arcs (see Fig. 3.1(f)) [63, 64]. Scanning tunnelling microscopy (STM) studies found chiral edge modes and observed their hybridisation on crystal terraces [18], shown in Fig. 3.1(e). Therefore, the overall experimental evidence indeed suggests that  $\text{Co}_3\text{Sn}_2\text{S}_2$  is a magnetic Weyl semimetal.

**Nodal loops and Weyl points**

Further interest in the consequences of this topological state was raised as a large anomalous Hall conductivity was measured in this material [60, 65]. The corresponding magneto–transport data is shown in Fig. 3.1(b) [62]. Earlier magneto–optical and theoretical studies suggest that the origin of this anomalous response is the gapped nodal line [61, 66], while an ARPES study claims that the Weyl points are the governing feature [60], but neither succeeded in observing the responsible interband transitions directly due to the vicinity of the topological features to the Fermi energy. It therefore remained unclear whether the Weyl points or the nodal loops give the dominant contribution to the static AHE, and whether extrinsic scattering mechanisms play a crucial role. Both of these questions could be addressed by the broadband MOKE study performed in the course of this thesis which is presented in the following.

**Figure 3.1**

Topological properties of  $\text{Co}_3\text{Sn}_2\text{S}_2$ . (a) Crystal structure highlighting the  $ABC$ -stacked Co kagome layer sequence. (b) Giant AHE with values up to  $1200 \Omega^{-1}\text{cm}^{-1}$  at low temperatures. (c) Nodal loops on high-symmetry planes of the BZ, the colour scale encodes the position of the crossing relative to the Fermi energy. When SOC is included, each nodal line is gapped to a pair of Weyl nodes  $60\text{meV}$  away from the Fermi energy, as indicated for the top right loop. (d) Band structure along high-symmetry directions with and without SOC. The band crossings of the nodal loop are highlighted with dashed circles (adapted from [62]). (e) STM images of hybridised edge states on a crystal terrace of  $\text{Co}_3\text{Sn}_2\text{S}_2$  with particle in a box behaviour (Reproduced Fig. 3(c-f) and 4(b) from S. Howard *et al.*, *Nature Communications* **12**, 4269 (2021) under Creative Commons license). (f) ARPES constant energy contour at the Fermi level. Features connecting Weyl points of opposite chirality (blue/green dots) are identified as Fermi arcs (FA) (Reprinted Fig. 4(a) with permission from I. Belopolski *et al.*, *Physical Review Letters* **127**, 256403 (2021), Copyright 2021 by the American Physical Society).



### 3.1 Reflectivity and Kerr Effect Spectra

In the magnetically ordered phase, the conductivity tensor in  $\text{Co}_3\text{Sn}_2\text{S}_2$  takes the form

$$\hat{\sigma}(\omega) = \begin{pmatrix} \sigma_{xx}(\omega) & \sigma_{xy}(\omega) & 0 \\ -\sigma_{xy}(\omega) & \sigma_{xx}(\omega) & 0 \\ 0 & 0 & \sigma_{zz}(\omega) \end{pmatrix} \quad (3.1)$$

due to symmetry (for better readability, the explicit frequency dependence of the quantities is omitted in the following). Here, the  $z$  coordinate aligns with the  $c$  axis of the crystal, while  $x$  and  $y$  lie in the kagome plane. Determining all tensor elements therefore requires polarised reflectivity measurements parallel and perpendicular to the kagome layer. These measurements were carried out on the polished  $ab$  and  $ac$  surfaces of single crystals with a lateral sizes of  $\approx 5$  mm and  $\approx 3$  mm, respectively. The individual samples were cut from a large single crystal which was grown by Mohamed Kassem at the group of Hiroyuki Nakamura with a modified Bridgman method [67, 68]. The high quality and stoichiometric chemical composition of the crystal were confirmed by powder x-ray diffraction and spectroscopy. The samples were glued on copper plates with circular apertures of 5 and 3 mm diameter, respectively, which were mounted on the coldfinger of a Cryovac Helium-flow cryostat for temperature dependent measurements down to 10 K. The MIR-VIS spectra were recorded in a Bruker IFS66v/S FTIR spectrometer and the FIR range was covered with a Bruker Vertex 80v. On the low-energy side, the reflectivity spectra were extrapolated by using the dc conductivity values. For the UV, the spectra were merged with a single high-temperature UV spectrum ranging up to 4 eV and then extrapolated with free electron behaviour setting in at  $10^6 \text{ cm}^{-1}$  and an exponent for the high-frequency regime of 1.5. The broadband MOKE spectra were measured on the same  $ab$  cut crystal in the spectrometers described in Sec. 2.3.3. Because of the large uniaxial anisotropy, the sample had to be field-cooled to reverse the magnetisation direction and allow the antisymmetrisation of the MOKE angles. In addition, the strong anisotropy results only in a small magnetisation component in the kagome plane for the available magnetic fields, so no MOKE spectra were recorded on the  $ac$  plane.

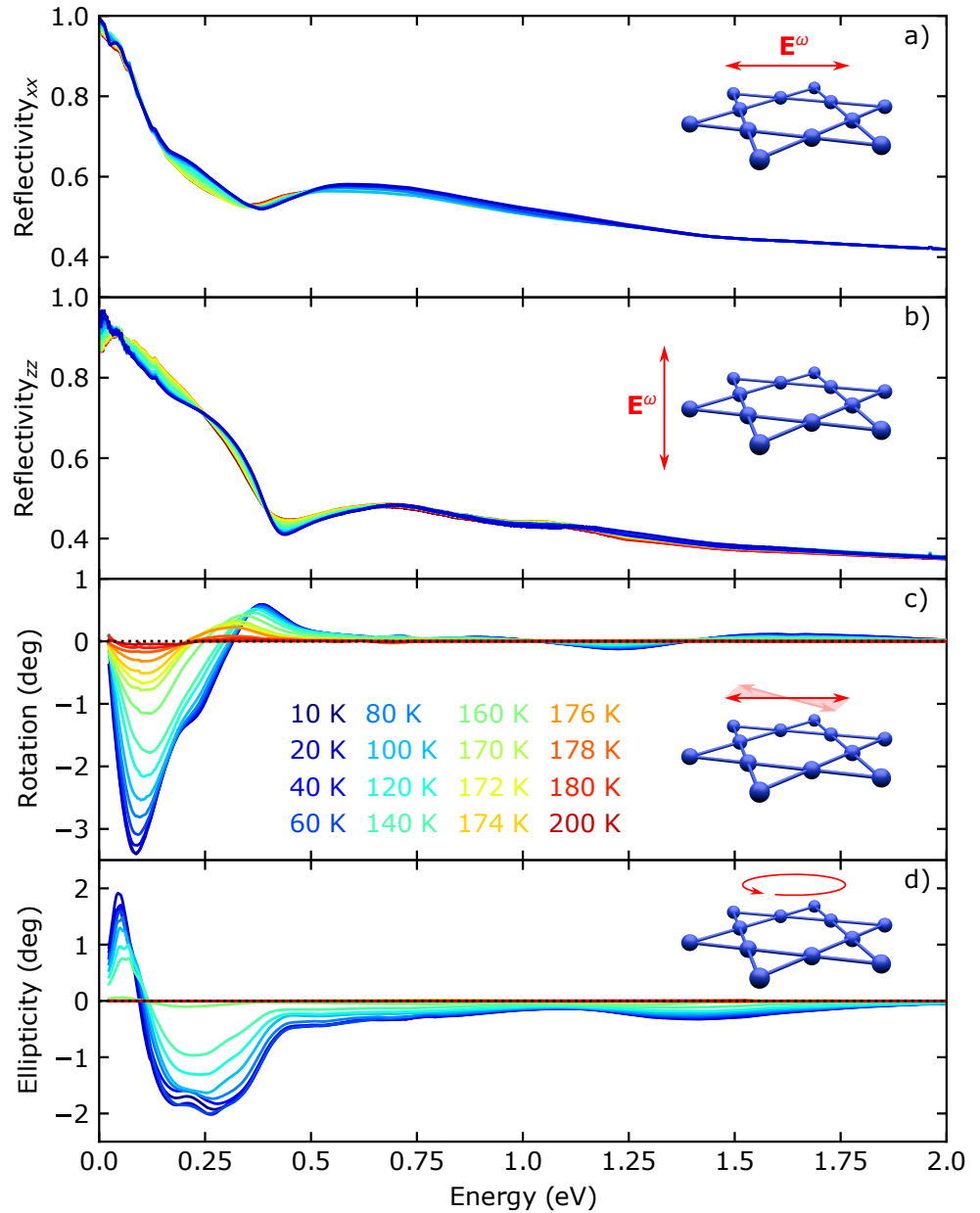
The obtained reflectivity and MOKE spectra for temperatures between 10–200 K are shown in Fig. 3.2. Both reflectivities approach unity towards zero frequency, implying metallic character. The  $ab$  plane spectra in panel (a) drop sharply around 0.125 eV, followed by a local, slightly temperature dependent minimum around 0.4 eV, agreeing with the spectra published in Ref. 69. For the  $c$  direction (panel (b)), the reflectivity drops significantly for temperatures above 100 K in the  $\omega \rightarrow 0$  limit, with a small peak forming around 40 meV. For higher energies, the spectra decrease towards a local minimum at 0.45 eV which becomes sharper at low temperatures. Above 0.7 eV there is no significant temperature dependence. We therefore observe a clear optical anisotropy which reflects the layered crystal structure.

Panels (c) and (d) show the Kerr rotation and ellipticity, respectively. Beside a small paramagnetic contribution, we start to detect a finite Kerr effect only below  $T_C$  due to the required broken time-reversal symmetry. Above 0.5 eV, both Kerr parameters are small showing several sign changes. By contrast, we observe giant Kerr effect in the low-energy range where the rotation shows a global minimum of  $-3.3^\circ$  at 90 meV for low temperatures. The corresponding feature in the ellipticity is a sequence of a peak at 50 meV up to  $2^\circ$  followed by a clear

**Giant MOKE**

**Figure 3.2**

Reflectivities and Kerr parameters for  $\text{Co}_3\text{Sn}_2\text{S}_2$ . (a) Reflectivity in and (b) perpendicular to the kagome plane. The insets highlight the measurement geometry. The optical anisotropy for in- vs. out-of-plane directions is evident. Kerr rotation (c) and ellipticity (d) spectra measured on the  $ab$  plane, showing giant magneto–optical activity in the energy range of the nodal line (adapted from [62]).



sign change and a broad minimum with  $-2^\circ$  at 0.25 eV. Comparing with the colour scale of Fig. 3.1(c), it is evident that this giant magneto–optical response appears in the energy range of the nodal line. These MOKE spectra agree with those published in Ref. 66 in the overlapping energy range, but have a lower cutoff energy of 25 meV compared to former 80 meV due to the FIR extension. Importantly, the measured Kerr effect spectra follow the Kramers–Kronig relation [70] and both angles approach 0 for  $\omega \rightarrow 0$ . This is also evident from Eq. 1.50, where the denominator makes the Kerr angles vanish with  $\sqrt{1/\omega}$ .

The temperature dependence of the MOKE spectra can have several contributions. To linear order, the polar Kerr effect is proportional to the out-of-plane magnetisation. In addition, it is sensitive to the temperature evolution of the band structure. In  $\text{Co}_3\text{Sn}_2\text{S}_2$ , ARPES studies suggest that in the paramagnetic phase, a 4-fold degenerate Dirac nodal loop exists, which upon the magnetic transition is exchange split into two 2-fold degenerate Weyl loops [63]. One of

them moves away from the Fermi energy remaining unoccupied, it's partner being the loop discussed in Fig. 3.1. The evolution of the latter will therefore influence the temperature dependence of the low-energy MOKE spectra. An earlier theoretical study further suggests that the Weyl point separation evolves as function of the ordered moment, inheriting the temperature dependence of the magnetisation. As discussed in Sec. 1.2.3, the node separation will influence the AHE and in turn the MOKE, but their position in energy depends on the loop evolution, complicating the resulting temperature dependence. Therefore, a quantitative separation of these influences would require detailed knowledge of the temperature evolution of the band structure. Due to the difficulties of including temperature on the theoretical level, this goes beyond the scope of the present work.

From the four presented spectral quantities, we can obtain the diagonal conductivity elements as described in Sec. 2.1 and derive the off-diagonal conductivity via Eq. 1.50, so these tensor elements are presented next.

### 3.2 Optical Conductivity and its Anisotropy

Fig. 3.3 shows the independent components of the conductivity tensor. The main panels focus on the spectra below 0.2 eV where the static conductivity values are presented for comparison as coloured squares at zero frequency, while the insets show the spectra on a broad energy range.

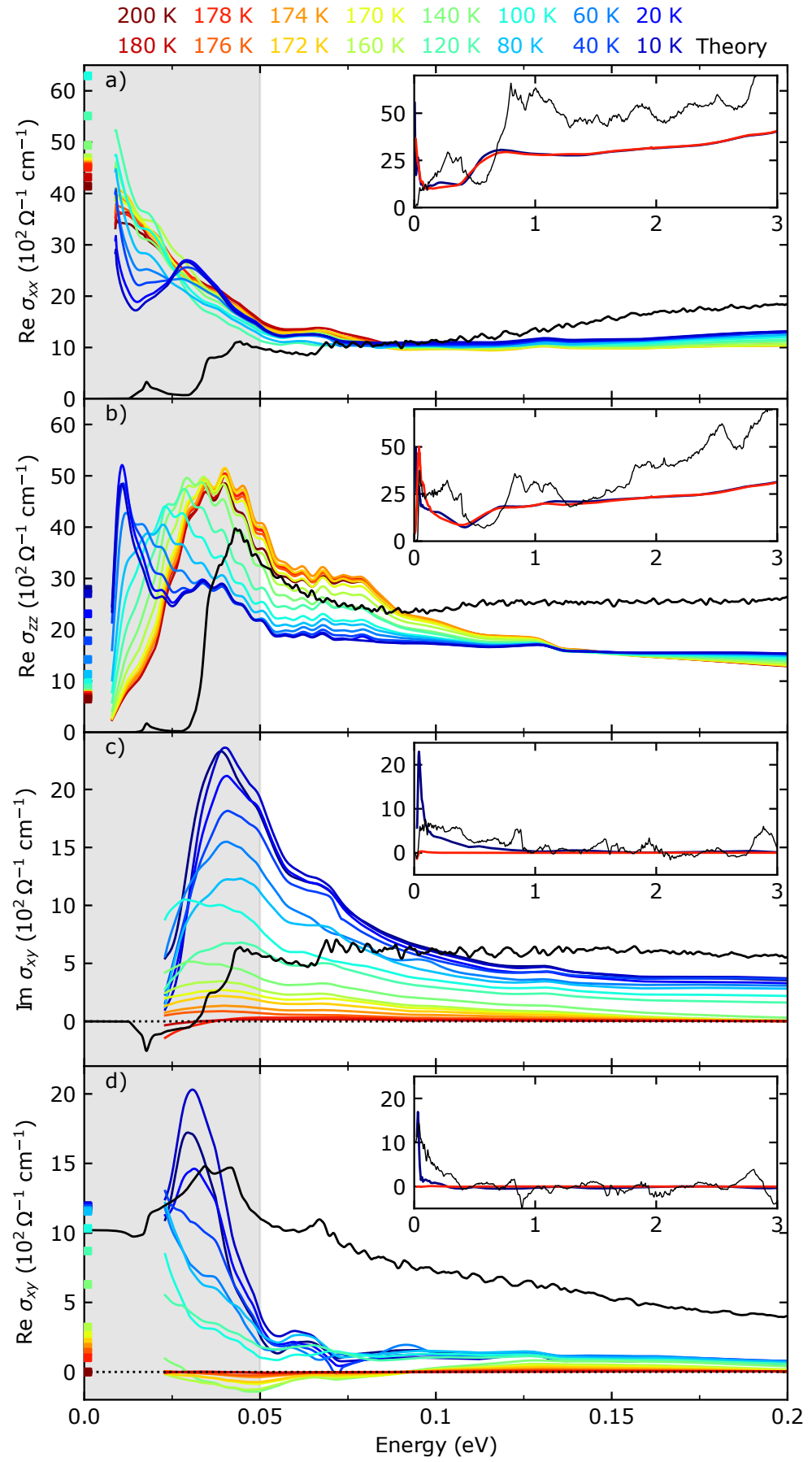
Due to the itinerant character,  $\text{Re } \sigma_{xx}$  in panel (a) shows a Drude component for  $\omega \rightarrow 0$  which becomes sharper at low temperatures and extrapolates the spectra to the static values. For temperatures below 80 K, a peak is forming at 30 meV clearly separated from the free carrier response. At higher energies, a temperature dependent hump appears at 250 meV followed by a step edge at 0.6 eV before the spectra become flat without distinct temperature dependence. The observed spectral shape agrees with earlier publications [66, 69, 71].

A novel finding of this thesis work are the spectra for  $\sigma_{zz}$ , their real part shown in panel (b). Most interestingly, they differ strongly from  $\sigma_{xx}$  as we do not find a Drude component down to the spectral cutoff, although a narrow peak in the unresolved region might again extrapolate to the dc values. This observation points to different conduction mechanisms. While within the kagome plane, the orbital overlap results in coherent conduction, interlayer electron motion is hindered only producing incoherent hopping, similar to the situation along and perpendicular to the Vanadium chains in BaVS<sub>3</sub> [72]. At higher energies, we observe a peak at 40 meV at 200 K which broadens and shifts to smaller energies upon lowering the temperature. Eventually, it splits in two below 80 K. Around 0.4 eV, a minimum forms. On its low energy slope, a similar temperature dependent hump is visible as in  $\text{Re } \sigma_{xx}$  and its high energy side resembles the step edge. For even higher energies,  $\text{Re } \sigma_{zz}$  is monotonously increasing without temperature dependence, again similar to  $\sigma_{xx}$ .

Finally, the imaginary and real parts of the Hall conductivity spectra,  $\text{Im } \sigma_{xy}$  and  $\text{Re } \sigma_{xy}$ , are shown in panels (c) & (d), respectively. Similar to the Kerr parameters, both are rather small and featureless at high energies, but show dramatic resonances below 0.1 eV. Importantly, it's worth to emphasise that this far-infrared range was not covered by a former magneto-optical study [66], but was directly observed here due to the development of the FIR MOKE setup to reveal this striking low-energy optical Hall response. In  $\text{Im } \sigma_{xy}$ , a peak forms

**Figure 3.3**

Conductivity tensor elements for  $\text{Co}_3\text{Sn}_2\text{S}_2$ . Comparison of the spectra measured between 10 and 200 K (coloured lines) and the theoretical DFT spectra (black lines). (a,b,c) and (d) respectively show the real parts of the diagonal,  $\text{Re } \sigma_{xx}$  and  $\text{Re } \sigma_{zz}$ , as well as the imaginary and real part of the off-diagonal conductivity spectra,  $\text{Im } \sigma_{xy}$  and  $\text{Re } \sigma_{xy}$ . The static conductivity values are plotted for comparison as coloured squares at zero energy. The insets show the respective spectrum on a broad energy range (adapted from [62]).



at 40 meV which becomes larger for low temperatures, with the spectra turning to 0 towards the cutoff (25 meV). The related lineshape in  $\text{Re } \sigma_{xy}$  is an upturn which at temperatures below 60 K becomes a peak with a magnitude as high as  $2000 \Omega^{-1} \text{cm}^{-1}$ , overshooting the dc AHE. Since the low-energy tail of the spectra agrees well with the dc values and formerly published terahertz spectroscopy data is featureless [66], no additional excitations are expected in the small uncovered energy window. In addition, a Drude fit suggests a width smaller than 10 meV at low temperatures, hence we do not expect that impurity scattering contributes to the AHE above this frequency. Since this width is smaller than the experimental cutoff for  $\sigma_{xy}$ , the optical weight produced by the resonance has purely intrinsic origin, and its magnitude at the cutoff consequently suggests that it yields the dominant contribution to the AHE.

### Giant FIR Hall conductivity

In order to elucidate the interband transition generating the resonance, Ming-Chun Jiang at the group of Ryotaro Arita performed *ab initio* calculations yielding all tensor elements (details for the calculations may be found in Ref. 62). The respective theoretical spectra are shown by black lines together with the experiments in Fig. 3.3. Despite the Drude contribution which is not included in the theory, all components are qualitatively well reproduced over the broad energy scale. Differences include a slight shift of the features to higher energies which may be caused by correlation effects [71] and an overestimated optical weight for the diagonal elements. In both  $\text{Re } \sigma_{xx}$  and  $\text{Re } \sigma_{zz}$ , the hump around 0.25 eV and the step edge are captured, as well as the peak at 40 meV. In the Hall effect spectra,  $\text{Im } \sigma_{xy}$  shows a sudden increase at 40 meV although the resonance is not as pronounced as in the experiment. Importantly, the peak at 34.3 meV is very well captured in  $\text{Re } \sigma_{xy}$  though the experiment is a bit sharper, likely again due to correlations [71]. The dc extrapolation yields a similar AHE as for the low-temperature magneto-transport experiments. Based on this agreement, we are now able to identify which bands in which part of the BZ generate the low-energy resonance.

### 3.3 Decomposition of the Optical Hall Effect

In order to identify the locations in the BZ where the optical Hall effect is generated, we can revisit Eq. 1.52. If we split the matrix elements of  $p_{\pm}$  into the  $p_x$  and  $p_y$  components, we can rewrite them with the Berry connection using

$$\langle n, \mathbf{k} | \mathbf{p} | n', \mathbf{k} \rangle = -im/\hbar \cdot (\varepsilon_{n'}(\mathbf{k}) - \varepsilon_n(\mathbf{k})) \mathcal{A}_{nn'}(\mathbf{k}). \quad (3.2)$$

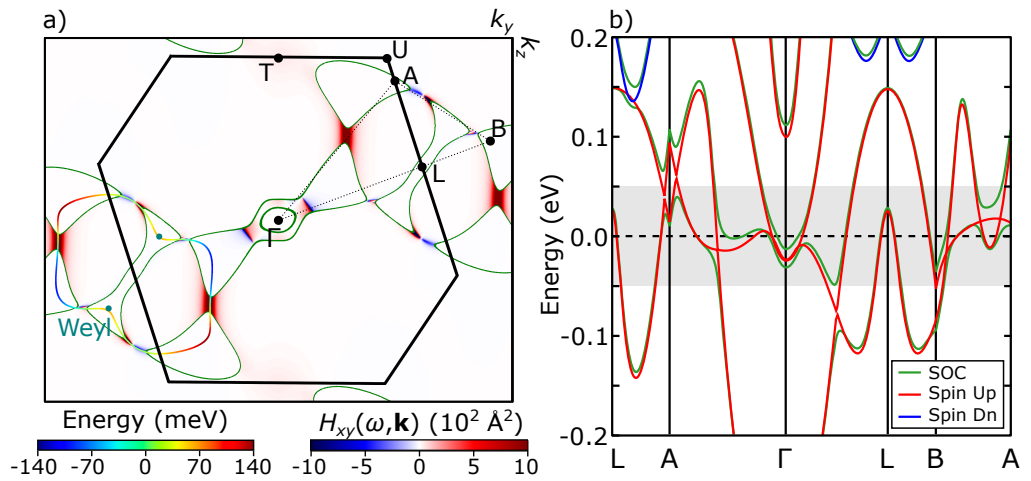
Summarising the prefactors, this yields

$$\begin{aligned} \sigma_{\alpha\beta}(\omega) &= \frac{ie^2}{\hbar V} \sum_{\mathbf{k}, n, n'} (f_{n'}(\mathbf{k}) - f_n(\mathbf{k})) \cdot \left( \frac{\varepsilon_{n'}(\mathbf{k}) - \varepsilon_n(\mathbf{k})}{\varepsilon_{n'}(\mathbf{k}) - \varepsilon_n(\mathbf{k}) - \hbar\omega} \right) \mathcal{A}_{nn'}^{\alpha}(\mathbf{k}) \mathcal{A}_{nn'}^{\beta}(\mathbf{k}) = \\ &= \frac{ie^2}{\hbar V} \sum_{\mathbf{k}} H_{\alpha\beta}(\omega, \mathbf{k}). \end{aligned} \quad (3.3)$$

$\alpha, \beta$  are indices for the Cartesian coordinates,  $V$  is the cell volume,  $f_n(\mathbf{k}) = f(\varepsilon_n(\mathbf{k}))$  is the Fermi-Dirac distribution function and  $\omega$  is the light frequency. With the last equality, we sum over the band indices taking into account transitions from filled to empty states and introduce the resulting quantity as the Hall spectral weight  $H_{xy}(\omega, \mathbf{k})$  which contains the momentum distribution of the off-diagonal conductivity. This relation resembles Eq. 1.33 after the summation over all bands

**Figure 3.4**

Momentum decomposition of the 34.3 meV resonance peak. (a) The Hall spectral weight of the calculated 34.3 meV peak on the mirror plane containing the nodal line and Weyl points. The colour scale of the nodal line is repeated for clarity. (b) Band structure along the triangle in (a). The grey shading highlights the energy range below 50 meV, same as in Fig. 3.3. The non–high–symmetry points A and B are (0.0, 0.4002, 0.301) and (0.0, 0.7373, 0.0) in units of the reciprocal lattice vectors (adapted from [62]).



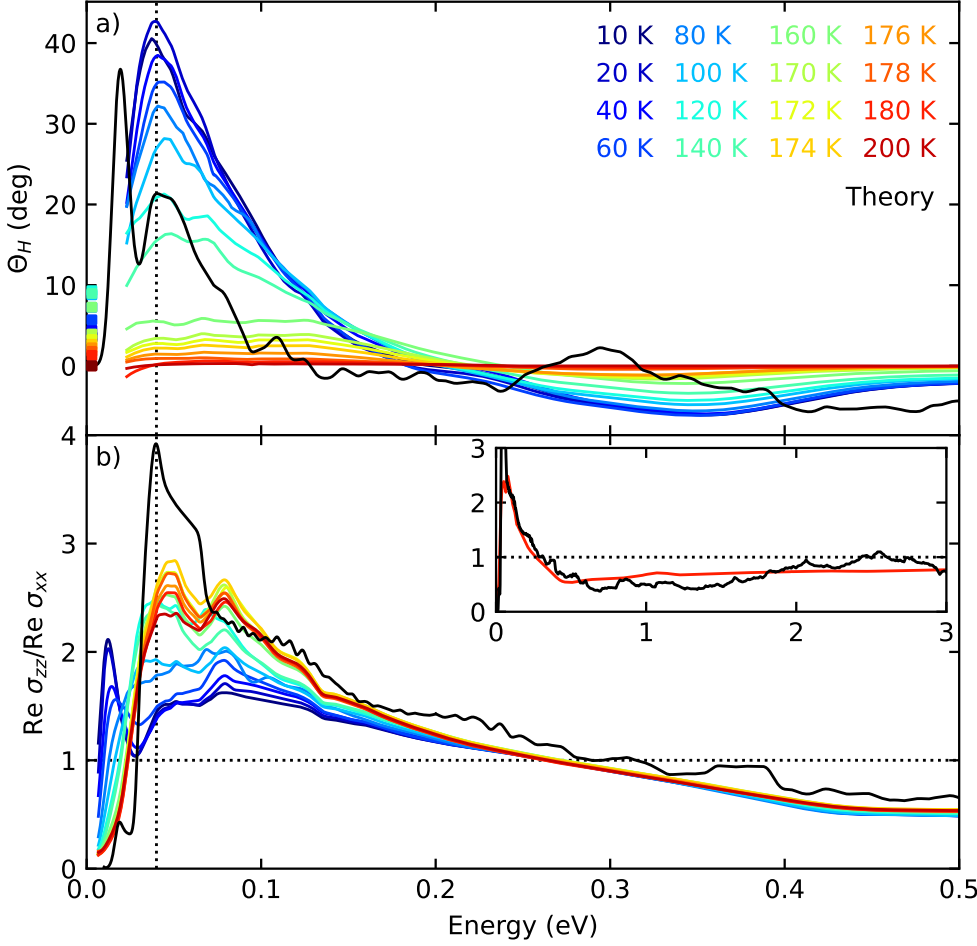
was performed, giving the Hall spectral weight the same unit as the Berry curvature  $\text{\AA}^2$ . Fig. 3.4(a) shows the Hall spectral weight of the 34.3 meV peak on one of the high–symmetry planes of the BZ which includes the nodal loops and Weyl points. These are exemplarily indicated on the bottom left by the rainbow line and green dots, respectively. The solid black line marks the boundary of the BZ, the green lines display the Fermi surface and the colour code shows the spectral weight. A numerical calculation of the Fermi surface verifies that all band crossings are found on the mirror plane, hence all low–energy features originate from the presented slice of the BZ.

There are several hotspots of Hall conductivity on the mirror plane. Close to A and in the vicinity of  $\Gamma$ , we find positive and negative patches next to each other. After integration over the BZ, the contribution from these hotspots will therefore cancel to a large extent. By contrast, the large positive patch along the  $\Gamma$ –A line does not have a negative partner and yields the dominant contribution to the peak. Interestingly, aside from the patches around  $\Gamma$ , we always find a hotspot when the nodal line comes close to or crosses the Fermi energy. These segments of the loop are indicated by light green of the rainbow in the lower left corner of Fig. 3.4(a). Therefore the hotspots always connect to dark green lines of the Fermi surface. Remarkably, we do not see any contribution at the location of the Weyl points. Comparing with the colour scale of the nodal line, they are located about 60 meV above the Fermi energy, hence cannot contribute to the optical weight of the peak and may only yield a sharp contribution in a small  $\mathbf{k}$ –volume.

In order to see the underlying band structure for the hotspots, Fig. 3.4(b) plots the bands along the A–B– $\Gamma$  triangle in panel (a). The grey shading indicates the low–energy range, same as in Fig. 3.3. The A–B line cuts through a sequence of a negative and positive hotspot. In the band structure, the two red spin up bands of the nodal loop are close to the Fermi energy, so with SOC, one of the bands is filled and the other is empty between the crossings, allowing the optical transition. The two crossings have opposite tilt which is the reason for the different sign in the optical weight, as discussed in Sec. 1.3.1. A similar situation produces the hotspots at  $\Gamma$  where we again observe two inverted spin–up bands with opposite tilt, gapped by SOC.

By contrast, we find only a single strongly tilted crossing point for the large positive patch on the  $\Gamma$ –A line. The SOC gap again provides the conditions for the

### Hotspots of the nodal line at the Fermi energy

**Figure 3.5**

(a) Hall angle spectrum  $\Theta_H = \arctan \text{Re}(\sigma_{xy}/\sigma_{xx})$  with a maximum of  $42.7^\circ$  at 40 meV. The underlying interband transition is almost fully circularly polarised, yielding the nodal line resonance. (b) Optical anisotropy spectrum  $\text{Re } \sigma_{zz} / \text{Re } \sigma_{xx}$  of  $\text{Co}_3\text{Sn}_2\text{S}_2$ . In the energy range of the nodal line resonance, the out-of-plane conductivity is significantly enhanced (adapted from [62]).

optical transitions, specifically, the strong tilt produces two almost parallel bands around the Fermi energy. Therefore, the energy gap stays almost constant in a relatively large  $\mathbf{k}$ -interval which sums up the Berry curvature of the two bands in a small energy window which results in the large patch of optical weight. A total of 6 such hotspots are expected in the BZ due to inversion and 3-fold rotational symmetry, which combined yield the dominant contribution to the peak in the optical Hall conductivity and therefore the AHE. Here, SOC plays a crucial role as without the gap, the hotspots would not appear. Hence, the magneto-optical response is amplified by SOC although the linear band degeneracy disappears.

With this knowledge, we can now come back to the conductivity tensor and evaluate the influence of this feature for the optical properties.

### 3.4 Fingerprints of the Nodal Line in the Conductivity Tensor

We can start by comparing the diagonal and off-diagonal conductivity by calculating the Hall angle spectra  $\Theta_H = \arctan \text{Re}(\sigma_{xy}/\sigma_{xx})$  as shown in Fig. 3.5(a). At 40 meV, we observe a very large Hall angle of  $42.7^\circ$ , indicating that the two conductivity elements have almost equal magnitude. If we employ the Kubo formula in the form of Eqs. 1.51 and 1.52,  $\sigma_{xy}$  depends on the difference of the two circular matrix elements, whereas  $\sigma_{xx}$  is given by their sum. Although the Hall angle as defined above is not limited, the ratio  $\text{Im } \sigma_{xy} / \text{Re } \sigma_{xx}$  cannot exceed

1, corresponding to a completely circularly polarised transition. This limiting case is almost realised in the nodal line resonance of  $\text{Co}_3\text{Sn}_2\text{S}_2$ .

This resonance has another profound implication. If we compare the in- and out-of-plane conductivities by calculating linear optical anisotropy spectra  $\text{Re } \sigma_{zz} / \text{Re } \sigma_{xx}$  as shown in Fig. 3.5(b),  $\sigma_{zz}$  is significantly enhanced in the energy range of the resonance, becoming almost three times larger than  $\sigma_{xx}$ . This behaviour is also captured by the first-principles calculation, where the overestimated optical weight for the individual components is cancelled by taking the ratio, yielding very nice agreement with the experimental data at high temperatures. For low temperatures, some of the optical weight splits off and moves to lower energies, nevertheless  $\sigma_{zz}$  still stays larger at the resonance. Since topological features usually require a band inversion, transitions between the two bands have very specific selection rules and the topological character prevents the orbitals to hybridise. Together, these prerequisites may only be fulfilled by the experimental conditions for a specific orientation of the polarisation. This observation may introduce the optical anisotropy as a new signature of topological states.

These results lead us to the first thesis point.

### Thesis Point 1

On the itinerant kagome ferromagnet  $\text{Co}_3\text{Sn}_2\text{S}_2$ , I have measured the reflectivity spectra with in- and out-of-plane polarisation, and the magneto-optical Kerr effect (MOKE) spectra over a broad energy range from 25 meV to 3 eV. This required the development of a MOKE setup for the far-infrared spectral range, which I successfully realised by fixed polarisers for rotation measurements and a Kramers–Kronig constrained extrapolation of the ellipticity. Due to this extension, I could determine all elements of the conductivity tensor in this material for the specified energy range and capture the peaks caused by interband transitions of the gapped nodal line below 40 meV also in the off-diagonal component. Extrapolating to the dc values confirmed that the AHE in  $\text{Co}_3\text{Sn}_2\text{S}_2$  has dominantly intrinsic nature caused by the nodal line and that Weyl points only give vanishing contributions. By calculating the frequency dependent Hall angle, I could show that these features are caused by an almost fully circularly polarised nodal line resonance, which additionally enhances the optical anisotropy favouring the out-of-plane conductivity [62].

In this study, we used magneto-optical spectroscopy to probe the topological properties of the ground state electronic structure. Since the time-reversal symmetry breaking plays a crucial role for the emergence of topological band structures, naturally the question arises whether we can also control these features if we tune the ground state with external forces, so next we investigate the evolution of the nodal line resonance if we manipulate the magnetic state with external fields.

## Field–Induced Reconstruction of the Nodal Loop in $\text{Co}_3\text{Sn}_2\text{S}_2$

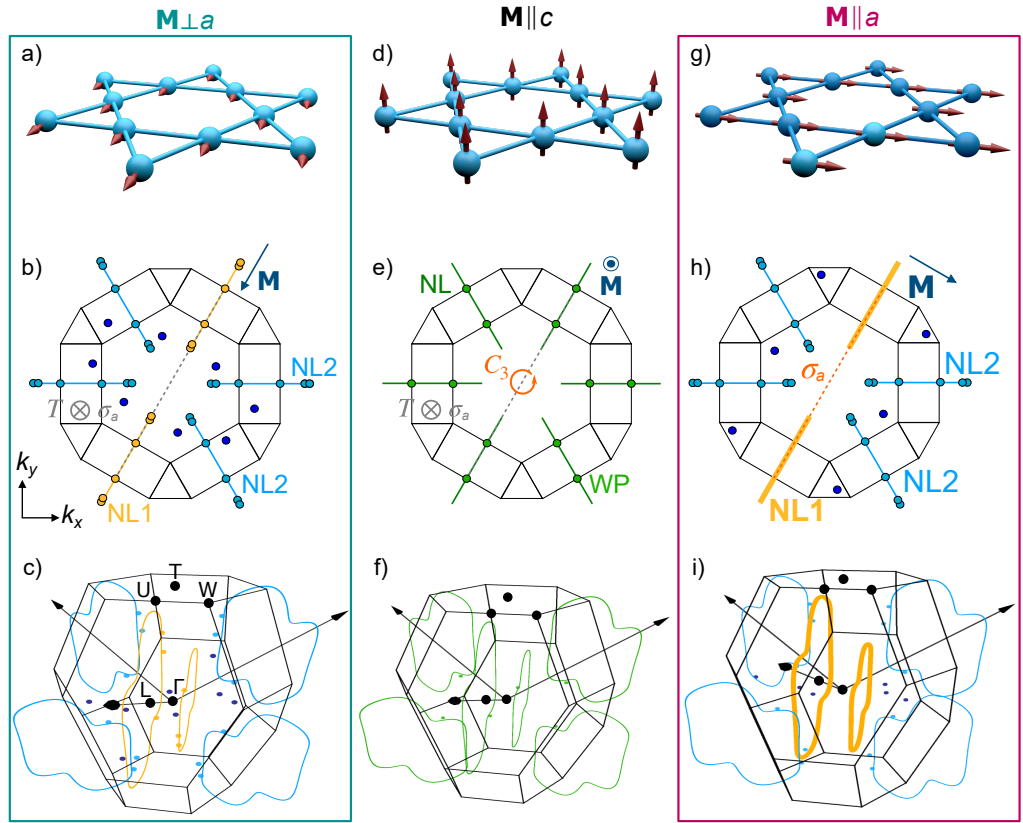
We have seen in the introductory chapter that the presence of topological states requires them to be protected by properties of the system, e. g. the band gap of a topological insulator or a certain symmetry as in the case of a nodal line semimetal. Since applications in spintronics and quantum information technology call for the on demand manipulation of the topological band structure, we require a handle on the protecting property through external stimuli. As was shown in the review by Ilan *et al.* [10], those can influence the topological band structure if they modify certain symmetries of the system, e. g. through uniaxial strain leading to an emergent effective electromagnetic field in the band Hamiltonian. In topological magnets, conveniently, external magnetic fields provide an efficient way to vary the electronic structure, if they can modify the magnetic ground state order.

A number of studies indeed predict that the number and position of Weyl nodes can depend on the magnitude and direction of the magnetic moments [12, 73–75]. Higher dimensional degenerate manifolds, e. g. nodal lines and planes may be gapped completely by magnetism together with SOC if non–symmorphic symmetries are altered by the field [26, 28, 65]. While these effects are well established on a theoretical basis, their experimental verification proves to be challenging. For example, STM on the kagome metal  $\text{Fe}_3\text{Sn}_2$  suggests a reconstruction of massive Dirac bands for out–of–plane vs. in–plane moments [76]. Similarly, in  $\text{EuP}_3$  magneto–transport experiments hint to the presence of a nodal ring or Weyl–semimetal phase for in– and out–of–plane fields, respectively [77]. Quantum oscillations, e. g. observed in transport, can also give insights into the field induced reconstruction of the Fermi surface, as was recently shown for  $\text{Co}_3\text{Sn}_2\text{S}_2$  [78]. In addition, it was shown for the nodal planes in  $\text{MnSi}$  that only bands on  $\mathbf{k}$  planes parallel to an externally applied magnetic field remain gapless [28]. While these examples indicate that the band structure in topological magnets can be highly sensitive to the magnetic state, they also highlight the difficulty to obtain the desired direct information about specific bands. Since ARPES cannot be performed in high external magnetic fields, we will employ magneto–optical spectroscopy to investigate the magnetic field control of electronic band topology.

Again,  $\text{Co}_3\text{Sn}_2\text{S}_2$  is a suitable material for this type of study due to the simple band structure at the Fermi level. With the dispersive nodal loop emerging across the ferromagnetic transition and its responsibility for large anomalous Hall, Nernst and magneto–optical effects [60–63, 66, 75], the topological band structure appears strongly coupled to the magnetic order in this kagome metal. Therefore, we will now investigate the evolution of the nodal line for magnetic field applied in the kagome plane by performing magneto–reflectance experiments up to 34 T.

**Figure 4.1**

Symmetries and topology for out-of- and in-plane magnetic field in  $\text{Co}_3\text{Sn}_2\text{S}_2$ . The first row (a,d,g) shows a real-space representation of the magnetisation for  $\mathbf{M} \perp a$ ,  $\mathbf{M} \parallel c$  and  $\mathbf{M} \parallel a$ . The second and third rows show a top and 3D view of the corresponding BZ for the respective configuration. (a–c) Emerging Weyl points (WP) for  $\mathbf{M} \perp a$ . The in-plane magnetisation makes the gapped nodal loops inequivalent (NL1/2) and produces additional Weyl points. Those have the same colour as their corresponding loop or are dark blue if located at other  $\mathbf{k}$  points. (d–f) Three equivalent nodal loops related by the  $C_3$  rotational symmetry for out-of-plane magnetisation. (g–i) Inequivalent nodal loops for  $\mathbf{M} \parallel a$ . For this configuration, the mirror plane  $\sigma_a$  is a symmetry and protects the nodal loop NL1 (thick yellow) from being gapped (adapted from [80]).



First, we consider the modification of symmetries by the in-plane field. For the ground state magnetisation  $\mathbf{M} \parallel c$ , all nodal loops are equivalent due to the  $C_3$  rotational symmetry, as shown in Fig. 4.1(d–f). We can therefore focus on one representative loop. However, for magnetisation in the kagome plane, the 3-fold rotational symmetry is broken. For  $\mathbf{M} \parallel a$ , this results in the magnetic point-group  $C2/m$ , which hosts a mirror plane  $\sigma_a$ . As shown in Fig. 4.1(g–i), this plane contains a nodal loop NL1 which will therefore be protected from being gapped by SOC (thick yellow). The remaining loops NL2 (light blue) are related by the mirror operation, but are not protected, hence they are gapped resulting in 6 Weyl points for each loop. Additionally, we find 6 Weyl points away from the nodal lines (dark blue). So in total we obtain 18 Weyl points and a protected nodal loop in the BZ. For the perpendicular in-plane direction  $\mathbf{M} \perp a$ , shown in panels (a–c), we obtain a similar situation, but here the magnetic point-group is  $C2'/m'$ . We therefore need to combine the mirror operation with time-reversal to obtain a symmetry. As this does not protect the loops NL1, they are gapped to 6 Weyl points by SOC. The remaining loops are similarly related by this operation and are again gapped to 6 Weyl points. Here we find 8 additional Weyl points away from the loops, so we obtain a total of 26 Weyl points distributed in the BZ. Some of these features were predicted earlier [75, 79], but a direct experimental investigation has been lacking, along with measurements of the physical consequences of their emergence. Therefore, the two following questions arise: Do the symmetry induced changes of the nodal lines show up in the optical response and do the additional Weyl nodes leave any fingerprints?

### Protected nodal loop

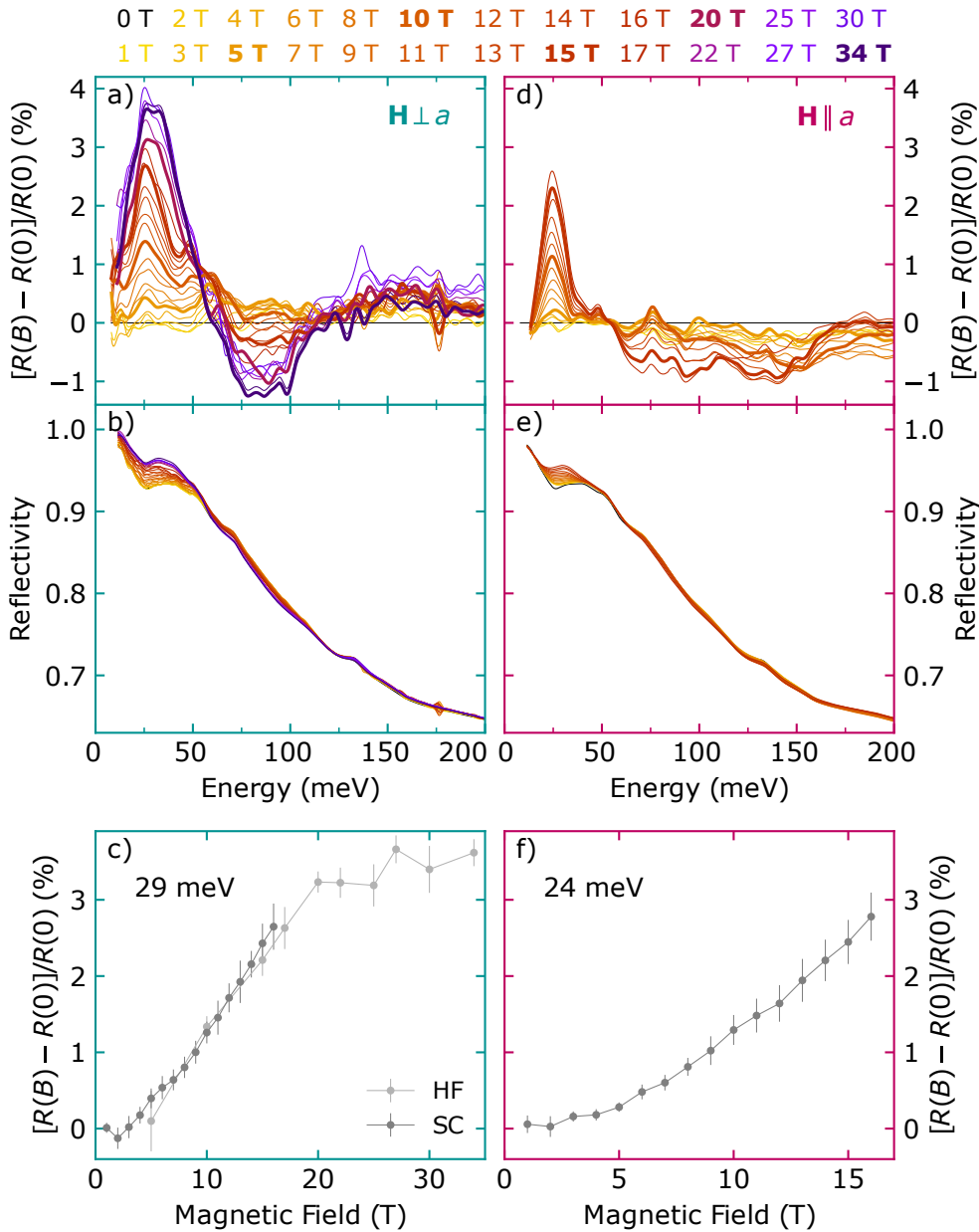


**Figure 4.2** Magneto-reflectance in  $\text{Co}_3\text{Sn}_2\text{S}_2$  up to 0.2 eV (a,d) Relative change of the reflectivity for in-plane magnetic fields perpendicular and along  $a$ , respectively. (b,e) Magneto-reflectance spectra calculated from the upper panels and the 10 K reflectivity data from Chapter 3. (c,f) Evolution of the magnitude of the low-energy peaks at 29 meV and 25 meV, respectively, for the SC and HF data sets (adapted from [80]).

## 4.1 High-Field Magneto-Reflection Measurements

For the magneto-reflectance experiments, the same large  $ab$  cut crystal as in the previous chapter was used. Relative magneto-reflectance data  $[R(B) - R(0)]/R(0)$  was collected in Voigt configuration and an external bolometer with the field aligned along and perpendicular to the in-plane  $a$  crystal axis in the setups described in Sec. 2.2. For this study, both the superconducting (SC) setup and the high-field resistive magnet (HF) were used for data collection. Due to the different optical path lengths in the SC and HF experiments, the raw signal is smaller in the HF data. Therefore, the HF data was scaled for comparison with the corresponding SC data sets at 5 and 10 T, while for 15 T and larger fields the 15 T SC data was used for scaling. The presented data for high fields therefore shows a lower limit for the actual magnitude of the effect.

The collected magneto-reflectance data up to 0.2 eV and fields up to 34 T is shown in Fig. 4.2. Since for low fields the magnetisation does not saturate in the plane, the datasets are labelled by the field direction  $\mathbf{H} \perp a$  and  $\mathbf{H} \parallel a$  for (a) and (d), respectively. Due to the limited measurement time at the high-field facility, the spectra for the latter configuration could only be collected in the SC setup up to 16 T. For both configurations, we obtain similar spectra, but the detailed line shapes are slightly different. With increasing magnetic field, a peak develops at low energies, followed by a broad minimum. For  $\mathbf{H} \perp a$ , these two features are located around 29 meV and 85 meV, while the peak is shifted to lower energies of 25 meV and the minimum broadens for the perpendicular direction. For both configurations, the changes approach 0 at the high-energy cutoff. This allows to multiply the data onto the low-temperature, zero-field in-plane reflectivity spectrum from the previous chapter to obtain the reflectivity in field which is shown in panels (b) and (e) for the two configurations, respectively. For  $\mathbf{H} \perp a$ , the additional spectral weight due to the peak at low energies pushes the reflectivity very close to 1 for high fields. The observed changes with a peak magnitude of 3.7% at 34 T can therefore be considered significantly large for such a metallic system. The detailed field dependence of the peak is shown in panel (c) for the SC and HF datasets, where error bars are determined from the noise level of the spectra. The magnitude increases up to 22 T and then saturates, following the same behaviour as the magnetisation for in-plane fields [81]. The field dependence of the peak for  $\mathbf{H} \parallel a$  is shown in panel (f), resulting in the same trend and similar magnitude up to 16 T.

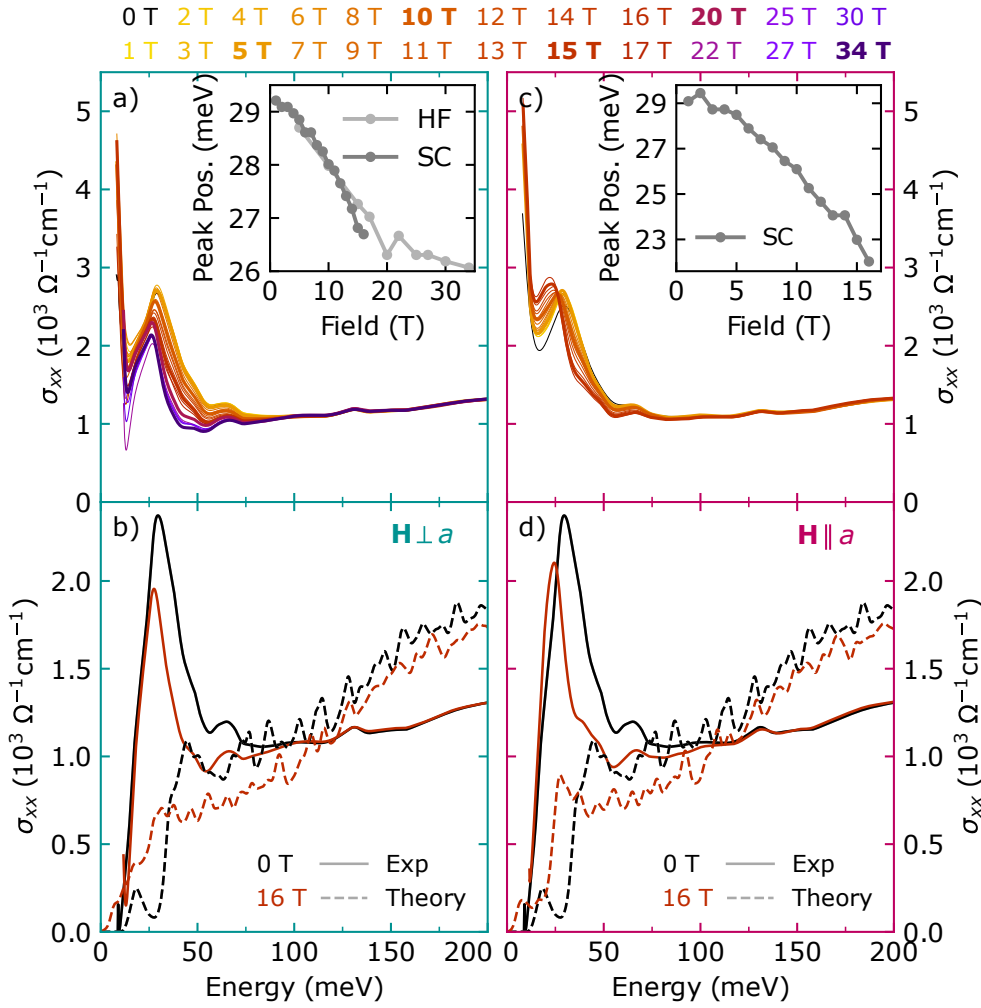
**Magneto-reflectance follows magnetisation**

Based on these reflectivity spectra, we can now analyse the underlying changes in the electronic structure by evaluating the optical conductivity.

## 4.2 Optical Conductivity in Magnetic Field

We perform the Kramers-Kronig analysis on the magneto-reflectivity spectra with the same dc extrapolation as the zero-field spectrum, since only a small negative magneto-resistance of 2% was observed up to 15 T [65]. The resulting optical conductivity at the various fields is shown in Fig. 4.3(a) and (c) for  $\mathbf{H} \perp a$  and  $\mathbf{H} \parallel a$ , respectively. The most prominent features are the metallic Drude contribution at energies below 15 meV and a peak around 29 meV which shifts to smaller energies at higher fields for both configurations. The detailed field evolutions of this feature for the two field directions are shown in the respective insets. Again, the peak shift follows the same trend as the magnetisation with saturation above 22 T observed for  $\mathbf{H} \perp a$ . As was shown in Chapter 3, this peak is caused by transitions between bands of the nodal line, excited with almost full circular polarisation. In panels (b) and (d), the spectra at 0 T and 16 T with subtracted Drude contribution are compared directly, together with *ab initio* calculated spectra for the ground state and the two magnetic configurations. The theory spectra reproduce the experimental features on a broad energy scale (compare Fig. 3.3(a)). The shift of the nodal line resonance is captured well as the onset of optical weight appears at lower energies for both directions of the in-plane fields, though the peak in the theory spectra is not as pronounced as in the experiment. The difference may be caused by electronic correlations [71], or the magnitude of the matrix elements for these transitions may be underestimated by the theory. Comparing the calculated optical conductivity for different in-plane orientations of the magnetic field, they appear very similar at high energies but

**Nodal line resonance reacts to magnetic field**

**Figure 4.3**

Magnetic field dependence of the conductivity spectra in  $\text{Co}_3\text{Sn}_2\text{S}_2$  up to 0.2 eV. (a,c) Optical conductivity in magnetic field for  $\mathbf{H} \perp a$  and  $\mathbf{H} \parallel a$ , respectively. The insets show the respective evolution of the peak, located around 29 meV at 0 T. (b,d) Comparison with calculated conductivity spectra (adapted from [80]).

show small differences around the resonance at 30 meV. While for  $\mathbf{M} \parallel a$  the slope of the peak is shifted parallel compared to the  $\mathbf{M} \parallel c$  spectrum, the peak for  $\mathbf{M} \perp a$  is broadened and the slope reduced. In addition the redshift is larger for  $\mathbf{M} \parallel a$ . Both observations are consistent with the experimental data for the two directions.

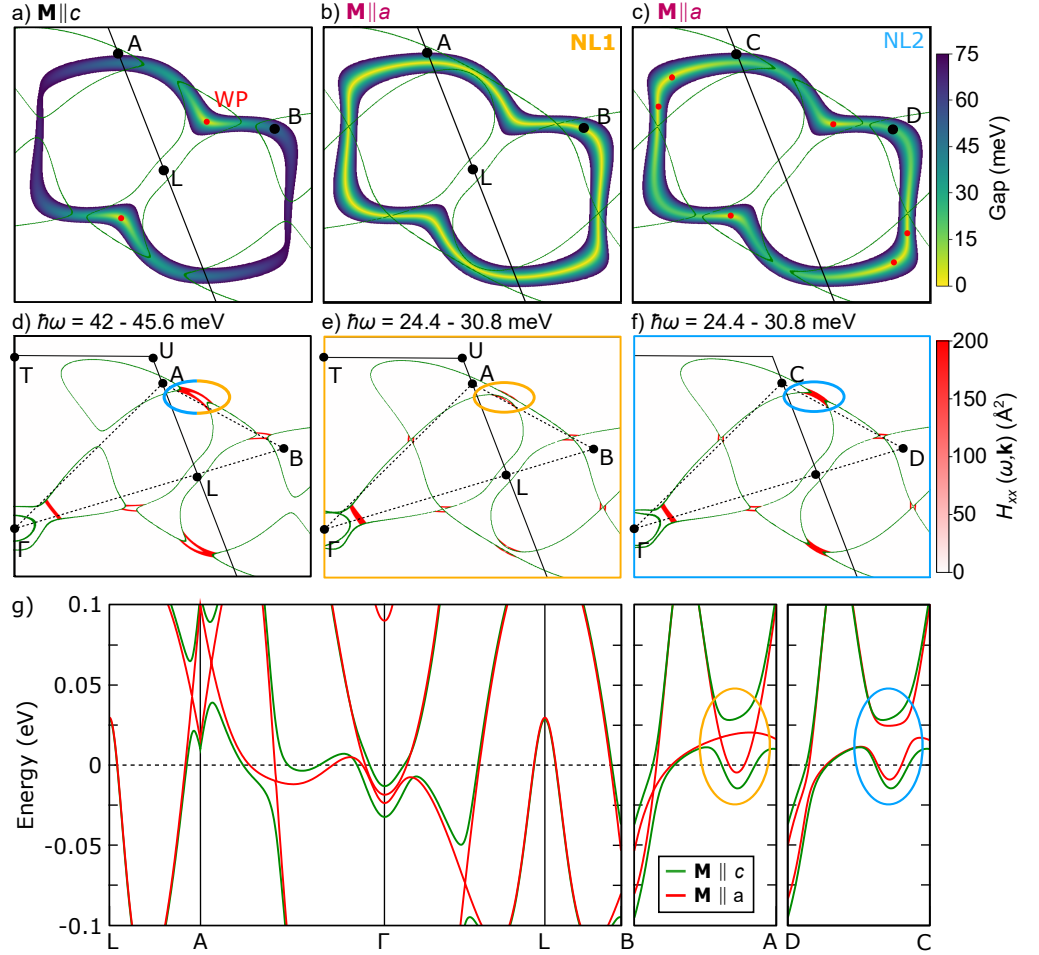
### 4.3 Evolution of the Nodal Line

In order to evaluate the origin of the peak shift, we directly investigate the band structures for the different magnetic configurations. Here, I only show the  $\mathbf{M} \parallel a$  case with the protected nodal line, while the analysis for  $\mathbf{M} \perp a$  may be found in Appendix A.2 which yields very similar conclusions. Details about the calculations performed by Ming-Chun Jiang at the group of Ryotaro Arita may be found in Ref. 80.

We start by comparing the differences between the nodal lines. Fig. 4.4(a–c) plots the gap size of the loops for  $\mathbf{M} \parallel c$  and of NL1 and NL2 for  $\mathbf{M} \parallel a$ , respectively. The position of Weyl points is shown in red and the Fermi surface with dark green lines. For both in-plane loops in panels (b) and (c), the average gap size is smaller than for out-of-plane magnetisation in panel (a), not only for the gapless NL1. This is clearly reflected in the band structure plot in panel (g),

**Figure 4.4**

Evolution of the nodal loop upon reorienting the magnetisation to  $\mathbf{M} \parallel a$ . (a–c) Gap of the nodal lines for out-of-plane and NL1 and NL2 in-plane loops, respectively. For (a), the average gap is larger than for (b) and (c). Points C and D are equivalent to A and B but lie on the BZ planes that contain NL2 instead of NL1. (d–f) Optical weight  $H_{xx}$  at the peak energies (42.0 – 45.6 meV in (d), 24.4 – 30.8 meV in (e) and (f)) distributed on the high-symmetry planes of the BZ containing the nodal loops from (a–c). We obtain qualitatively similar distributions despite the different energy ranges. (g) Band structure along the triangles in the right column. The high-symmetry points are shown above and in Fig. 4.1(c). The gapless nature of NL1 is evident, while also for NL2 the SOC gap along the nodal line is clearly smaller than for out-of-plane magnetisation (adapted from [80]).



where we show the bands for  $\mathbf{M} \parallel c$  and  $\mathbf{M} \parallel a$  in green and red, respectively. Along A–B and C–D, the gapless nature of NL1 is evident, while also the gap for NL2 is smaller than for out-of-plane magnetisation.

In order to compare the generation of optical weight by these features, we again calculate the distribution of spectral weight in the BZ, similar to Chapter 3. For this, we reuse Eq. 3.3, but now for the diagonal conductivity distribution  $\text{Re } H_{xx}(\omega, \mathbf{k})$ , which is shown for the different nodal lines in Fig. 4.4(d–f). Due to the smaller gap, the nodal lines contribute in a different energy range to the optical conductivity. Therefore, in panel (d), we plot the spectral weight distribution for out-of-plane magnetisation at photon energies between 42.0 – 45.6 meV, whereas for in-plane field in (e) and (f) we show the optical weight at 24.4 – 30.8 meV. Qualitatively, all plots show similar features with a small hotspot along  $\Gamma$ –L and several hotspots where the nodal line lies around the Fermi energy, e.g. on the A–B and C–D lines. This comparison shows that the onset of optical weight of the optical conductivity for in- and out-of-plane magnetisation is generated by the same band structure regions, but at different photon energies, explaining

### Shrink of SOC gap

the shift of the peak as the moments cant into the  $ab$  plane. Interestingly, if we infer the position of the Weyl nodes from panels (a–c), we do not find any optical weight associated with transitions around these points. As was shown previously for  $\mathbf{M} \parallel c$ , the Weyl nodes are located around 60 meV above the Fermi level and therefore cannot contribute to the optical response at such low energies [62]. For in-plane field, while the gap changes significantly, the energy of the crossing

point with respect to  $E_F$  does not change upon reorientation of the magnetisation. Therefore, by comparing the momentum position of the Weyl nodes with the colour scale in Fig. 3.1(c), the same argument also accounts for the absence of optical weight from the Weyl points for  $\mathbf{M} \parallel a$ . Similarly, the Weyl points away from high-symmetry directions do not contribute to this low-energy response.

Let us now discuss the possible origin of the nodal line reconstruction. Since the gap is initially produced by SOC, a shrinking gap indicates a reduction of the SOC strength. Among other quantities that have the same nature are the orbital magnetic moment [82] or the magneto-crystalline anisotropy [83, 84]. We can explain the origin of such anisotropy if we directly compare the relative SOC strength for the different SOC matrix elements in the  $p$ - or the  $d$ -orbital basis [84, 85]. In the same spin channel, the SOC matrix elements  $\langle d_{yz} | \mathcal{H}_{\text{SOC}} | d_{xy, x^2-y^2} \rangle$  and  $\langle d_{yz} | \mathcal{H}_{\text{SOC}} | d_{z^2} \rangle$  prefer the in-plane anisotropy, while  $\langle d_{xy} | \mathcal{H}_{\text{SOC}} | d_{x^2-y^2} \rangle$  and  $\langle d_{yz} | \mathcal{H}_{\text{SOC}} | d_{xz} \rangle$  favour the out-of-plane direction. Interestingly, their magnitude ratio is  $\langle d_{yz} | \mathcal{H}_{\text{SOC}} | d_{xy, x^2-y^2} \rangle^2 : \langle d_{yz} | \mathcal{H}_{\text{SOC}} | d_{z^2} \rangle^2 : \langle d_{xy} | \mathcal{H}_{\text{SOC}} | d_{x^2-y^2} \rangle^2 : \langle d_{yz} | \mathcal{H}_{\text{SOC}} | d_{xz} \rangle^2 = 1 : 3 : 4 : 1$  [85]. As the nodal lines consist mainly of Co  $d_{xy, x^2-y^2}$  orbitals with small contributions from the Co  $d_{xz, yz}$  orbitals [80], we note that in the above relation, the SOC matrix element of  $\langle d_{xy} | \mathcal{H}_{\text{SOC}} | d_{x^2-y^2} \rangle$  dominates. This indicates that out-of-plane magnetism is energetically preferred, as the magnetic ground state of  $\text{Co}_3\text{Sn}_2\text{S}_2$  verifies, and that the SOC strength is reduced when in-plane field is applied. This is directly confirmed as we observe a gap shrink for in-plane magnetisation in  $\text{Co}_3\text{Sn}_2\text{S}_2$ .

These results are summarised in the next thesis point.

### Thesis Point 2

On  $\text{Co}_3\text{Sn}_2\text{S}_2$ , I have measured magneto-reflectance in Voigt configuration for two perpendicular field directions in the kagome plane, which result in the generation of a large number of Weyl points and a protected nodal loop. The resulting spectra show a spectral weight redistribution at low energies that follows the same trend as the in-plane magnetisation. I calculated the optical conductivity in field, which associates this redistribution to a peak caused by the nodal line resonance. Comparison to *ab initio* calculated spectra shows that the peak shift is associated with a narrowing of the SOC induced gap of the nodal line, while the large number of emergent Weyl nodes does not contribute significantly to the low-energy response [80].

Due to the simple band structure of  $\text{Co}_3\text{Sn}_2\text{S}_2$  around the Fermi level, the assignment of spectroscopic features to the nodal lines could be performed relatively straightforward. In order to see whether magneto-optical spectroscopy can also pinpoint signatures of topological bands in more complicated systems, we will investigate another kagome magnet next.



## Signatures of a Helical Nodal Line in the Anomalous Hall Effect of $\text{Fe}_3\text{Sn}_2$

The second example of kagome magnets studied in this thesis is  $\text{Fe}_3\text{Sn}_2$ , where Fe kagome bilayers are stacked in an *ABC*-fashion, with Sn honeycomb spacer sheets. The crystal structure, again with space-group  $R\bar{3}m$ , is shown in Fig. 5.1(a) [86]. With  $T_C = 657\text{ K}$ , this compound becomes a soft ferromagnet with the moments aligned along the *c* axis at high temperatures, but they gradually rotate into the *ab* plane when the temperature is lowered [86–88]. Whether the bulk magnetic order is completely collinear is still debated, while in thin *ab* plane lamellae branched domains and skyrmionic bubbles were observed as a result of competing easy-axis and shape anisotropy due to magnetic dipole-dipole interaction. [87–90]. Fig. 5.1(e) shows the dendrite domains on the surface of a bulk crystal, emerging from the same competition [90]. Due to the bulk nature of the investigated crystals, we nevertheless again consider no topological Hall effect.

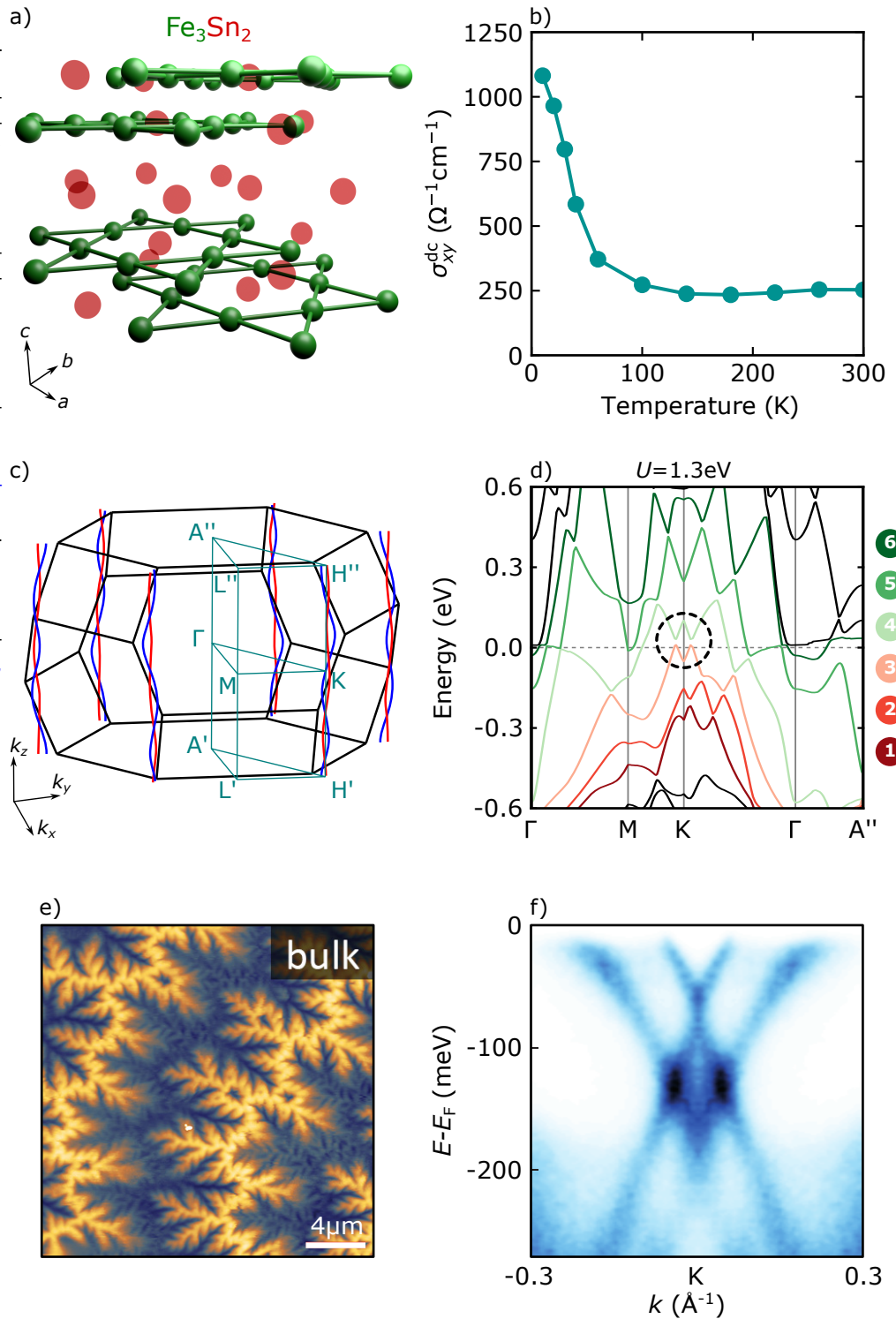
In  $\text{Fe}_3\text{Sn}_2$ , very diverse electronic topology emerges. ARPES and optical studies observe massive (gapped) Dirac Fermions close to the Fermi energy, as shown in Fig. 5.1(f) [20, 91, 92]. Additionally, STM results indicate the presence of flat bands, emerging from localised states on the kagome hexagon which may also leave fingerprints in the optical conductivity [92, 93]. Further studies suggest the presence of a large number of Weyl points in the bulk of the BZ, whose distribution depends on the orientation of the magnetisation [94]. Lastly, following the construction from Sec. 1.2.4, a DFT investigation finds a pair of helical nodal lines around each K point due to the bilayer *ABC*-stack [26]. This feature is illustrated in Fig. 5.1(c) while the bands forming these nodal lines are highlighted in panel (d). When SOC and magnetic order are both taken into account, one of the nodal lines gaps completely, while the other leaves a pair of Weyl nodes behind, whose position is sensitive to the direction of the magnetic moment [26].

**Variety of topological features including helical nodal lines**

Due to this variety of topological features, the origin of the large AHE detected in this material stayed unclear [20, 95]. The corresponding magneto-transport data is shown in Fig. 5.1(b) with an AHE of similar magnitude as in  $\text{Co}_3\text{Sn}_2\text{S}_2$  at low temperatures [96]. Interestingly, scaling relations suggest that a big portion of the AHE has extrinsic origin due impurity scattering [20, 95]. One reason may be that, compared to  $\text{Co}_3\text{Sn}_2\text{S}_2$ , the band structure of  $\text{Fe}_3\text{Sn}_2$  is more complicated and a large number of bands cross the Fermi energy, as Fig. 5.1(d) indicates, each potentially influencing the AHE. Therefore, separating the individual contributions of the different bands is a remarkable experimental challenge. So next, we will see whether magneto-optical spectroscopy, again supported by *ab initio* calculations, is able to quantify the ratios of extrinsic and intrinsic contributions and identify the origin of the intrinsic AHE also for such a complicated band structure.

**Figure 5.1**

Topological properties of Fe<sub>3</sub>Sn<sub>2</sub>. (a) Crystal structure highlighting the stacked Fe kagome bilayer sequence. (b) Giant AHE with values up to 1100  $\Omega^{-1}\text{cm}^{-1}$  at low temperatures. (c) Helical nodal lines around the K points of the hexagonal BZ. (d) Band structure along selected high-symmetry directions with SOC, magnetic moment along the  $c$  axis and  $U = 1.3\text{eV}$ . The band crossings of the helical nodal lines are highlighted with the dashed circle (adapted from [26, 96]). (e) Dendrite domains in bulk Fe<sub>3</sub>Sn<sub>2</sub> observed by MFM (Reproduced Fig. 1(a) from M. Althaler *et al.*, *Physical Review Research* **3**, 043191 (2021) under Creative Commons license). (f) ARPES dispersion around the K point showing massive Dirac Fermions (Reproduced Fig. 3(c) with permission from Springer Nature, L. Ye *et al.*, *Nature* **555**, 638–642 (2018)).



## 5.1 Reflectivity and MOKE Spectra

In  $\text{Fe}_3\text{Sn}_2$ , the conductivity tensor has the same form as in  $\text{Co}_3\text{Sn}_2\text{S}_2$  due to the same space-group when the magnetisation points along the  $c$  axis. Unfortunately, the available sample platelets did not provide large enough  $ac$  surfaces, hence only  $\sigma_{xx}$  and  $\sigma_{xy}$  could be determined ( $z \parallel c$ ). The reflectivity spectra were obtained by collaborators (Jihaan Ebad-Allah at the group of Christine Kuntscher) using a Hyperion IR-microscope with a 15x Cassegrain objective, attached to a Bruker Vertex 80v. The spectra were measured in the MIR-FIR range from room temperature down to 10 K. A silver film, evaporated on half of the single crystal was used as a reference. Each low frequency spectrum was merged to the NIR-VIS spectrum measured at room temperature, resulting in spectra ranging from 0.01 – 2.5 eV. The optical conductivity was calculated by using Kramers-Kronig analysis, where the low-energy side was extrapolated by using a Drude-Lorentz fitting, while above 2.5 eV the reflectivity spectra were extrapolated using x-ray atomic scattering functions [97]. The single crystal used to obtain the MOKE spectra has an as grown  $ab$  surface with a diameter of  $\approx 3$  mm and was measured in  $\pm 0.3$  T applied along the  $c$  axis in the previously described spectrometers.

The resulting spectra for temperatures between 10 – 300 K are shown in Fig. 5.2. Again, we observe metallic reflectivity approaching unity towards zero energy as demonstrated in panel (a). Around 0.2 eV, a local minimum forms upon lowering the temperature. Above 1 eV, there is no significant temperature dependence and the reflectivity decreases towards higher energies overall agreeing with a former publication [92]. The Kerr rotation and ellipticity are shown in panels (b) and (c), respectively. Because of the high  $T_C$ , we detect finite Kerr angles already at room temperature with a magnitude in the order of  $0.1^\circ$ . Both angles are positive and approach 0 for  $\omega \rightarrow 0$ . At 0.125 eV, the rotation shows a steep decrease where the ellipticity even peaks for low temperatures. This is the energy where the plasma edge in the reflectivity is observed and correspondingly the permittivity vanishes. Since  $\varepsilon_{xx}$  appears in the denominator of Eq. 1.49, these features can be assigned to the plasma edge enhancement of MOKE [98]. For higher energies, the rotation is negative with a minimum at 0.5 eV. At this energy, the ellipticity shows a sign change. For higher energies, both angles are rather featureless. The two components can be nicely mapped onto each other by Kramers-Kronig transformation confirming the properness of the measurement.

**Plasma edge enhanced MOKE**

Interestingly, the magnitude of the Kerr angles decreases for lower temperatures in the featureless high-energy regime. Judging from the band structure shown in Fig. 5.1(d), we expect that many interband transitions contribute to the response, averaging out the temperature dependence of individual excitations. Therefore, the temperature dependence in this range may be related to the out-of-plane magnetisation, which decreases for lower temperatures as the magnetic moments cant into the plane, although the magnetic moment per Fe site is slightly increasing [87, 95].

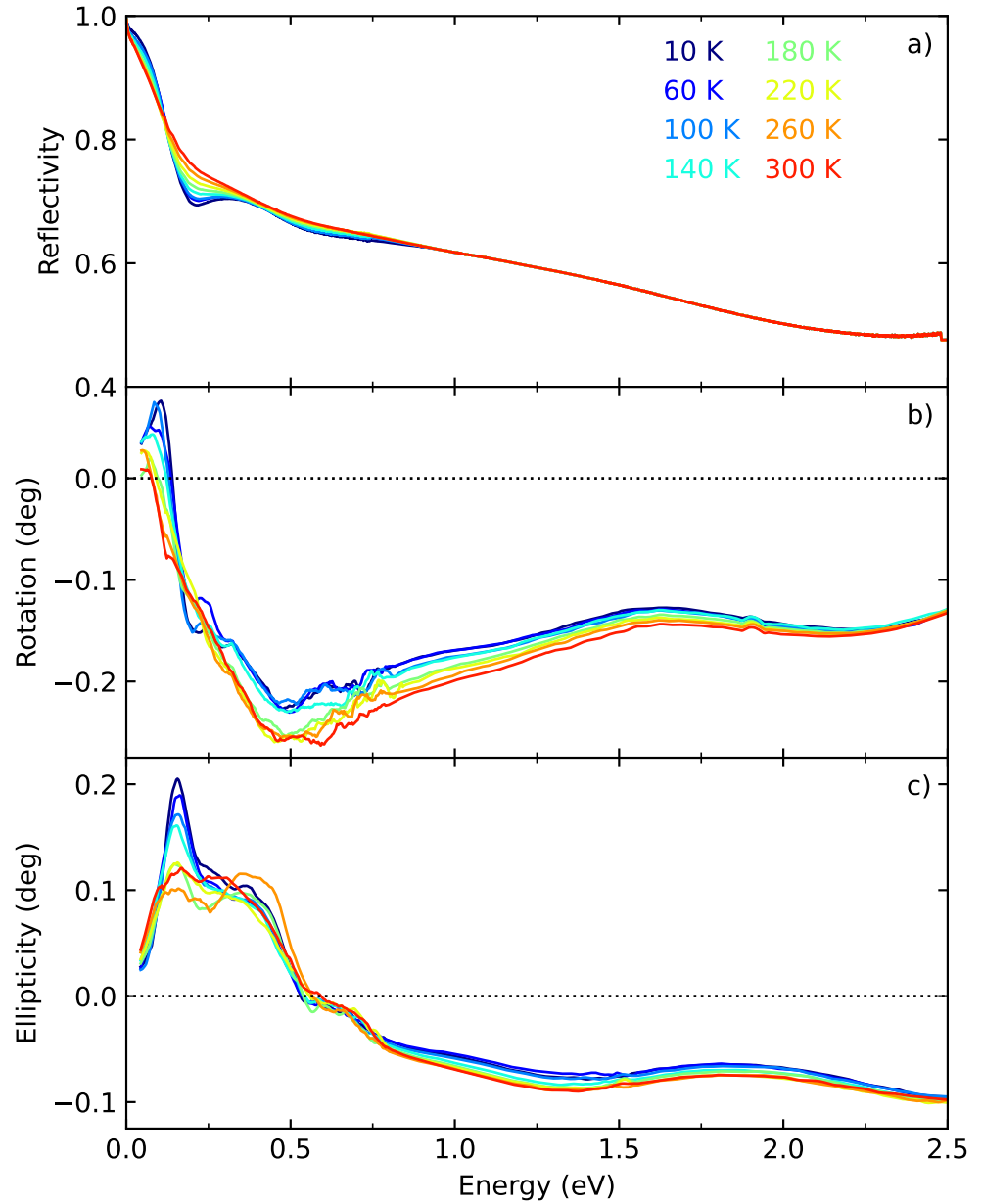
Based on these reflectivity and MOKE spectra, next we can calculate the conductivity tensor for the kagome plane.

## 5.2 Optical Conductivity Spectra

The derived conductivity tensor elements for each temperature are presented in colour in Fig. 5.3. The real part of  $\sigma_{xx}$  in panel (a) shows a Drude peak at zero energy which becomes sharper at low temperatures. Around 0.25 eV, we observe

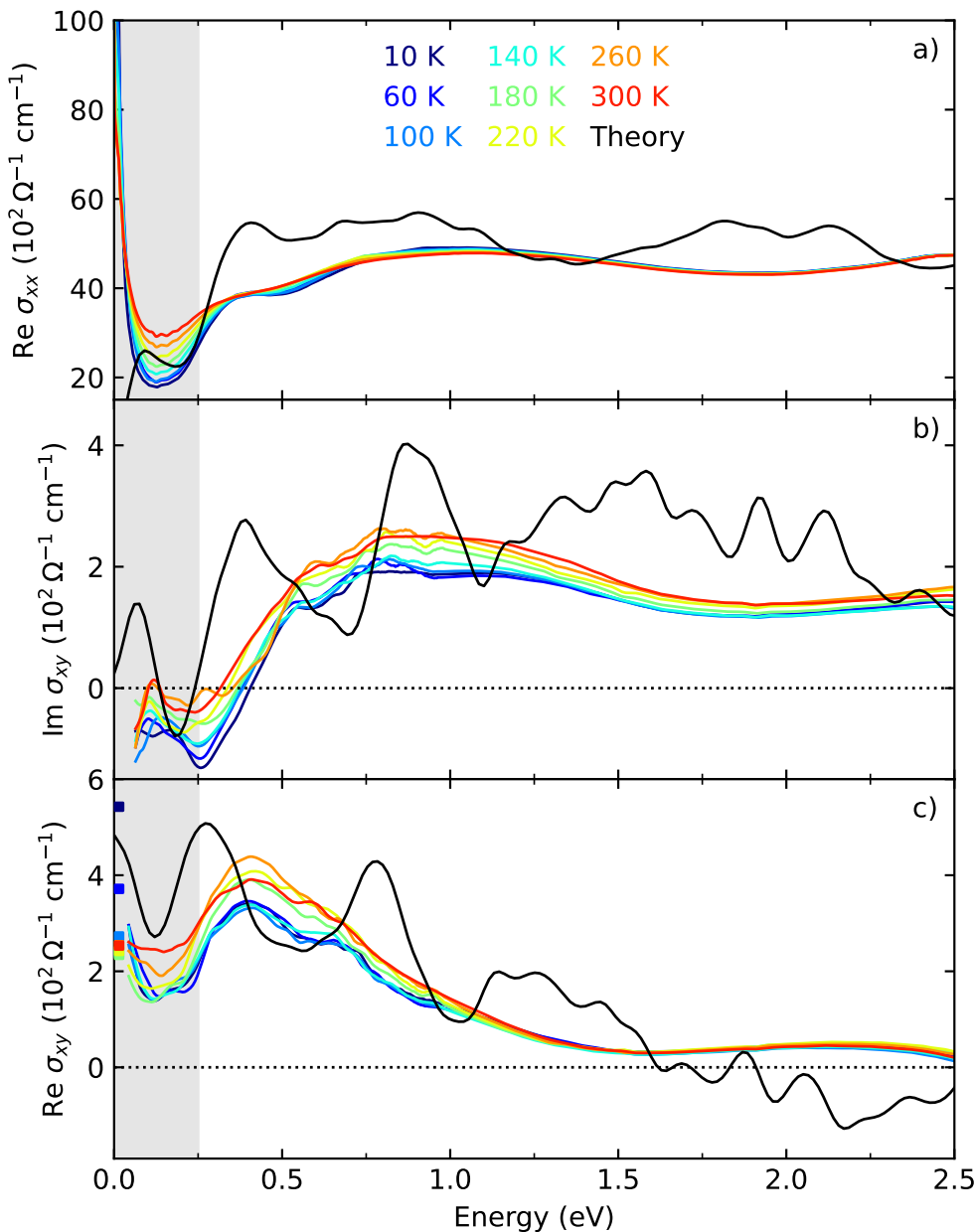
**Figure 5.2**

Reflectivities and Kerr parameters for  $\text{Fe}_3\text{Sn}_2$  from room temperature down to 10 K. (a) Reflectivity in the  $ab$  plane. Kerr rotation (b) and ellipticity (c) spectra (adapted from [96]).



a step edge followed by a broad maximum centred around 0.9 eV. Both features are clearly separated from the free carrier response. These spectra agree with those published in Ref. 92, despite of a small peak around 40 meV which appears to be masked by the Drude term in the present spectra.

In the imaginary part of the Hall conductivity in Fig. 5.3(b), we observe three main features: A small peak around 0.125 eV, a minimum at 0.35 eV followed by a broad maximum again around 0.9 eV, similar to  $\sigma_{xx}$ . Due to the Kramers–Kronig relationship, the derivative shape of these features appears in  $\text{Re } \sigma_{xy}$ . The broad hump leads to an increase of the Hall conductivity for lower energies, leading to a maximum of  $450 \Omega^{-1}\text{cm}^{-1}$  at 0.45 eV. Below this energy, the minimum depletes the Hall conductivity while the transitions from the small peak lead to an upturn towards the cutoff. This upturn matches the spectra well to the dc values shown as coloured squares, especially for high temperatures. With a Drude width of 31 meV, we expect that extrinsic scattering starts to contribute just below the

**Figure 5.3**

Conductivity tensor elements for  $\text{Fe}_3\text{Sn}_2$ . Comparison of the spectra measured between 10 and 300 K (coloured lines) and the theoretical DFT spectra (black lines). (a,b) and (c) respectively show the real part of the diagonal,  $\text{Re } \sigma_{xx}$ , as well as, the imaginary and real part of the off-diagonal conductivity spectra,  $\text{Im } \sigma_{xy}$  and  $\text{Re } \sigma_{xy}$ . The static AHE values are plotted for comparison as coloured squares at zero energy (adapted from [96]).

spectral cutoff of the optical study. This shows, that the Berry curvature accounts for a Hall conductivity of about  $250 \Omega^{-1} \text{cm}^{-1}$  and extrinsic contributions do not play a major role for the AHE at high temperatures. By contrast, for temperatures below 100 K, the spectra have to turn up significantly to extrapolate to the static values, implying a large extrinsic contribution, making up more than 75% of the total AHE at 10 K.

To clarify which of the topological features lead to the intrinsic AHE, Nico Unglert in the group of Liviu Chioncel performed DFT calculations to reproduce the measured spectra (details for the calculations may be found in Ref. 96). They find that introducing a Hubbard correction  $U = 1.3 \text{ eV}$  to the Fe ( $3d$ ) orbitals to simulate local Coulomb interactions significantly improves the agreement with the experiment, while another publication uses the same value to explain ARPES results [99]. The resulting band structure for selected high-symmetry points is shown in Fig. 5.1(d), while the spectra are coplotted with the experiment in

**Dominantly intrinsic  
AHE above 100 K**

Fig. 5.3. Beside the free carrier response, the theory reproduces the low-energy features of  $\text{Re } \sigma_{xx}$  in panel (a). The small peak at 0.1 eV is masked by the Drude peak in the experiment, but the step edge at 0.25 eV is captured as well as the broad maximum, although slightly shifted in energy. In  $\text{Im } \sigma_{xy}$ , the sequence of the peak, minimum and step edge is resolved by the theory, although it is shifted to lower energies with respect to the experiment. At higher energies, the theory spectrum shows two peaks instead of one broad feature with a shoulder in the experiment. Since *ab initio* calculations do not include the lifetime of excited states, features can appear sharper than in the experiment, possibly explaining the observed behaviour. Similarly, the low-energy side of  $\text{Re } \sigma_{xy}$  is well captured in the theory, whereas features at higher energies are again sharper. If the lifetime is assumed to be independent of the photon energy, further smoothing of the theoretical spectrum could improve the agreement, but would certainly mask the low-energy behaviour this study is focused on. Importantly, the dc extrapolation of the theory predicts a similar AHE as the experiment. Under the assumption that low-energy side is reproduced by the theory, we can now investigate which band structure features are responsible for the spectral shape.

### 5.3 Band and Momentum Decomposition

Fig. 5.4 focuses on the energy range below 0.25 eV for the dissipative components of the diagonal and off-diagonal conductivity spectra,  $\text{Re } \sigma_{xx}$  and  $\text{Im } \sigma_{xy}$ , respectively. For this energy window, we find that three transitions between bands  $2 \rightarrow 3$ ,  $3 \rightarrow 4$  and  $4 \rightarrow 6$  yield the dominant spectral weight (compare Fig. 5.1(d) for band labels). The individual contributions are shown by the blue spectra in panels (a) and (f), their sum as a dashed grey line and the total spectrum from Fig. 5.3 is shown in black.

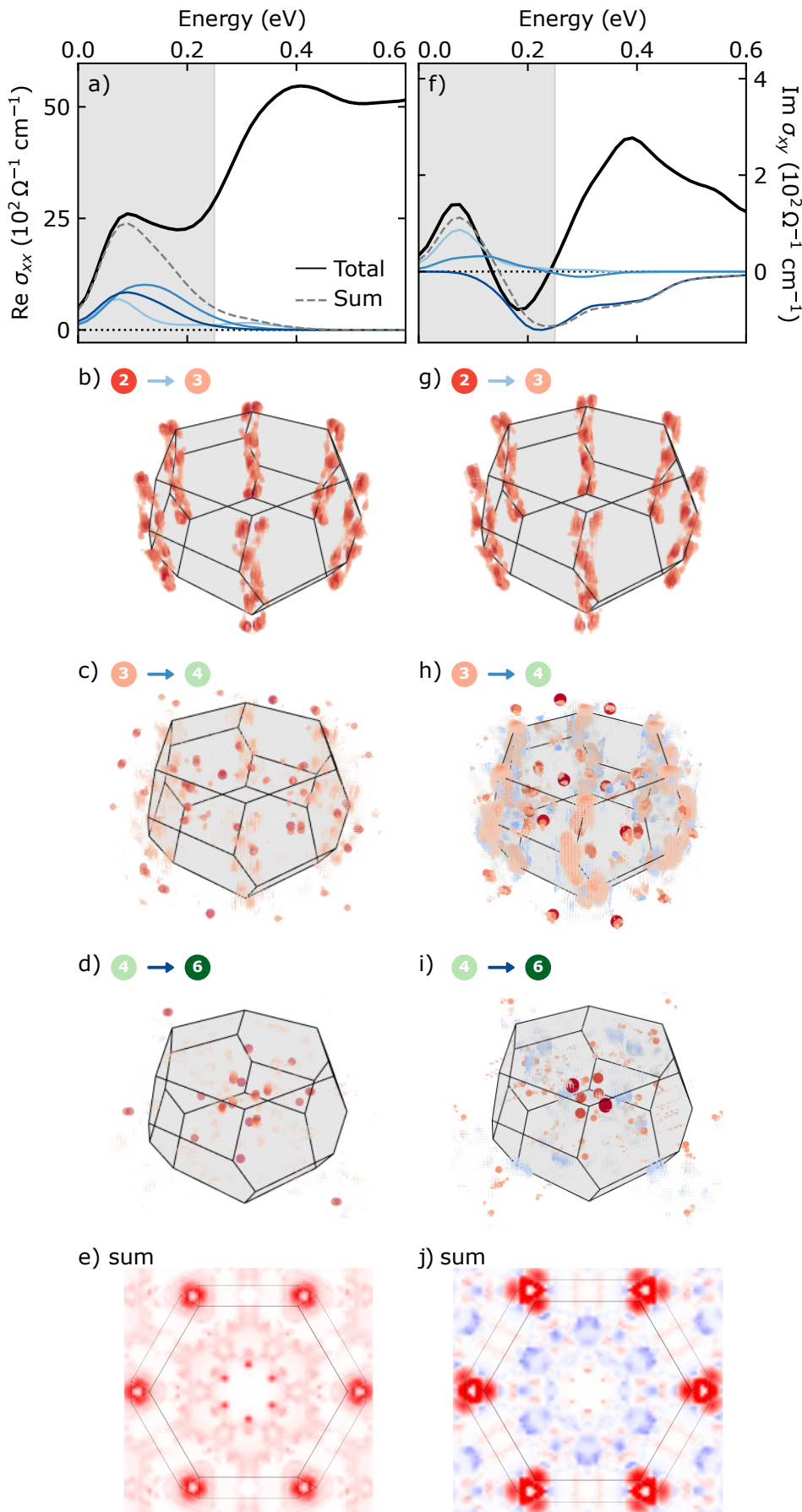
To check in which part of the BZ the responsible transitions occur, we take a similar approach as in the previous chapter and calculate the optical weight distribution. Due to the extensive number of bands at the Fermi level, this time we do not perform the summation over the band indices in order to resolve the interband transitions. Starting from Eq. 3.3, we combine the terms in the summation and the prefactors to define the spectral density  $\rho_{\alpha\beta}^{n \rightarrow n'}(\omega, \mathbf{k})$  as

$$\begin{aligned} \sigma_{\alpha\beta}(\omega) &= \frac{ie^2}{\hbar V} \sum_{\mathbf{k}, n, n'} (f_{n'}(\mathbf{k}) - f_n(\mathbf{k})) \cdot \left( \frac{\epsilon_{n'}(\mathbf{k}) - \epsilon_n(\mathbf{k})}{\epsilon_{n'}(\mathbf{k}) - \epsilon_n(\mathbf{k}) - \hbar\omega} \right) \mathcal{A}_{nn'}^\alpha(\mathbf{k}) \mathcal{A}_{nn'}^\beta(\mathbf{k}) = \\ &= \sum_{\mathbf{k}, n, n'} \rho_{\alpha\beta}^{n \rightarrow n'}(\omega, \mathbf{k}). \end{aligned} \quad (5.1)$$

The corresponding weight to  $\text{Re } \sigma_{xx}$  for each of the three transitions and their sum is shown in Fig. 5.4(b–e) and for  $\text{Im } \sigma_{xy}$  in (g–j), respectively. Red/blue spectral density denotes positive/negative optical weight. The colour labels refer to the band structure as shown in Fig. 5.1(d), whereas the blue arrows denote the respective spectrum in (a) and (f).

For the transition from bands  $2 \rightarrow 3$ , the optical weight in the BZ of both  $\sigma_{xx}$  and  $\sigma_{xy}$  traces out a double helix along the  $H' - K - H''$  line (panels b & g), strongly resembling the helical nodal lines introduced in in Fig. 5.1(c). The hotspots from bands  $3 \rightarrow 4$  and  $4 \rightarrow 6$  appear less localised but distributed at various positions around the BZ as shown in panels (c,d) & (h,i) for  $\sigma_{xx}$  and  $\sigma_{xy}$ , respectively. Their location may be estimated in the top view of the BZ in panels (e) and (j). These

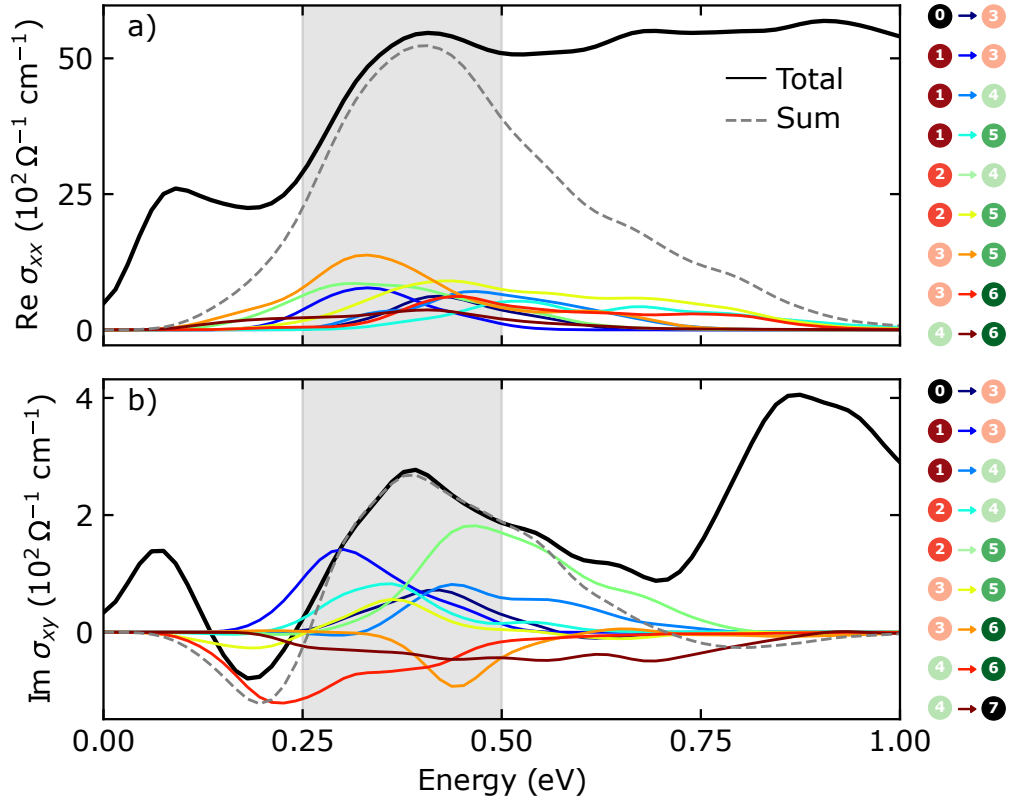
**Hotspots form helical volumes**

**Figure 5.4**

Low-energy band and momentum decomposition for conductivity spectra in  $\text{Fe}_3\text{Sn}_2$ . Three transitions ( $2 \rightarrow 3$ ,  $3 \rightarrow 4$  and  $4 \rightarrow 6$ ) yield most of the spectral weight for the energy window of  $0 - 0.25$  eV (shaded in grey). (a,f) The total spectra calculated for  $\text{Re } \sigma_{xx}$  &  $\text{Im } \sigma_{xy}$  are shown in black, while the individual transitions are plotted in blue shades and their sum in dashed grey. (b-d)  $\mathbf{k}$ -resolved spectral weight distributions  $\rho_{\alpha\beta}^{n \rightarrow n'}$  ( $0 \text{ eV} < \hbar\omega < 0.25 \text{ eV}$ ,  $\mathbf{k}$ ) of the three transitions and their sum (e) for  $\text{Re } \sigma_{xx}$ . The numerical labels refer to the bands as in Fig. 5.1(d) while the arrows have the same colour as the corresponding spectra in panel (a). Panels (g-j) depict the same information for  $\text{Im } \sigma_{xy}$ , where  $\mathbf{k}$ -regions with red/blue colour represent positive/negative weights. As seen in panels (b) and (g), the lowest energy transitions are located around the  $\text{H}'\text{-K-H}''$  line as “helical volumes” and dominate the off-diagonal response around  $0.1$  eV (adapted from [96]).

**Figure 5.5**

Spectral decomposition of the step edge between 0.25 – 0.5 eV for  $\text{Re } \sigma_{xx}$  (a) and  $\text{Im } \sigma_{xy}$  (b). The individual transitions are shown in colour, with the corresponding band indices shown in the respective legend. Bands 0 and 7 not indicated in Fig. 5.1(d) lie just below band 1 and above band 6, respectively. The sum is plotted in dashed grey and the total spectrum in black. For both conductivity components, many interband transitions contribute to the total optical weight (adapted from [96]).



hotspots may be related to Weyl nodes or weakly gapped crossings arising in the bulk of the BZ, although pinpointing the structures is difficult due to the plethora of points and their locations away from high-symmetry directions [26, 94]. Note that some transitions also contribute with negative optical weight to  $\text{Im } \sigma_{xy}$ , producing the minimum at 0.2 eV. In both tensor elements, the summed optical weight along the double helices produces large hotspots at the K and K' points, but in total they contribute only partially to the 0.1 eV peak in the diagonal conductivity. By contrast they dominate the lowest peak of the Hall conductivity highlighting the strength of MOKE spectroscopy in investigating quantities derived from the Berry curvature.

As a significant contribution to the AHE is also produced at higher energies, we also check the energy interval from 0.25 – 0.5 eV related to the step edge, where the resulting band decomposition is shown in Fig. 5.5. In a former publication of  $\sigma_{xx}$ , this feature was associated to transitions between the bands of two Dirac points, with the step edge emerging once Pauli blocking is overcome [92]. Our decomposition contradicts this picture as shown in panel (a). As many bands lie in the vicinity of the Fermi energy, a variety of transitions is possible with no band pair yielding a dominant contribution. A similar situation is encountered for  $\text{Im } \sigma_{xy}$  in panel (b), where many transitions with positive and negative weights combined are necessary to produce the total response. If any, the contributions from bands 1 → 3 and 2 → 5 may be the largest here, but due to the number of transitions we did not perform a momentum decomposition.

At even higher energies, we expect more and more transitions to contribute, therefore, we conclude that not a single topological feature produces the intrinsic AHE in  $\text{Fe}_3\text{Sn}_2$ , but a whole variety of transitions need to be taken into account, yielding the next thesis point.

### Thesis Point 3

In the kagome bilayer ferromagnet  $\text{Fe}_3\text{Sn}_2$ , I measured the broadband magneto-optical Kerr effect spectra between 50 meV–3 eV, which together with reflectivity data allowed me to calculate the conductivity tensor elements for the kagome plane. Again the far-infrared MOKE spectra enabled me to match the dc Hall effect to the optical spectra, revealing that the AHE in  $\text{Fe}_3\text{Sn}_2$  is dominantly intrinsic above 100 K with a magnitude of  $250 \Omega^{-1}\text{cm}^{-1}$ . At lower temperatures, extrinsic scattering plays a major role. Due to the large number of bands close to the Fermi energy, the intrinsic AHE is produced by a large variety of transitions, but we could identify a distinct contribution from the helical nodal lines at energies below 0.2 eV [96].

This is a clearly distinct outcome compared to the conclusion of Chapter 3, so it is worth to shortly note the differences.

## 5.4 Comparison and Outlook

The studies resulting in the preceding chapters followed the same methodology to investigate the origin of the AHE in two, at first sight, similar kagome magnets. In  $\text{Co}_3\text{Sn}_2\text{S}_2$ , the band structure is relatively simple close to the Fermi energy, with topological features solely lying on a high-symmetry plane. This results in clear spectroscopic signatures of the nodal line in the MOKE and Hall conductivity spectra and a dominantly intrinsic AHE. By contrast, the band structure of  $\text{Fe}_3\text{Sn}_2$  is much more complicated with many bands crossing the Fermi energy and a huge variety of topological features away from high-symmetry directions potentially relevant for the generation of the AHE. Despite these difficulties, the study could quantify the intrinsic contribution and record the fingerprints of the helical nodal line unambiguously in the optical Hall conductivity.

Although these big differences between the two materials, the topological features responsible for the AHE could be identified in both cases, proving magneto-optical spectroscopy a highly efficient tool to investigate the low-energy electronic structure of topological magnets. The key to the success of these studies was the development and implementation of the FIR MOKE setup, which allowed the extension of the MOKE spectra to the FIR range, together with the good agreement with the *ab initio* calculations, allowing the band and momentum decompositions.

In terms of material engineering, the  $\text{Co}_3\text{Sn}_2\text{S}_2$  study suggests a way how to increase the Hall response. The Hall spectral weight hotspots may be enlarged by bringing the crossing points of the nodal line closer to the Fermi energy until eventually the system becomes gapped where the diagonal dc conductivity vanishes. In this respect, monitoring the effects of doping, e. g. by different compositions of  $\text{Co}_3\text{Sn}_{2-x}\text{In}_x\text{S}_2$  or of external stimuli like magnetic fields or pressure by magneto-optical spectroscopy may give hints towards the realisation of such a peculiar phase. As shown in Chapter 4, in-plane fields can actually strongly modify the topology and band structure in this itinerant magnet. Experiments to analyse the effect of Indium doping were initiated together with a master student, while the group of Christine Kuntscher started to investigate the effects of hydrostatic pressure on the optical spectra.

Similarly, due to the spin reorientation, the evolution of topological features depending on the magnitude and direction of an external magnetic field in  $\text{Fe}_3\text{Sn}_2$

may reveal information about the interplay of its complex electronic topology with the magnetic order. In addition, there exists a whole family of compounds with slightly different stoichiometry, e. g.  $\text{Fe}_3\text{Sn}$  or  $\text{FeSn}$ , which differ in the stacking sequence of the kagome layers and the magnetic properties. Investigating the other family members may therefore give insights how topological features can be tuned by different layer stacking. An initial project along this direction was already completed together with the group of Christine Kuntscher [100].

Another interesting direction is to leave the realm of collinear ferromagnets, to which both compounds investigated so far belong. In materials with non-collinear magnetic order, e. g. a skyrmion lattice state, additional contributions to the Hall effect can arise to due scalar spin chirality. These contributions are ascribed to real-space Berry curvature and therefore termed topological Hall effect, which was already observed in itinerant kagome magnets [101]. Performing magneto-optical spectroscopy on such systems can reveal how the electronic structure is influenced by such topological states.

One interesting material which combines itinerant carriers and non-collinear order is the kagome spin-ice candidate  $\text{HoAgGe}$ . In this system, a peculiar evolution of transport properties across metamagnetic transitions was observed. In the following, we will investigate how its electronic structure behaves under these transitions.

## Tracing Band Reconstructions across Metamagnetic Transitions in HoAgGe

In Chapter 4, we have already seen that the band structure in kagome magnets can be sensitive to the magnetic order. In that example, we tuned the ferromagnetic order in  $\text{Co}_3\text{Sn}_2\text{S}_2$  from out-of-plane to in-plane, with the emergent optical response closely following the magnetisation due to the collinear nature of the ground state order. Therefore, the interesting question arises whether for non-collinear magnets, additional field induced metamagnetic orders couple differently to the electronic structure, especially in itinerant systems. Again, the kagome lattice provides a good platform for this kind of study due to its triangular nature, hosting the potential for non-collinearity through frustrated interactions.

Our target material for here is HoAgGe, which crystallises in the hexagonal space-group  $P\bar{6}2m$ , with the Ho atoms forming a distorted kagome lattice in the  $ab$  plane with up-/downward facing triangles rotated by  $15.6^\circ$  in opposite directions as shown in Fig. 6.1(a) [102, 103]. The  $a$  axis is defined as one of the hexagonal axes, with  $b$  denoting the perpendicular in-plane direction and  $c$  the stacking axis. Neutron diffraction results indicate that HoAgGe shows non-collinear antiferromagnetic in-plane ordering at low temperatures. Below  $T_2 = 11.6$  K, a partial magnetic order develops where the magnetic moments for 2/3 of the Ho atoms form vortices on 1/3 of the kagome hexagons [103]. For even lower temperatures, the remaining Ho moments enter the magnetic order at  $T_1 = 7$  K, realising the kagome spin-ice state with 2-in-1-out or 1-in-2-out configuration of moments on each kagome triangle, as shown in Fig. 6.2(b) [103, 104].

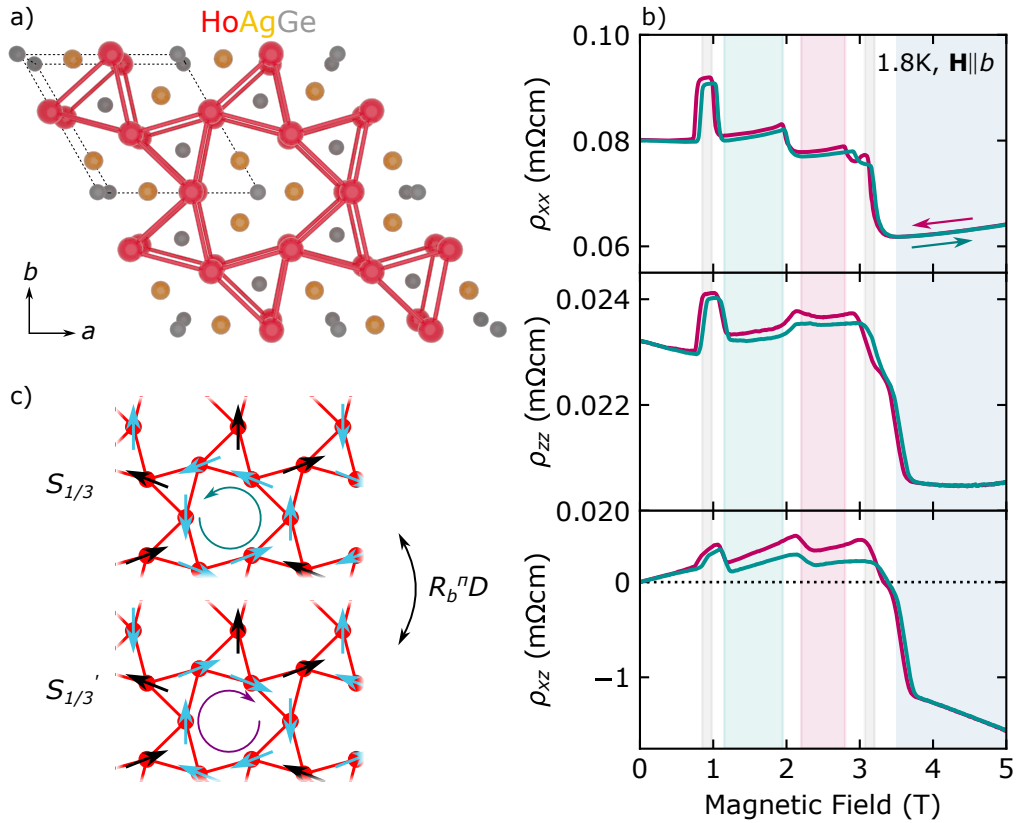
Similar to other members of the RAgGe (R = rare earth) family, HoAgGe undergoes a series of metamagnetic transitions for external magnetic fields applied along the  $a$  or  $b$  axis of the crystal, while it might show a spin-flop transition for field along  $c$  [102, 103]. These metamagnetic states appear as plateaus in the magnetisation curve for field along  $b$  as shown in Fig. 6.2(a). The evolution of the magnetic order is schematically drawn in Fig. 6.2(b–e) with the ground state, the 1/3 and 2/3 magnetisation plateaus and the saturated state, respectively. Due to the strong Ising character of the rare earth moments, for each transition, 1/3 of the total moment flips into the direction of the field, as highlighted by the coloured spins for each transition. This process increases the magnetisation while every state still obeys the kagome ice rule.

### Metamagnetic transitions

Coupled to the diverse magnetic structure, HoAgGe shows rather peculiar electronic transport properties. Fig. 6.1(b) shows the transverse magneto-resistance for  $\mathbf{H} \parallel b$  at 1.8 K. With  $x \parallel a$ ,  $y \parallel b$  and  $z \parallel c$ , both  $\rho_{xx}$  and  $\rho_{zz}$  show strongly non-monotonous evolution between the magnetisation plateaus and unusual hysteretic behaviour [105, 106]. The same is true for the Hall resistivity  $\rho_{xz}$  which doubles in the range of the plateau phases after ramping the field down from saturation [105]. The latter effect was suggested to emerge from the existence

**Figure 6.1**

The peculiar transport properties of HoAgGe. (a) Crystal structure highlighting the tilted kagome triangles. (b) Unusual shape and hysteretic behaviour of the magneto-resistance and AHE correlating with the magnetic phases from Fig. 6.2. (c) The quasi-symmetry  $R_b^\pi D$  relating the two plateau states  $S_{1/3}$  and  $S'_{1/3}$ . The black spins maintain their orientation while the vortices are reversed (adapted from [103, 105]).



of two degenerate magnetic configurations for both of the plateau phases, which supposedly have the same magnetisation, the same band structure, but different Berry curvature due to an unconventional operation linking the two configurations [105]. This is exemplarily shown for the  $1/3$  plateau state  $S_{1/3}$  in Fig. 6.1(c) whose degenerate partner state  $S'_{1/3}$  is related by a  $\pi$  rotation around the  $b$  axis  $R_b^\pi$  and the operation  $D$  which involves a distortion reversal of the kagome triangles from  $+15.6^\circ$  to  $-15.6^\circ$  or vice-versa. The combined operation reverses the orientation of the vortex, while it keeps the other moments (coloured black) fixed. Model calculations show that the band structure for the two states linked by this quasi-symmetry is indeed the same while the Berry curvature differs, which may explain the hysteretic behaviour of the Hall resistivity. But it remains unclear why one of the states should be favoured by the field sweep direction if the magnetisation is the same and why the hysteresis is also present in the diagonal resistivity, for which the identical band structure should not differentiate the response between the two states. In order to answer these questions, magneto-optical spectroscopy is again a suitable tool, as it is able to track the band structure changes between the metamagnetic states for both the diagonal and off-diagonal tensor elements.

Due to the strong field dependence and the hysteretic behaviour of the static Hall conductivity (Fig. 6.1(b)), studying MOKE on this compound can again give profound insight into the topological nature of the Hall effect of HoAgGe. Unfortunately, the magnetic field for the MOKE spectroscopy is limited to 300 mT in the setups described in Sec. 2.3.3, so we can only probe the Kerr response for the magnetic ground state at this stage, although this limitation triggered the development of a high-field MOKE setup at BME. The preliminary low-field data together with an analysis of the anisotropic nature of the MOKE parameters

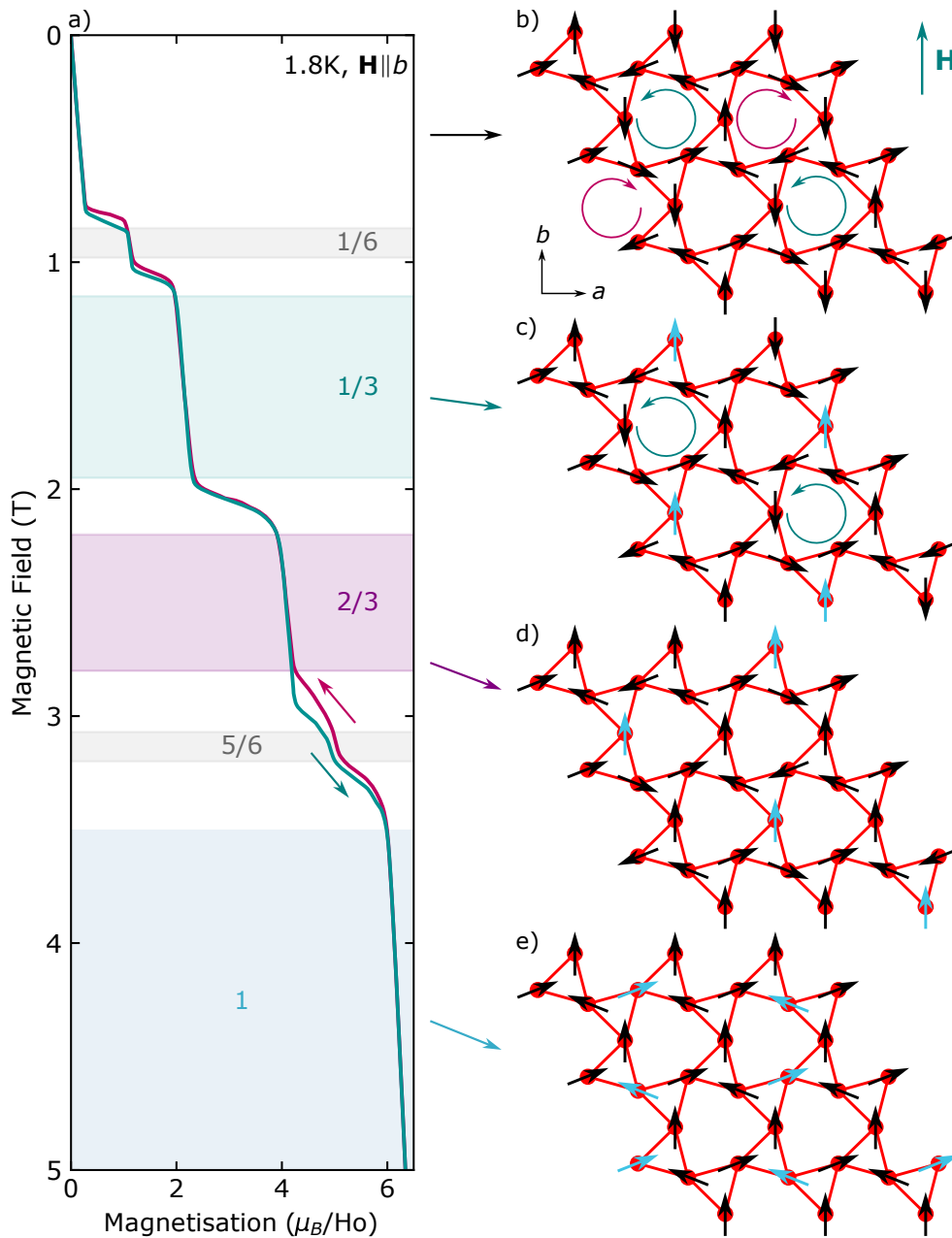


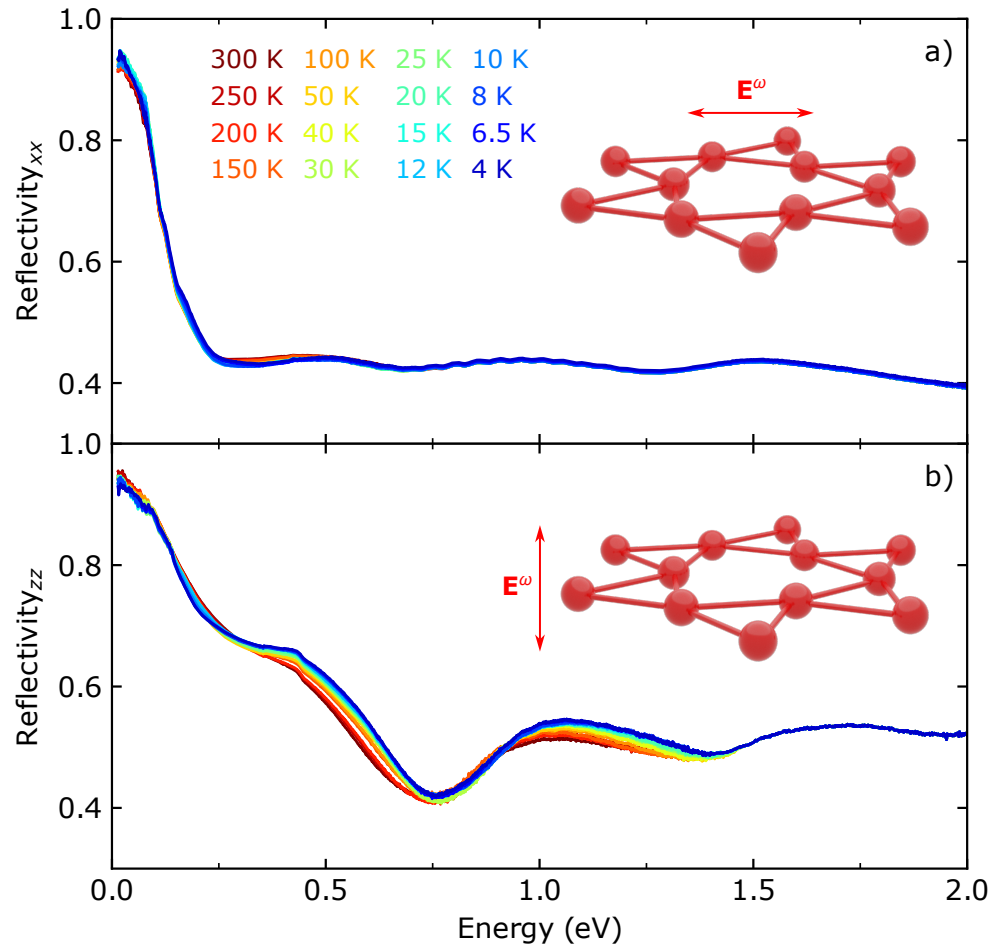
**Figure 6.2** Metamagnetic phases of HoAgGe. (a) Magnetisation at 1.8 K showing distinct plateaus at several fractions of the saturation moment (b–e) Magnetic structures of the ground state, the  $1/3$ ,  $2/3$  plateaus and saturated state, respectively. For each of the phases, the coloured spins flip to increase the magnetic moment parallel to the external field while keeping the kagome ice rule satisfied. Due to the strong Ising nature of the rare earth spins, the saturated state is not fully polarised. (adapted from [103]).

for the symmetry of the non-collinear order in HoAgGe is detailed in Appendix A.3.

Nevertheless, as shown in Fig. 6.1(b), also the diagonal magneto-resistance shows strong changes in magnetic field which correlate with the plateau phases. Since the static resistivity will also influence the Drude component of the low-energy optical response, measuring polarised reflectivity can also reveal the responsible changes in the electronic structure, with the possibility to extend to interband transitions as well. For this type of study, the setups described in Sec. 2.2 provide the required field range. As starting point, we first investigate the polarised zero-field reflectivity.

**Figure 6.3**

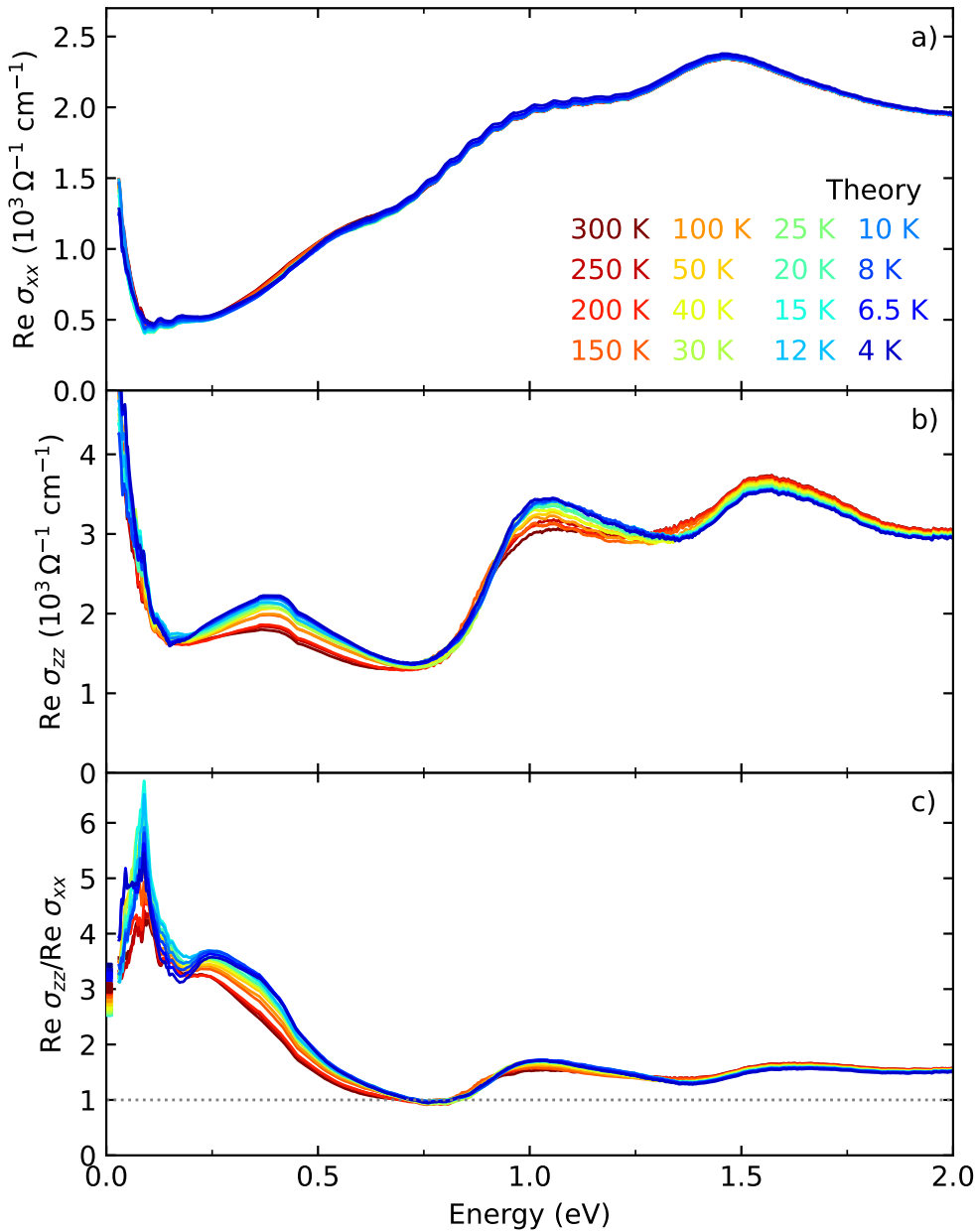
Reflectivity data for HoAgGe. (a) Reflectivity in and (b) perpendicular to the kagome plane. The insets highlight the measurement geometry. The optical anisotropy for in- vs. out-of-plane directions is pronounced (adapted from [107]).



### 6.1 Zero-Field Reflectivity

The reflectivity spectra were obtained by polarised measurements on an *ac* cut crystal with an aperture of 1.4 mm in an energy range from 10 meV to 2.2 eV for temperatures between 4 and 300 K. The sample was mounted on the coldfinger of a Cryovac Helium-flow cryostat and placed in the Bruker Vertex 80v spectrometer for the whole energy range. On the low-energy side, the reflectivity spectra were extrapolated by using the dc conductivity values. For the UV, the spectra were extrapolated with free electron behaviour setting in at  $10^6 \text{ cm}^{-1}$  and an exponent for the high-frequency regime of 1.5. The resulting in- and out-of-plane spectra are shown in Fig. 6.3(a) and (b), respectively. For both polarisations, the metallic character is evident as they approach unity towards low frequencies. For the *ab* plane spectra, we obtain the plasma edge around 120 meV, above which the reflectivity is flat at around 40% with only small temperature dependence. For polarisation along *c*, the spectra above the plasma edge host more features. A distinguished minimum is visible at 0.75 eV which gets more pronounced at lower temperatures. At higher energies, an additional local minimum develops around 1.4 eV above which there is no temperature dependence. Again, these spectra reveal a clear optical anisotropy of the layered crystal structure.

As in the preceding chapters, we now evaluate the optical conductivity based on these reflectivities to discuss the origin of the spectral features.

**Figure 6.4**

Optical conductivity data for HoAgGe. Panels (a,b) show the in- and out-of-plane conductivity,  $\text{Re } \sigma_{xx}$  &  $\text{Re } \sigma_{zz}$  respectively, while panel (c) plots the optical anisotropy  $\text{Re } \sigma_{zz}/\text{Re } \sigma_{xx}$ . The dc values are shown as squares at zero energy for the anisotropy only as the dc conductivity values lie above the shown range (adapted from [107]).

## 6.2 Optical Conductivity and Conductivity Anisotropy

The obtained temperature dependent real parts of the optical conductivity spectra are shown in Fig. 6.4. At energies above 0.2 eV,  $\text{Re } \sigma_{xx}$  increases monotonously up to a broad maximum around 1.5 eV almost independent of temperature. By contrast,  $\text{Re } \sigma_{zz}$  shows a series of three peaks in the same energy range, centred around 0.4, 1 and 1.5 eV, respectively, with the first two being strongly influenced by temperature.

For both  $\sigma_{xx}$  and  $\sigma_{zz}$ , we observe a narrow Drude component in the  $\omega \rightarrow 0$  limit. While these should extrapolate to the static conductivity values, those are not shown in the plots as already at 300 K, they lie above  $4100$  and  $12600 \text{ } \Omega^{-1} \text{ cm}^{-1}$  for the in- and out-of-plane directions, respectively. Therefore, the conductivity across the kagome layers is larger than within the layers, which suggest a strong coupling between the individual kagome planes and a three-dimensional electronic

**Enhanced out-of-plane conductivity** structure. While this is contrasted by the behaviour we obtained for  $\text{Co}_3\text{Sn}_2\text{S}_2$  in Chapter 3, a higher interlayer conductivity is not uncommon for kagome metals as it was reported also e. g. in  $\text{YCr}_6\text{Ge}_6$  [108] and in the  $\text{Fe}_x\text{Sn}_y$  family [100, 109, 110]. For HoAgGe, this conductivity anisotropy persists also at finite frequencies as shown in Fig. 6.4(c), where the conductivity ratio is larger than 1 for most of the covered energy range and approaches the static values towards zero frequency. The sharp peak around 80 meV is caused by a different onset of the Drude peak for the two directions. It appears at slightly higher energies for  $\sigma_{zz}$  which due to the steep increase drastically enhances the anisotropy until  $\sigma_{xx}$  follows. This behaviour may be caused by different scattering rates or effective masses for the in- and out-of-plane directions.

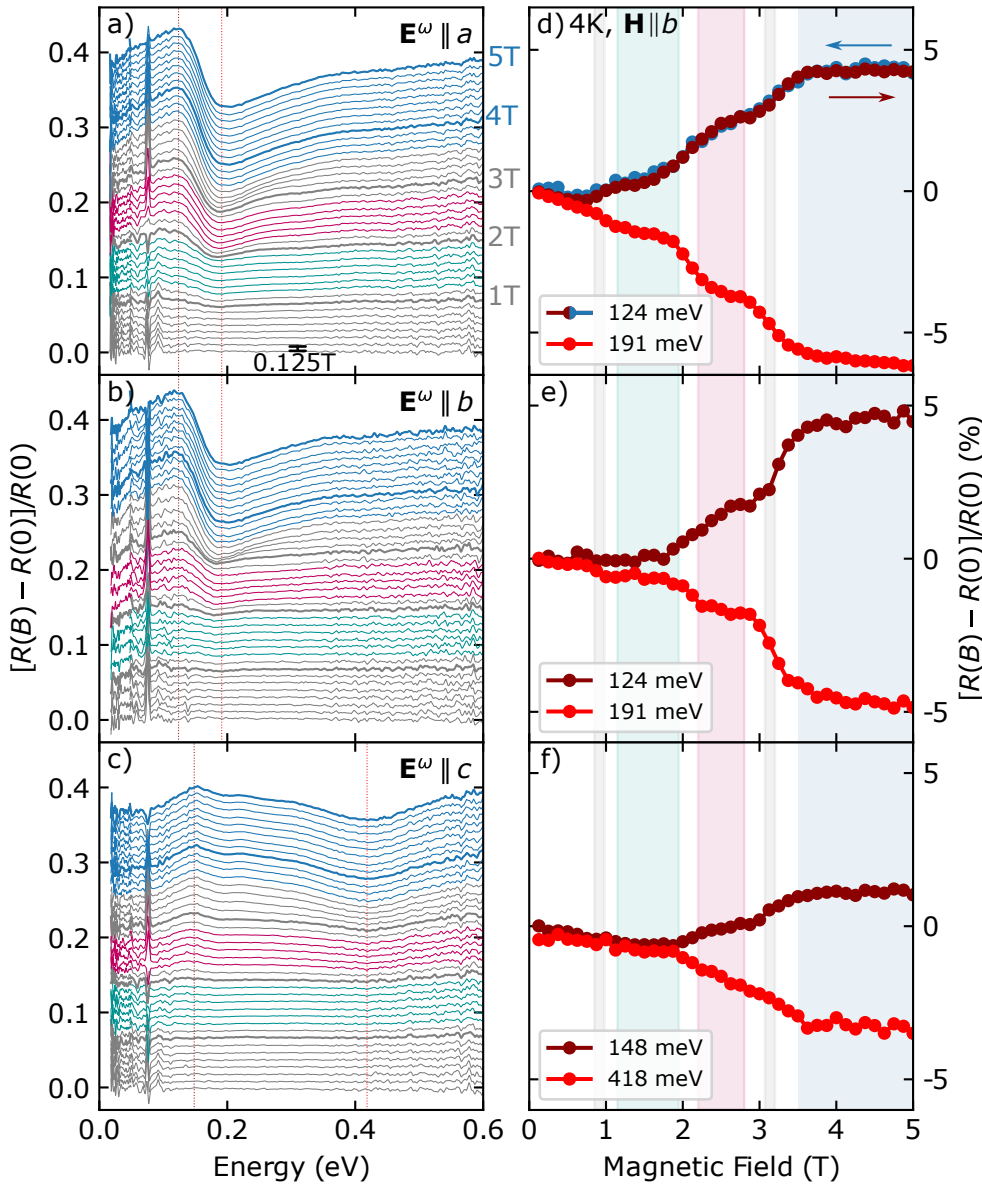
At the time of submission of the thesis, theory collaborators (Luke DeFreitas in the group of Hua Chen) succeeded in calculating the optical conductivity from *ab initio* only for the saturated state. Therefore, we will discuss the possible origin of these features after evaluating the optical conductivity in magnetic field in the following.

### 6.3 Probing Metamagnetic States by Magneto-Reflection

Based on the zero-field reflectivity, we can now investigate the changes in the electronic structure by performing magneto-reflectance experiments. These measurements were performed on *ab* and *bc* cut samples in Voigt configuration in the setup introduced in Sec. 2.2 with field along the *b* axis. The experiments cover the energy range from 20 meV to 0.6 eV and fields up to 5 T, to reach the saturated state of the compound. The obtained polarised magneto-reflectance spectra  $R(B) - R(0)/R(0)$  for  $\mathbf{E}^\omega \parallel a, b$  and *c*, are shown in Fig. 6.5(a-c), respectively.

For the two in-plane directions in panels (a) and (b), we find that the response is very similar despite a higher noise level for  $\mathbf{E}^\omega \parallel b$  due to the beamsplitter in the optical path. At the high- and low-frequency cutoffs, the response approaches 0, meaning no resulting changes in the reflectivity. In between, two spectral features dominate the magneto-reflectance. Around 125 meV a peak develops with increasing magnetic field, which is immediately followed by a minimum around 200 meV. The detailed field dependence of these two features with 125 mT resolution is shown in panels (d) and (e) for the two polarisations, respectively. While the noise level spoils some of the features for  $\mathbf{E}^\omega \parallel b$  in panel (e), the magneto-reflectance for  $\mathbf{E}^\omega \parallel a$  (panel d) shows clear signatures of the metamagnetic phases. Their field ranges are indicated by the background shade (compare Fig. 6.2). While approaching the 1/3 plateau, the magneto-reflectance of both the peak and the dip shows a jump just above 1 T, then stays linear over the field range of the magnetisation plateau. Further jumps occur upon reaching the critical fields for the 2/3 plateau and the saturated state. Upon reaching the latter, the reflectance change saturates around  $\pm 5\%$  for the two features. The magneto-reflectance at these frequencies therefore follows closely the field dependence of the magnetisation and differs strongly from the behaviour of the magneto-resistance. Since the measurement temperature is 4 K, the magnetic transitions are slightly smeared and the 1/6 and 5/6 states do not show any distinct changes. This is in line with the magnetisation data at this temperature [105]. In order to check for hysteretic behaviour, measurements were also taken on sweeping the field down from 5 to 0 T. This is shown by the blue data points

**Magneto-reflectance follows magnetisation**

**Figure 6.5**

Magneto-reflectance data for HoAgGe with  $\mathbf{H} \parallel b$ . (a–c) Magneto-reflectance spectra for the light electric field aligned along each crystallographic axis, respectively. Spectra were taken from 0 – 5 T with 0.125 T steps. Subsequent spectra are offset for clarity. (d–f) Cross-sections at fixed photon energies indicated by the coloured dashed lines in light and dark red in panels (a–c). For in-plane electric field, the reflectance shows distinct plateaus at the metamagnetic phases, following the behaviour of the magnetisation. Due to the spectra being taken at 4 K, no hysteresis was observed for up- and down-sweep measurements (adapted from [107]).

in panel (d), which within the error of the experiments align with the upsweep data, we therefore detect no hysteresis.

One likely explanation is that the hysteresis is already closed at 4 K, as also indicated by magnetisation and transport data [105]. On the other hand, the field dependence of the magnetisation only shows minor hysteresis around the 1/6 and 5/6 states at low temperatures to begin with, as the magnetisation for the degenerate states  $S_{1/3}$  and  $S'_{1/3}$  is the same. The stronger hysteresis of the dc transport data is not observed by the magneto-reflectance experiment. This suggests that at these frequencies, we do not probe the response of the free carriers to the magnetic field, but instead observe a change in the interband excitations that is coupled to the magnetisation. This is corroborated by the optical conductivity, from which we can estimate a width of the Drude peak below 10 meV at low temperatures, below the frequencies of the observed features in the magneto-reflectance.

Before we turn to the consequences of this observation, let us first discuss the remaining polarisation  $\mathbf{E}^\omega \parallel c$ , shown in Fig. 6.5(c). Again, a peak and dip emerge

for increasing field, but the position and shape of these features strongly differ from the other polarisations. The peak now appears at 150 meV while the dip is shifted to 420 meV. In the field evolution shown in panel (f), we can see traces of the metamagnetic states, especially saturation of the magneto–reflectance above 3.5 T in the saturated state, but the overall magnitude is smaller and the clear steps seen in the other polarisations are absent. Again the temperature of 4 K may result in smearing of the steps. Nevertheless, the field dependence still follows the magnetisation better than the magneto–resistance also for this polarisation. This observation encourages to try measurements at even lower photon energies to reach the regime where the magneto–transport data influences the optical response to see the crossover between the two ranges. This may be achieved by polarised terahertz reflection experiments.

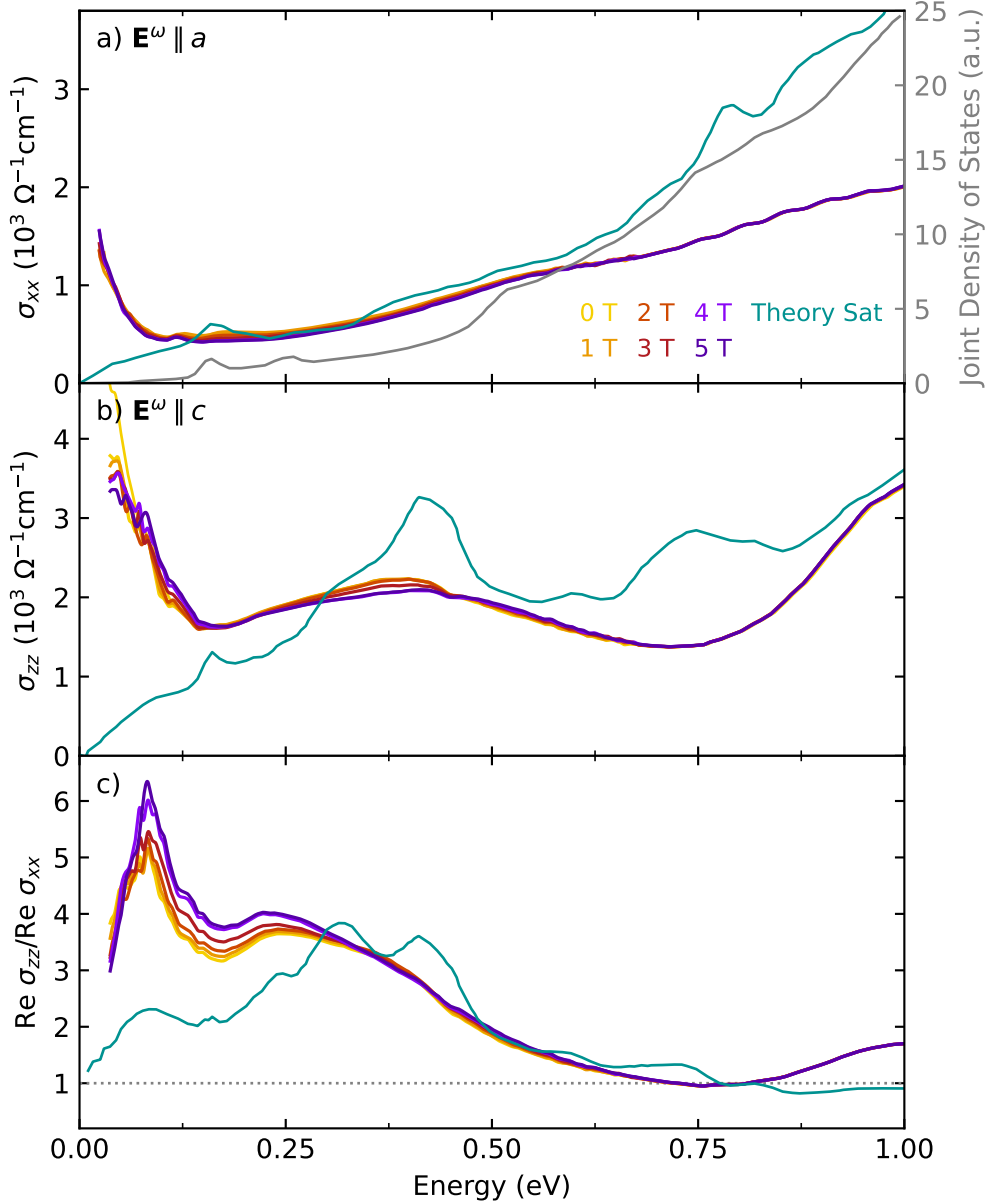
Since the current frequency range of the observed features for all polarisations implies that the band structure responds to the magnetic field, we now investigate the optical conductivity in field for the different polarisations.

#### 6.4 Optical Conductivity between the Plateau Phases

Similar to the study from Chapter 4, we now multiply the magneto–reflectance spectra with the zero–field reflectivity at 4 K and perform a Kramers–Kronig analysis to determine the optical conductivity in a magnetic field. The resulting conductivity spectra for a selection of fields are shown in Fig. 6.6(a,b) for the in– and out–of–plane response, respectively. For both polarisations, the tail of the Drude peak is modified compared to the zero–field response. Although  $\sigma_{xx}$  in high fields increases in agreement with the negative dc magneto–resistance (compare Fig. 6.1(b)), in general, the tail of the Drude peak does not follow the non–monotonous field dependence of the resistivity. At higher energies, the broad minimum in the in–plane conductivity around 0.2 eV is lowered, which also shifts the onset of optical weight of the rising absorption edge to higher energies. For  $\mathbf{E}^\omega \parallel c$ , the peak around 0.4 eV is reduced and shifted to higher energies. These changes are also reflected in the optical anisotropy shown in panel (c), where the broad hump centred around 0.25 meV is modified, which also influences the sharp peak caused by the onset of Drude response.

In all panels, the experimental spectra are compared with the theoretical data for the saturated state shown in green. Beside the Drude component which is not included in the *ab initio* calculation, the spectral features are qualitatively well reproduced in all quantities. For  $\sigma_{xx}$  in panel (a), the theory shows the same monotonous increase as the experiment, although the magnitude is larger towards the high–frequency cutoff. For comparison, the joint density of states is coplotted in grey. This quantity measures the number of transition possibilities from filled to empty states of the band structure for a given (photon) energy, which follows the same monotonous behaviour. This suggests only a small energy dependence of the matrix elements for this polarisation.

We observe a different behaviour for  $\sigma_{zz}$  in panel (b), where the peak at 0.4 eV in both theory and experiment is not reflected in the joint density of states. The preliminary theory hypothesis is that unoccupied  $4f$  states of the Ho atoms hybridise with other states in the same energy range to which the optical transitions occur. If the orbital anisotropy of the  $4f$  states is large enough due to the crystal field splitting, the anisotropy can be transferred to the hybridised states determining the selection rules which lead to the polarisation dependence.

**Figure 6.6**

Magnetic field dependence of the conductivity spectra for HoAgGe up to 1 eV for field applied along the  $b$  axis. (a,b) Optical conductivity in magnetic field for light polarisation  $\mathbf{E}^\omega \parallel a$  and  $\mathbf{E}^\omega \parallel c$ , respectively. The green spectra show the theory for the saturated state, while the grey line corresponds to the joint density of states shown on the second axis (c) Optical anisotropy in magnetic field. (adapted from [107]).

As shown in Fig. 6.6(c), this peak causes the onset of the broad hump in the optical anisotropy. Therefore, in the range above 0.25 eV, the theoretical anisotropy spectra agree very well with the experiment. Below this energy, the dc anisotropy in the Drude response not considered in the theory starts to play a role. Interestingly, also the theoretical spectra show a peak at around 80 meV, so the sharp feature in the experiment at that energy may not be solely related to the Drude anisotropy.

These initial theory results are promising and give the prospect to explain the band origin of the observed spectral features. This requires additional efforts to obtain a band or momentum decomposition of the optical conductivity, as well as the calculation of the optical response for the ground state and the metamagnetic phases. While the first will elucidate the detailed role of the Ho  $4f$  states and possibly contributions of topological bands, the latter will reveal the band reconstructions which cause the steps in the magneto-reflectance. Once these tasks are solved, the combination of theory and experiment will yield a

clear picture of the coupling between the electronic and magnetic properties in this itinerant system.

For now, we summarise the experimental results in the last thesis point.

#### **Thesis Point 4**

On the distorted kagome lattice compound HoAgGe, I have measured the anisotropic MOKE parameters as well as polarised reflectivity and magneto-reflectance for all crystallographic directions with magnetic field applied along the  $b$  axis. Due to the non-collinear magnetic order, we derived a formula for the Kerr parameters with anisotropic diagonal conductivity tensor elements, providing the basis for the analysis of high-field MOKE measurements. The broadband reflectivity measured between 10 meV to 2.2 eV shows strong anisotropy which translates to the optical conductivity along the stacking direction being larger than within the kagome planes. In the magneto-reflectance spectra obtained from 25 meV to 0.5 eV, the relative change of the reflectivity across the metamagnetic phases follows the magnetisation rather than the magneto-resistance for the in-plane response, suggesting a band reconstruction upon the magnetic transitions. The underlying changes of the electronic structure were analysed by evaluating the optical conductivity in magnetic field, which agree with preliminary *ab initio* calculations [107].

## Summary

In this thesis, we investigated the fascinating electronic and optical properties of a variety of kagome lattice based magnets with magneto–optical spectroscopy. While the key achievements of this work are collected by the thesis points in the following Sec. 7.1, I would nevertheless like to give a short summary and put the obtained results into a broader perspective.

During the MOKE studies on  $\text{Co}_3\text{Sn}_2\text{S}_2$  and  $\text{Fe}_3\text{Sn}_2$ , we were able to disentangle the intrinsic and extrinsic contributions to the AHE by using the spectroscopic information of the optical Hall effect provided by broadband MOKE measurements. The different energy ranges of the contributions enabled the clear distinction in the spectra beyond the phenomenological assignment commonly obtained from applying scaling relations on magneto–transport data. Beyond this straightforward separation of contributions, the spectroscopic fingerprints of topological band features especially in the Hall effect spectrum in combination with *ab initio* calculations additionally allowed to pinpoint the specific bands that generate the anomalous response. While in principle also ARPES can reveal the linear band degeneracies, the major advantages of the magneto–optical approach demonstrated here are the high energy resolution and the direct information obtained about the Berry curvature in the optical Hall effect spectrum.

Once we had assigned optical features to specific interband transitions, we could use this information to monitor the manipulation of the topological states by external fields, as demonstrated for  $\text{Co}_3\text{Sn}_2\text{S}_2$ . While a number of theoretical works predicted that in these kinds of systems, the topological properties can be tuned by magnetic field or altering the magnetisation [12, 73–75], actual experimental observations of such effects are rare. Although STM and magneto–transport studies indeed suggest a high sensitivity of the topological band structure to the magnetic state [28, 76–78], they also highlight the difficulty to obtain the desired information about specific bands. One central reason is the incompatibility of ARPES with external magnetic fields, which makes magneto–optical spectroscopy a valuable tool for this type of study. For the presented results on  $\text{Co}_3\text{Sn}_2\text{S}_2$ , this revealed the key role of SOC in the generation of topological phenomena, as we could directly observe its reduction upon the magnetisation reorientation.

These findings demonstrate that while topological band structures are generally considered robust, breaking underlying crystal symmetries with external magnetic fields provides an efficient way to manipulate them even in collinear systems. This handle on the electronic properties of these magnets presents a central prerequisite for applications in spintronics or quantum information technology. This approach opens exciting avenues for investigating materials with more complex magnetic structures and even to study the interplay of real- and momentum-space topological states.

An initial step along this direction was taken with the investigation of the highly frustrated metamagnetic states in  $\text{HoAgGe}$ . While the dc transport properties show a strongly non-monotonous magnetic field dependence, the observed optical

response follows the magnetisation instead. This suggests a reconstruction of the bands and a strong coupling between electronic and magnetic degrees of freedom in this spin–ice candidate.

Overall, despite various experimental challenges, such as small sample sizes, the need to extend spectral ranges, the multiband nature and complex electronic and magnetic structures of the investigated compounds, we were able to successfully perform magneto–optical spectroscopy and gain valuable insights into the topological and magnetic properties in all investigated kagome metals. These studies prove magneto–optics as a versatile and reliable tool to investigate topological bands and hints to the potential for future works to study and control these features beyond the capabilities of other experimental techniques.

## 7.1 Thesis Points and Related Publications

Below, the major achievements of this thesis work are summarised in the form of the thesis points and the corresponding publications.

### Thesis Point 1

On the itinerant kagome ferromagnet  $\text{Co}_3\text{Sn}_2\text{S}_2$ , I have measured the reflectivity spectra with in- and out-of-plane polarisation, and the magneto-optical Kerr effect (MOKE) spectra over a broad energy range from 25 meV to 3 eV. This required the development of a MOKE setup for the far-infrared spectral range, which I successfully realised by fixed polarisers for rotation measurements and a Kramers–Kronig constrained extrapolation of the ellipticity. Due to this extension, I could determine all elements of the conductivity tensor in this material for the specified energy range and capture the peaks caused by interband transitions of the gapped nodal line below 40 meV also in the off-diagonal component. Extrapolating to the dc values confirmed that the AHE in  $\text{Co}_3\text{Sn}_2\text{S}_2$  has dominantly intrinsic nature caused by the nodal line and that Weyl points only give vanishing contributions. By calculating the frequency dependent Hall angle, I could show that these features are caused by an almost fully circularly polarised nodal line resonance, which additionally enhances the optical anisotropy favouring the out-of-plane conductivity.

F. Schilberth *et al.*, “Nodal line resonance generating the large anomalous Hall effect in  $\text{Co}_3\text{Sn}_2\text{S}_2$ ”, [Physical Review B 107, 214441 \(2023\)](#)

### Thesis Point 2

On  $\text{Co}_3\text{Sn}_2\text{S}_2$ , I have measured magneto-reflectance in Voigt configuration for two perpendicular field directions in the kagome plane, which result in the generation of a large number of Weyl points and a protected nodal loop. The resulting spectra show a spectral weight redistribution at low energies that follows the same trend as the in-plane magnetisation. I calculated the optical conductivity in field, which associates this redistribution to a peak caused by the nodal line resonance. Comparison to *ab initio* calculated spectra shows that the peak shift is associated with a narrowing of the SOC induced gap of the nodal line, while the large number of emergent Weyl nodes does not contribute significantly to the low-energy response.

F. Schilberth *et al.*, “Generation of Weyl points and a nodal line by magnetization reorientation in  $\text{Co}_3\text{Sn}_2\text{S}_2$ ”, [arXiv.2408.03575 \(2024\)](#) *submitted*

### Thesis Point 3

In the kagome bilayer ferromagnet  $\text{Fe}_3\text{Sn}_2$ , I measured the broadband magneto-optical Kerr effect spectra between 50 meV–3 eV, which together with reflectivity data allowed me to calculate the conductivity tensor elements for the kagome plane. Again the far-infrared MOKE spectra enabled me to match the dc Hall effect to the optical spectra, revealing that the AHE in  $\text{Fe}_3\text{Sn}_2$  is dominantly intrinsic above 100 K with a magnitude of  $250 \Omega^{-1}\text{cm}^{-1}$ . At lower temperatures, extrinsic scattering plays a major role. Due to the large number of bands close to the Fermi energy, the intrinsic AHE is produced by a large variety of transitions,

but we could identify a distinct contribution from the helical nodal lines at energies below 0.2 eV.

F. Schilberth *et al.*, “Magneto–optical detection of topological contributions to the anomalous Hall effect in a kagome ferromagnet”, *Physical Review B*, **106**, 144404 (2022)

#### Thesis Point 4

On the distorted kagome lattice compound HoAgGe, I have measured the anisotropic MOKE parameters as well as polarised reflectivity and magneto–reflectance for all crystallographic directions with magnetic field applied along the  $b$  axis. Due to the non–collinear magnetic order, we derived a formula for the Kerr parameters with anisotropic diagonal conductivity tensor elements, providing the basis for the analysis of high–field MOKE measurements. The broadband reflectivity measured between 10 meV to 2.2 eV shows strong anisotropy which translates to the optical conductivity along the stacking direction being larger than within the kagome planes. In the magneto–reflectance spectra obtained from 25 meV to 0.5 eV, the relative change of the reflectivity across the metamagnetic phases follows the magnetisation rather than the magneto–resistance for the in–plane response, suggesting a band reconstruction upon the magnetic transitions. The underlying changes of the electronic structure were analysed by evaluating the optical conductivity in magnetic field, which agree with preliminary *ab initio* calculations

F. Schilberth *et al.*, “Tracing Band Reconstructions across Metamagnetic Transitions in HoAgGe”, *in preparation* (2024)

## 7.2 Full List of Publications

- ▷ F. Schilberth *et al.*, “Magneto–optical detection of topological contributions to the anomalous Hall effect in a kagome ferromagnet”, *Physical Review B*, **106**, 144404 (2022)
- ▷ F. Schilberth *et al.*, “Nodal line resonance generating the giant anomalous Hall effect in  $\text{Co}_3\text{Sn}_2\text{S}_2$ ”, *Physical Review B* **107**, 214441 (2023)
- ▷ J. Ebad Allah *et al.*, “Optical anisotropy of the kagome magnet FeSn: Dominant role of excitations between kagome and Sn layers”, *Physical Review B*, **109**, L201106 (2024)
- ▷ K. Vasin *et al.*, “Optical magnetoelectric effect in the polar honeycomb antiferromagnet  $\text{Fe}_2\text{Mo}_3\text{O}_8$ ”, *Physical Review B* **110**, 054401 (2024)
- F. Schilberth *et al.*, “Generation of Weyl points and a nodal line by magnetization reorientation in  $\text{Co}_3\text{Sn}_2\text{S}_2$ ”, *arXiv.2408.03575* (2024) *submitted*
- ▷ F. Schilberth *et al.*, “Tracing Band Reconstructions across Metamagnetic Transitions in HoAgGe”, *in preparation* (2024)
- ▷ V. Bader *et al.*, “Rotational disorder and its impact on the spin–1/2 triangular antiferromagnet  $\text{Na}_2\text{BaCo}(\text{PO}_4)_2$ ”, *in preparation* (2024)

# A

## Appendix

### A.1 Recommissioned and Developed Setups

Summary of the newly commissioned, rebuilt and newly developed setups during the PhD.

#### Commissioned

- ▷ Macro-reflectivity setup for Vertex 80v (UA)
- ▷ Macro-transmission setup for Vertex 80v (UA)
- ▷ Pan-cryo option for Hyperion FTIR-microscope in transmission and reflection (UA)
- ▷ FTIR-microscope based reflectivity setup for magnetic fields up to 5 T for Hyperion (UA)

#### Recommissioned

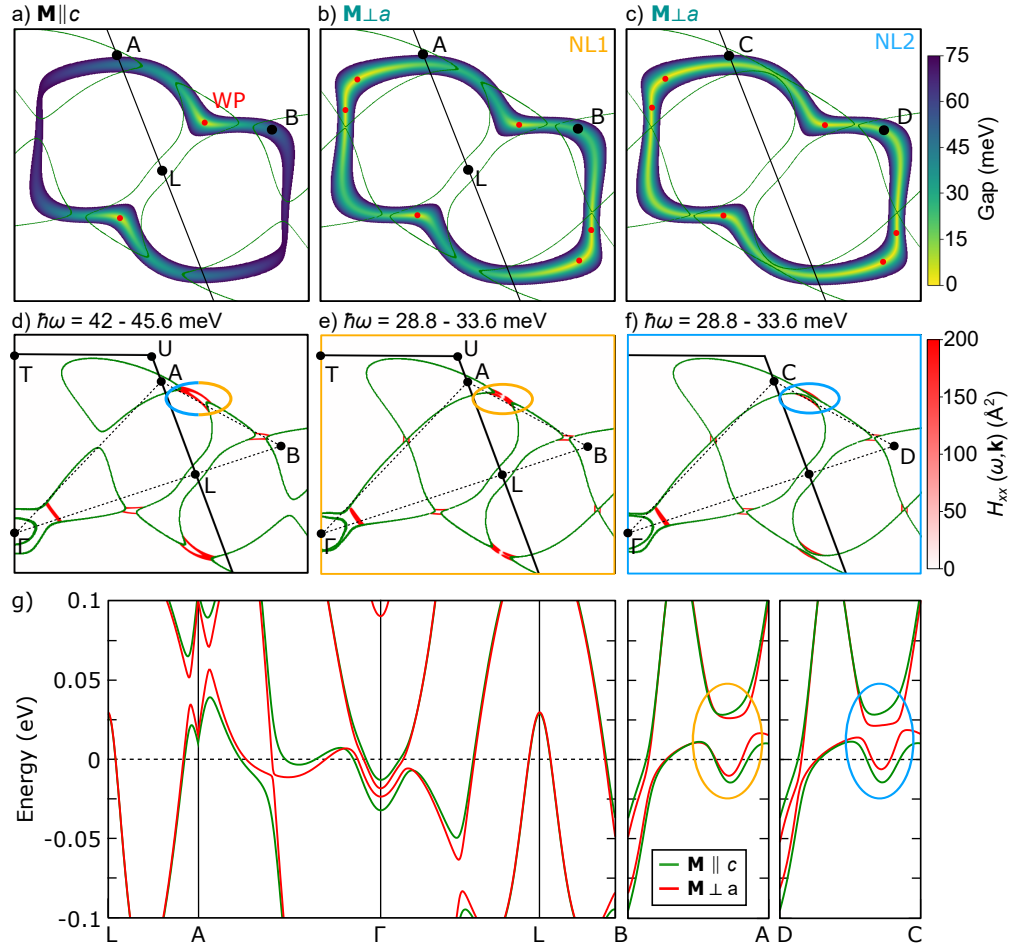
- ▷ grating-based tabletop PEM NIR/VIS MOKE spectrometer (BME)
- ▷ FTIR-based tabletop PEM MIR MOKE spectrometer (BME)
- ▷ Oxford cryostat refurbishment (BME)

#### Developed

- ▷ FTIR-based tabletop fixed polariser FIR MOKE spectrometer (BME)
- ▷ Rotatable polariser mount for high speeds and accurate positioning (BME)
- ▷ NIR Femtosecond laser pump-laser probe MOKE setup (BME)
- ▷ FTIR-based in-system fixed polariser FIR MOKE spectrometer for Vertex 80v (UA)
- ▷ Laser-MOKE setup in magnetic field up to 5 T (UA)
- ▷ Laser-MOKE lab course experiment for bachelor students (UA)
- ▷ Laser or broadband birefringence microscope for detection of antiferromagnetic domains including manipulation with magnetic and electric fields (UA)

**Figure A.1**

Evolution of the nodal loop upon reorienting the magnetisation  $\mathbf{M} \perp a$ . (a–c) Gap of the nodal lines for out-of-plane and NL1 and NL2 in-plane loops, respectively. For (a), the average gap is larger than for (b) and (c). Points C and D are equivalent to A and B but lie on the BZ planes that contain NL2 instead of NL1. (d–f) Optical weight  $H_{xx}$  at the peak energies (42.0 – 45.6 meV in (d), 28.8 – 33.6 meV in (e) and (f)) distributed on the high-symmetry planes of the BZ containing the nodal loops from (a–c). We obtain qualitatively similar distributions despite the different energy ranges. (g) Band structure along the triangles in the right column. The high-symmetry points are shown above and in Fig. 4.1(c). For in-plane magnetisation, the SOC gap along the nodal line is clearly smaller than for out-of-plane (adapted from [80]).



## A.2 Analysis of the SOC Gap in $\text{Co}_3\text{Sn}_2\text{S}_2$ for $\mathbf{M} \perp a$

Fig. A.1(a–c) plots the gap size of the loops for  $\mathbf{M} \parallel c$  and of NL1 and NL2 for  $\mathbf{M} \perp a$ , respectively. The position of Weyl points is shown in red and the Fermi surface with dark green lines. For both in-plane loops in panels (b) and (c), the average gap size is smaller than for out-of-plane magnetisation in panel (a). This is clearly reflected in the band structure plot in panel (g), where we show the bands for  $\mathbf{M} \parallel c$  and  $\mathbf{M} \perp a$  in green and red, respectively. Along A–B and C–D, the main difference between NL1 and NL2 is highlighted, namely a slightly smaller gap for NL2. In order to compare the generation of optical weight by these features, we again calculate the distribution of spectral weight in the BZ by Eq. 3.3 for the diagonal conductivity distribution  $\text{Re } H_{xx}(\omega, \mathbf{k})$ , which is shown for the different nodal lines in Fig. A.1(d–f). Due to the smaller gap, the nodal lines contribute in a different energy range to the optical conductivity. Therefore, in panel (d), we plot the spectral weight distribution for out-of-plane magnetisation at photon energies between 42.0 – 45.6 meV, whereas for in-plane field in (e) and (f) we show the optical weight at 28.8 – 33.6 meV. Qualitatively, all plots show similar features with a small hotspot along  $\Gamma$ –L and several hotspots where the nodal line lies around the Fermi energy, e.g. on the A–B and C–D lines. This comparison shows that the onset of optical weight of the optical conductivity for in- and out-of-plane magnetisation is generated by the same band structure regions, but at different photon energies, explaining the shift of the peak as the moments cant into the  $ab$  plane.

### A.3 Low-Field MOKE Measurements on HoAgGe

Due to the strong field dependence and the hysteretic behaviour of the static Hall conductivity (Fig. 6.1(b)), studying MOKE on this compound can give profound insight into the topological nature of the Hall effect of HoAgGe. Because of the exotic nature of the magnetic order in HoAgGe, we need to check which elements of the dielectric tensor are allowed under the experimental conditions for the MOKE spectroscopy. Unfortunately, the magnetic field for the MOKE spectroscopy is limited to 300 mT in the setups described in Sec. 2.3.3, so we can only probe the Kerr response for the magnetic ground state.

#### A.3.1 *ab* cut with $\mathbf{H} \parallel \mathbf{c}$

The magnetic space-group of HoAgGe below the first metamagnetic transition at 11.6 K is  $-6'_z m_{xz} 2'_x$ , with  $'$  indicating time-reversal operations [103]. If we additionally include a magnetic field along the  $c$  axis, some of these symmetries are broken, resulting in the space-group  $3_z 2'_x$ . Due to Neumann's principle, the dielectric tensor must fulfil  $\hat{\epsilon} = R\hat{\epsilon}R^{-1}$  for any symmetry element  $R$ , consequently

$$\hat{\epsilon} = \begin{pmatrix} \epsilon_{xx}^S & \epsilon_{xy}^A & 0 \\ -\epsilon_{xy}^A & \epsilon_{xx}^S & 0 \\ 0 & 0 & \epsilon_{zz}^S \end{pmatrix}, \quad (\text{A.1})$$

where the diagonal elements have to be symmetric under time-reversal (S) while the off-diagonal elements are antisymmetric (A) [41]. The derivation is detailed in Appendix A.3.4. Therefore, for light propagation along the  $c$  axis, we obtain the same expression for the MOKE parameters as in Sec. 1.3.2.

The MOKE spectra for this configuration were obtained on a polished *ab* cut crystal with a diameter of 1.4 mm. The resulting spectra are shown in Fig. A.2(a,b) for low temperatures. Compared to the studies shown in the previous chapter, the angles are almost two orders of magnitude smaller and we cannot identify distinct spectral features. Therefore, the shown data represents the noise level of the spectrometer and we cannot resolve the actual response of HoAgGe. Hence only the MIR spectra were recorded. Although MOKE is in principle allowed for this geometry as shown above, the out-of-plane magnetisation is very small in 300 mT showing the limits of the angular resolution.

#### A.3.2 *ac* cut with $\mathbf{H} \parallel \mathbf{b}$

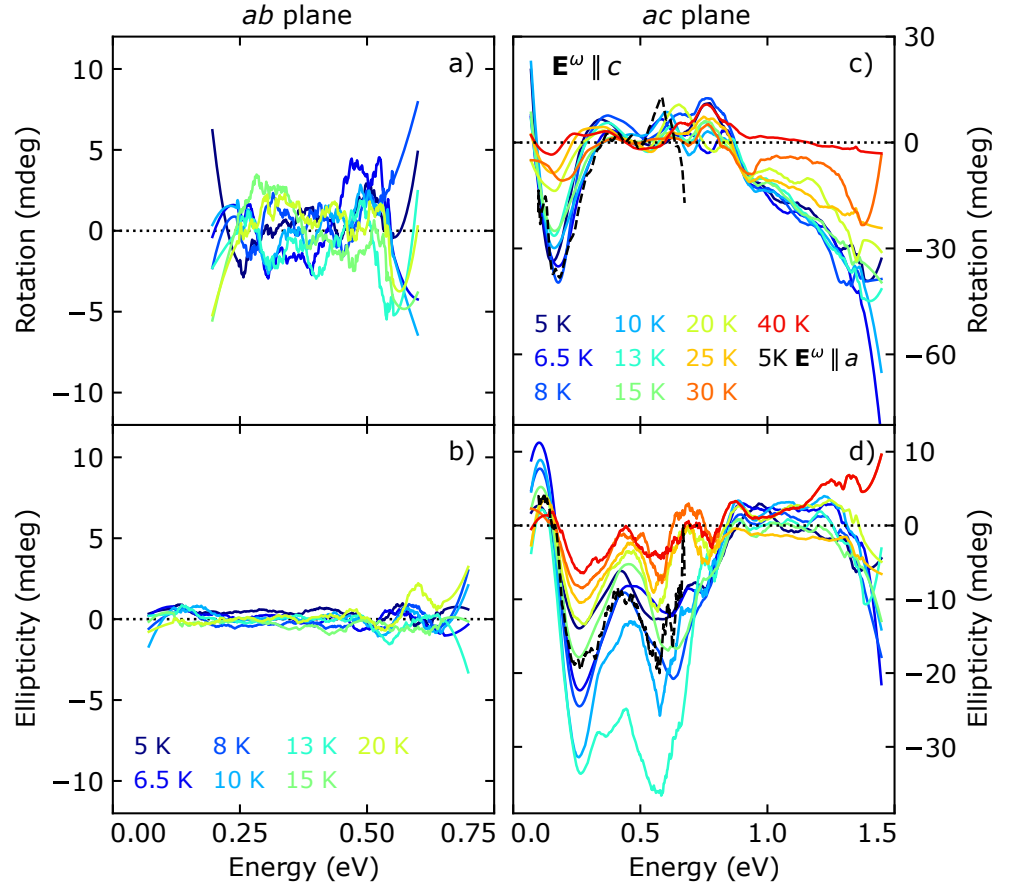
Here, we apply a magnetic field along the  $b$  axis of the crystal. For this configuration, all kinds of magnetic order present in HoAgGe have the same magnetic space-group of  $m'_{xy} m_{xz} 2'_x$  [103]. Applying a magnetic field along the  $b$  axis of the crystal thus does not lead to any new constraints. This yields a dielectric tensor of the form

$$\hat{\epsilon} = \begin{pmatrix} \epsilon_{xx}^S & 0 & \epsilon_{xz}^A \\ 0 & \epsilon_{yy}^S & 0 \\ -\epsilon_{xz}^A & 0 & \epsilon_{zz}^S \end{pmatrix}. \quad (\text{A.2})$$

Therefore, when light is propagating along the  $b$  axis of the crystal, the effective dielectric tensor has anisotropic diagonal elements (details in Appendix A.3.5). Hence we cannot use Eq. 1.50 to calculate the optical Hall conductivity and need to derive a different formula which will be detailed in the following.

**Figure A.2**

Ground state MOKE spectra of HoAgGe obtained at 300 mT. (a,b) MIR *ab* plane Rotation and Ellipticity spectra of HoAgGe, respectively. (c,d) Broadband *ac* plane Rotation and Ellipticity spectra of HoAgGe, respectively. The spectra were measured with the incoming polarisation along the *c* axis of the crystal. Since for this plane, the Kerr parameters can depend on the polarisation of the incoming electric field as shown in Sec. A.3.3, the MIR spectra at 5 K for light polarised along the *a* axis is shown in black for comparison.



### A.3.3 MOKE with Anisotropic Diagonal Conductivity Tensor Elements

Interestingly, a literature review produced no results in finding an already published derivation for this issue. Therefore, we need to find the equivalent expression for Eq. 1.50 for this case. Much credit for the following derivation goes to Sándor Bordács.

We follow the same scheme as in Sec. 1.3.2, starting with the Maxwell equations to derive the refractive index

$$\left. \begin{aligned} \mathbf{k} \times \mathbf{E} &= \omega \mu_0 \mathbf{H} \\ \mathbf{k} \times \mathbf{H} &= -\omega \varepsilon_0 \hat{\varepsilon} \mathbf{E} \end{aligned} \right\} \rightarrow \mathbf{k} \times (\mathbf{k} \times \mathbf{E}) = \frac{\omega^2}{c^2} \hat{\varepsilon} \mathbf{E}$$

$$\mathbf{k} \cdot \mathbf{E} = 0 \rightarrow k^2 \mathbf{E} = \frac{\omega^2}{c^2} \hat{\varepsilon} \mathbf{E}$$

$$\rightarrow N^2 \mathbf{E} = \hat{\varepsilon} \mathbf{E} \quad (\text{A.3})$$

Using the general form of the dielectric tensor with different diagonal elements

$$\hat{\varepsilon} = \begin{pmatrix} \varepsilon_{xx} & \varepsilon_{xy} \\ -\varepsilon_{xy} & \varepsilon_{yy} \end{pmatrix}, \quad (\text{A.4})$$

we obtain the eigenvalues

$$N_{\pm}^2 = \frac{\varepsilon_{xx} + \varepsilon_{yy}}{2} \pm \sqrt{\left(\frac{\varepsilon_{xx} - \varepsilon_{yy}}{2}\right)^2 - \varepsilon_{xy}^2} \quad (\text{A.5})$$

and eigenvectors

$$\mathbf{s}_{\pm} = \left( \begin{array}{c} -\frac{\varepsilon_{xx} - \varepsilon_{yy} \mp \sqrt{(\varepsilon_{xx} - \varepsilon_{yy})^2 - 4\varepsilon_{xy}^2}}{2\varepsilon_{xy}} \\ 1 \end{array} \right) \rightarrow \hat{\mathbf{s}}_{\pm} = \frac{\mathbf{s}_{\pm}}{|\mathbf{s}_{\pm}|}. \quad (\text{A.6})$$

From this, we can again derive the transformation matrix into the basis of the eigenstates

$$\hat{U} = (\hat{\mathbf{s}}_+ | \hat{\mathbf{s}}_-). \quad (\text{A.7})$$

If the sample is characterised by the reflectivities  $r_{\pm}$  for the two eigenstates, we find that the reflected field is given by

$$\mathbf{E}_{\text{ref}} = \hat{U} \begin{pmatrix} r_+ & 0 \\ 0 & r_- \end{pmatrix} \hat{U}^{-1} \mathbf{E}_{\text{in}}.$$

For an incoming electric field of the form  $\mathbf{E}_{\text{in}} = \begin{pmatrix} 1 \\ 0 \end{pmatrix}$  it holds

$$\mathbf{E}_{\text{ref}} = \begin{pmatrix} \frac{r_-(\varepsilon_{xx} - \varepsilon_{yy} + \sigma) + r_+(-(\varepsilon_{xx} - \varepsilon_{yy}) + \sigma)}{2\sigma} \\ -\frac{\varepsilon_{xy}(r_- - r_+)}{\sigma} \end{pmatrix} \quad (\text{A.8})$$

with  $\sigma = \sqrt{\left(\frac{\varepsilon_{xx} - \varepsilon_{yy}}{2}\right)^2 - \varepsilon_{xy}^2}$ . This yields

$$\phi_x = \frac{r_y}{r_x} = \frac{2\varepsilon_{xy}(r_+ - r_-)}{\sigma(r_+ + r_-) - (\varepsilon_{xx} - \varepsilon_{yy})(r_+ - r_-)} \quad (\text{A.9})$$

if  $\phi_x$  is small. In an analogous fashion, for  $\mathbf{E}_{\text{in}} = \begin{pmatrix} 0 \\ 1 \end{pmatrix}$  we obtain

$$\mathbf{E}_{\text{ref}} = \begin{pmatrix} \frac{\varepsilon_{xy}(r_- - r_+)}{2\sigma} \\ \frac{r_-(-(\varepsilon_{xx} - \varepsilon_{yy}) + \sigma) + r_+(\varepsilon_{xx} - \varepsilon_{yy} + \sigma)}{2\sigma} \end{pmatrix} \quad (\text{A.10})$$

which results in

$$\phi_y = -\frac{-2\varepsilon_{xy}(r_+ - r_-)}{\sigma(r_+ + r_-) + (\varepsilon_{xx} - \varepsilon_{yy})(r_+ - r_-)}, \quad (\text{A.11})$$

where the additional minus sign is used to preserve the sense of rotation. Under the assumptions that the conduction anisotropy is small and that the Hall effect is small compared to the diagonal conductivity, meaning

$$\left| \frac{\varepsilon_{xx} - \varepsilon_{yy}}{2} \right| \ll \left| \frac{\varepsilon_{xx} + \varepsilon_{yy}}{2} \right| \quad \& \quad \varepsilon_{xy} \ll \left| \frac{\varepsilon_{xx} + \varepsilon_{yy}}{2} \right|$$

this expression can be simplified. The refractive indices become

$$N_{\pm} = \sqrt{\frac{\varepsilon_{xx} + \varepsilon_{yy}}{2} \pm \frac{1}{2}\sigma} = \sqrt{\varepsilon \pm \frac{1}{2}\sigma} \approx \sqrt{\varepsilon} \pm \frac{\sigma}{4\sqrt{\varepsilon}} = N \pm \frac{\Delta N}{2} \quad (\text{A.12})$$

With this, we can calculate the reflectivities accordingly

$$\begin{aligned}
r_{\pm} &= \frac{N_{\pm} - 1}{N_{\pm} + 1} = \frac{N \pm \frac{\Delta N}{2} - 1}{N \pm \frac{\Delta N}{2} + 1} = \frac{N - 1 \pm \frac{\Delta N}{2}}{(N + 1) \cdot \left(\frac{\Delta N}{2(N+1)}\right)} \\
&\approx \frac{N - 1}{N + 1} \pm \frac{\Delta N}{2} \frac{1}{N + 1} \mp \frac{\Delta N}{2} \frac{1}{N + 1} \frac{N - 1}{N + 1} \cdots \\
&= \frac{N - 1}{N + 1} \pm \frac{\Delta N}{2(N + 1)} \left(1 - \frac{N - 1}{N + 1}\right) = \frac{N - 1}{N + 1} \pm \frac{\Delta N}{(N + 1)^2} \\
&= \frac{\sqrt{\varepsilon} - 1}{\sqrt{\varepsilon} + 1} \pm \frac{\sigma}{2\sqrt{\varepsilon}(\sqrt{\varepsilon} + 1)^2}.
\end{aligned} \tag{A.13}$$

Finally, we obtain expressions for  $\phi_{x,y}$

$$\begin{aligned}
\phi_{x,y} &= \frac{2\varepsilon_{xy}(r_+ - r_-)}{\sigma(r_+ + r_-) \mp (\varepsilon_{xx} - \varepsilon_{yy})(r_+ - r_-)} \\
&\approx \frac{2\varepsilon_{xy} \cdot 2 \frac{\sigma}{2\sqrt{\varepsilon}(\sqrt{\varepsilon} + 1)^2}}{\sigma \cdot 2 \frac{\sqrt{\varepsilon} - 1}{\sqrt{\varepsilon} + 1} \mp (\varepsilon_{xx} - \varepsilon_{yy}) \cdot 2 \frac{\sigma}{2\sqrt{\varepsilon}(\sqrt{\varepsilon} + 1)^2}} \\
&= \frac{\frac{\varepsilon_{xy}}{\sqrt{\varepsilon}(\sqrt{\varepsilon} + 1)}}{\sqrt{\varepsilon} - 1 \mp \left(\frac{\varepsilon_{xx} - \varepsilon_{yy}}{2}\right) \frac{1}{\sqrt{\varepsilon}(\sqrt{\varepsilon} + 1)}} \\
&= \frac{\varepsilon_{xy}}{\sqrt{\varepsilon}(\varepsilon - 1) \mp \left(\frac{\varepsilon_{xx} - \varepsilon_{yy}}{2}\right)} \\
&= \frac{\varepsilon_{xy}}{\sqrt{\frac{\varepsilon_{xx} + \varepsilon_{yy}}{2} \left(\frac{\varepsilon_{xx} + \varepsilon_{yy}}{2} - 1\right) \mp \left(\frac{\varepsilon_{xx} - \varepsilon_{yy}}{2}\right)}}
\end{aligned} \tag{A.14}$$

Comparing with Eq. 1.49, the Kerr parameters now depend on the average and the difference of the diagonal elements. Hence, if we set  $\varepsilon_{xx} = \varepsilon_{yy}$ , we always recover the case for identical diagonal tensor elements during the above considerations, which validates the made assumptions.

When replacing the dielectric function with the conductivity by  $\varepsilon_{\alpha\beta} = \delta_{\alpha\beta} + \frac{i}{\varepsilon_0\omega} \sigma_{\alpha\beta}$ , this yields

### Anisotropic Kerr effect

$$\phi_{x,y} = - \frac{\sigma_{xy}}{\frac{\sigma_{xx} + \sigma_{yy}}{2} \sqrt{1 + \frac{i}{\varepsilon_0\omega} \frac{\sigma_{xx} + \sigma_{yy}}{2}} \pm \frac{\sigma_{xx} - \sigma_{yy}}{2}}, \tag{A.15}$$

enabling the calculation of the off-diagonal conductivity from the Kerr-parameters and the diagonal conductivity. Importantly, we directly obtain Eq. 1.50 if we set the diagonal elements equal.

As a result, in the anisotropic case, the Kerr parameters will be different depending on the alignment of the incoming electric field within the  $ac$  plane. Therefore, Fig. A.2(c,d) shows the Kerr parameters with the incoming light polarised along the  $c$  axis of the crystal. Since a PEM is used for the measurement, this refers to the  $45^\circ$  polarisation aligned with the crystallographic axis. For comparison, the 5 K MIR spectrum for light polarised along the  $a$  axis is shown additionally. The spectra were obtained on a polished  $ac$  cut crystal with useful aperture of 1.4 mm. The most prominent features observed in the spectra are two peaks in the ellipticity at 0.25 and 0.6 eV with peak magnitude of  $-0.03^\circ$ , respectively. While their magnitude increases upon lowering the temperature, the

onset of these features is already visible at 40 K, which is far above the magnetic ordering temperature. Due to the antiferromagnetic nature of the ground state order and the small magnetic fields, these signals are obtained due to a small polarisation of the magnetic moments by the external field, which appears not to be significantly influenced by the magnetic ordering. It would be interesting to observe the evolution of these features when the metamagnetic transitions occur at higher fields, which triggered the development of a high-field MOKE setup at BME, which at present is not completed. We therefore cannot evaluate the evolution of the optical Hall conductivity across the metamagnetic states at this stage.

### A.3.4 ab cut with $\mathbf{H} \parallel \mathbf{c}$

The magnetic space-group of HoAgGe below the first metamagnetic transition at 11.6 K is  $-6'_2m_{xz}2'_x$  [103]. Considering  $x \parallel a$ ,  $y \parallel b$  and  $z \parallel c$ , if we additionally include a magnetic field along the  $c$  axis, some of these symmetries are broken, resulting in the space-group  $3_z2'_x$ . The threefold-rotation can be represented by

$$C_3^z = \begin{pmatrix} -\frac{1}{2} & -\frac{\sqrt{3}}{2} & 0 \\ \frac{\sqrt{3}}{2} & -\frac{1}{2} & 0 \\ 0 & 0 & 1 \end{pmatrix}$$

Due to Neumann's principle [41], the dielectric tensor must fulfil  $\hat{\varepsilon} = C_3^z \hat{\varepsilon} (C_3^z)^{-1}$ , consequently

$$\begin{pmatrix} \varepsilon_{xx} & \varepsilon_{xy} & \varepsilon_{xz} \\ \varepsilon_{yx} & \varepsilon_{yy} & \varepsilon_{yz} \\ \varepsilon_{zx} & \varepsilon_{zy} & \varepsilon_{zz} \end{pmatrix} = \frac{1}{4} \begin{pmatrix} \varepsilon_{xx} + \sqrt{3}(\varepsilon_{yx} + \varepsilon_{xy}) + 3\varepsilon_{yy} & \varepsilon_{xy} + \sqrt{3}(\varepsilon_{xx} - \varepsilon_{yy}) - 3\varepsilon_{yx} & -\varepsilon_{xz} - \sqrt{3}\varepsilon_{yz} \\ \varepsilon_{yx} + \sqrt{3}(\varepsilon_{yy} - \varepsilon_{xx}) - 3\varepsilon_{xy} & \varepsilon_{yy} - \sqrt{3}(\varepsilon_{xy} + \varepsilon_{yx}) + 3\varepsilon_{xx} & -\varepsilon_{yz} - \sqrt{3}\varepsilon_{xz} \\ -\varepsilon_{zx} - \sqrt{3}\varepsilon_{zy} & -\varepsilon_{zy} - \sqrt{3}\varepsilon_{zx} & 4\varepsilon_{zz} \end{pmatrix}.$$

This equation can be fulfilled if

$$\begin{aligned} \varepsilon_{xx} &= \varepsilon_{yy} \\ \varepsilon_{xy} &= -\varepsilon_{yx} \\ \varepsilon_{zx} &= \varepsilon_{zy} = 0 \\ \varepsilon_{xz} &= \varepsilon_{yz} = 0, \end{aligned}$$

leading to

$$\hat{\varepsilon} = \begin{pmatrix} \varepsilon_{xx} & \varepsilon_{xy} & 0 \\ -\varepsilon_{xy} & \varepsilon_{xx} & 0 \\ 0 & 0 & \varepsilon_{zz} \end{pmatrix}. \quad (\text{A.16})$$

The twofold rotation represented by

$$C_2^x = \begin{pmatrix} 1 & 0 & 0 \\ 0 & -1 & 0 \\ 0 & 0 & -1 \end{pmatrix}$$

including time-reversal ( $'$ ) leads to

$$\begin{pmatrix} \varepsilon_{xx} & \varepsilon_{xy} & 0 \\ -\varepsilon_{xy} & \varepsilon_{xx} & 0 \\ 0 & 0 & \varepsilon_{zz} \end{pmatrix} = \begin{pmatrix} \varepsilon'_{xx} & -\varepsilon'_{xy} & 0 \\ \varepsilon'_{xy} & \varepsilon'_{xx} & 0 \\ 0 & 0 & \varepsilon'_{zz} \end{pmatrix}. \quad (\text{A.17})$$

The last equivalence is obtained through the Onsager relations for reversibility in linear response theory [53]. In order to fulfil this equation, the diagonal elements have to be symmetric under time-reversal (S) while the off-diagonal elements are antisymmetric (A), so finally

$$\hat{\varepsilon} = \begin{pmatrix} \varepsilon_{xx}^S & \varepsilon_{xy}^A & 0 \\ -\varepsilon_{xy}^A & \varepsilon_{xx}^S & 0 \\ 0 & 0 & \varepsilon_{zz}^S \end{pmatrix}. \quad (\text{A.18})$$

Therefore, for light propagation along the  $c$  axis, we obtain the same expression for the MOKE parameters as in Sec. 1.3.2.

### A.3.5 ac cut with $\mathbf{H} \parallel \mathbf{b}$

Here we apply a magnetic field along the  $b$  axis of the crystal. For this configuration, all kinds of magnetic order present in HoAgGe have the same magnetic space-group of  $m'_{xy}m_{xz}2'_x$  [103]. Applying a magnetic field along the  $b$  axis of the crystal thus does not lead to any new constraints. Representing  $m_{xz}$  by

$$m_{xz} = \begin{pmatrix} 1 & 0 & 0 \\ 0 & -1 & 0 \\ 0 & 0 & 1 \end{pmatrix}$$

Neumann's principle leads to

$$\begin{pmatrix} \varepsilon_{xx} & \varepsilon_{xy} & \varepsilon_{xz} \\ \varepsilon_{yx} & \varepsilon_{yy} & \varepsilon_{yz} \\ \varepsilon_{zx} & \varepsilon_{zy} & \varepsilon_{zz} \end{pmatrix} = \begin{pmatrix} \varepsilon_{xx} & -\varepsilon_{xy} & \varepsilon_{xz} \\ -\varepsilon_{yx} & \varepsilon_{yy} & -\varepsilon_{yz} \\ \varepsilon_{zx} & -\varepsilon_{zy} & \varepsilon_{zz} \end{pmatrix}$$

resulting in

$$\varepsilon_{xy} = \varepsilon_{yx} = \varepsilon_{zy} = \varepsilon_{yz} = 0,$$

which produces

$$\hat{\varepsilon} = \begin{pmatrix} \varepsilon_{xx} & 0 & \varepsilon_{xz} \\ 0 & \varepsilon_{yy} & 0 \\ \varepsilon_{zx} & 0 & \varepsilon_{zz} \end{pmatrix}. \quad (\text{A.19})$$

Similarly, with

$$m_{xy} = \begin{pmatrix} 1 & 0 & 0 \\ 0 & 1 & 0 \\ 0 & 0 & -1 \end{pmatrix}$$

we obtain for  $m'_{xy}$

$$\begin{pmatrix} \varepsilon_{xx} & 0 & \varepsilon_{xz} \\ 0 & \varepsilon_{yy} & 0 \\ \varepsilon_{zx} & 0 & \varepsilon_{zz} \end{pmatrix} = \begin{pmatrix} \varepsilon'_{xx} & 0 & -\varepsilon'_{xz} \\ 0 & \varepsilon'_{yy} & 0 \\ -\varepsilon'_{zx} & 0 & \varepsilon'_{zz} \end{pmatrix}$$

yielding,

$$\hat{\varepsilon} = \begin{pmatrix} \varepsilon_{xx}^S & 0 & \varepsilon_{xz}^A \\ 0 & \varepsilon_{yy}^S & 0 \\ \varepsilon_{zx}^A & 0 & \varepsilon_{zz}^S \end{pmatrix}. \quad (\text{A.20})$$

The twofold axis does not add any new constraints, so with time-reversal requiring that  $\varepsilon_{zx} = -\varepsilon_{xz}$  [53], we finally obtain:

$$\hat{\varepsilon} = \begin{pmatrix} \varepsilon_{xx}^S & 0 & \varepsilon_{xz}^A \\ 0 & \varepsilon_{yy}^S & 0 \\ -\varepsilon_{xz}^A & 0 & \varepsilon_{zz}^S \end{pmatrix}. \quad (\text{A.21})$$

Therefore, when light is propagating along the  $b$  axis of the crystal, the effective dielectric tensor has anisotropic diagonal elements for the Faraday and Kerr effect.



## References

- [1] C. K. Chiu et al., “Classification of topological quantum matter with symmetries”, *Reviews of Modern Physics* **88**, 035005 (2016).
- [2] D. J. Thouless et al., “Quantized Hall Conductance in a Two-Dimensional Periodic Potential”, *Physical Review Letters* **49**, 405–408 (1982).
- [3] N. Nagaosa et al., “Anomalous Hall effect”, *Reviews of Modern Physics* **82**, 1539 (2010).
- [4] P. Bruno, V. K. Dugaev, and M. Taillefumier, “Topological Hall effect and Berry phase in magnetic nanostructures”, *Physical Review Letters* **93**, 1–4 (2004).
- [5] M. G. Vergniory et al., “A complete catalogue of high-quality topological materials”, *Nature* **566**, 480–485 (2019).
- [6] M. J. Gilbert, “Topological electronics”, *Communications Physics* **4**, 1–12 (2021).
- [7] M. Z. Hasan and C. L. Kane, “Colloquium : Topological insulators”, *Reviews of Modern Physics* **82**, 3045–3067 (2010).
- [8] J. X. Yin, B. Lian, and M. Z. Hasan, “Topological kagome magnets and superconductors”, *Nature* **612**, 647–657 (2022).
- [9] N. P. Armitage, E. J. Mele, and A. Vishwanath, “Weyl and Dirac semimetals in three-dimensional solids”, *Reviews of Modern Physics* **90**, 015001 (2018).
- [10] R. Ilan, A. G. Grushin, and D. I. Pikulin, “Pseudo-electromagnetic fields in 3D topological semimetals”, *Nature Reviews Physics* **2**, 29–41 (2020).
- [11] K. Ohgushi, S. Murakami, and N. Nagaosa, “Spin anisotropy and quantum Hall effect in the kagomé lattice: Chiral spin state based on a ferromagnet”, *Physical Review B* **62**, R6065 (2000).
- [12] A. A. Burkov and L. Balents, “Weyl semimetal in a topological insulator multilayer”, *Physical Review Letters* **107**, 127205 (2011).
- [13] J. K. Asbóth, L. Oroszlány, and A. Pályi, *A Short Course on Topological Insulators*, Vol. 919, Lecture Notes in Physics (Springer International Publishing, Cham, 2016).
- [14] H. Weyl, “Gravitation and the Electron”, *Proceedings of the National Academy of Sciences* **15**, 323–334 (1929).
- [15] H. Nielsen and M. Ninomiya, “Absence of neutrinos on a lattice”, *Nuclear Physics B* **185**, 20–40 (1981).

- [16] M. Kang et al., “Topological flat bands in frustrated kagome lattice CoSn”, *Nature Communications* **11**, 1–9 (2020).
- [17] B. R. Ortiz et al., “CsV<sub>3</sub>Sb<sub>5</sub>: A Z<sub>2</sub> Topological Kagomé Metal with a Superconducting Ground State”, *Physical Review Letters* **125**, 247002 (2020).
- [18] S. Howard et al., “Evidence for one-dimensional chiral edge states in a magnetic Weyl semimetal Co<sub>3</sub>Sn<sub>2</sub>S<sub>2</sub>”, *Nature Communications* **12**, 4269 (2021).
- [19] D. L. Bergman, C. Wu, and L. Balents, “Band touching from real-space topology in frustrated hopping models”, *Physical Review B* **78**, 125104 (2008).
- [20] L. Ye et al., “Massive Dirac fermions in a ferromagnetic kagome metal”, *Nature* **555**, 638–642 (2018).
- [21] Z. Wang and P. Zhang, “Edge states and the integer quantum Hall conductance in spin-chiral ferromagnetic kagomé lattice”, *Physical Review B* **77**, 125119 (2008).
- [22] M. V. Berry, “Quantal Phase Factors Accompanying Adiabatic Changes”, *Proceedings of the Royal Society of London* **392**, 45–57 (1984).
- [23] D. Xiao, M.-C. Chang, and Q. Niu, “Berry phase effects on electronic properties”, *Rev. Mod. Phys.* **82**, 1959 (2010).
- [24] C. Z. Chang et al., “Experimental observation of the quantum anomalous Hall effect in a magnetic topological insulator”, *Science* **340**, 167–170 (2013).
- [25] A. A. Burkov, “Weyl Metals”, *Annual Review of Condensed Matter Physics* **9**, 359–378 (2018).
- [26] S. Fang et al., “Ferromagnetic helical nodal line and Kane-Mele spin-orbit coupling in kagome metal Fe<sub>3</sub>Sn<sub>2</sub>”, *Physical Review B* **105**, 035107 (2022).
- [27] A. A. Burkov, M. D. Hook, and L. Balents, “Topological nodal semimetals”, *Physical Review B - Condensed Matter and Materials Physics* **84**, 235126 (2011).
- [28] M. A. Wilde et al., “Symmetry-enforced topological nodal planes at the Fermi surface of a chiral magnet”, *Nature* **594**, 374–379 (2021).
- [29] E. Hall, “On the new action of magnetism on a permanent electric current”, *The London, Edinburgh, and Dublin Philosophical Magazine and Journal of Science* **10**, 301–328 (1880).
- [30] J. Smit, “The Spontaneous Hall Effect in Ferromagnets II”, *Physica (Amsterdam)* **24**, 39–51 (1958).

- [31] L. Berger, “Side-jump mechanism for the Hall effect of ferromagnets”, [Physical Review B](#) **2**, 4559 (1970).
- [32] R. Karplus and J. M. Luttinger, “Hall effect in ferromagnetics”, [Physical Review](#) **95**, 1154 (1954).
- [33] Y. Tian, L. Ye, and X. Jin, “Proper scaling of the anomalous Hall effect”, [Physical Review Letters](#) **103**, 087206 (2009).
- [34] Y. Pu et al., “Mott relation for anomalous Hall and Nernst effects in  $\text{Ga}_{1-x}\text{Mn}_x\text{As}$  ferromagnetic semiconductors”, [Physical Review Letters](#) **101**, 117208 (2008).
- [35] M. Kargarian, M. Randeria, and N. Trivedi, “Theory of Kerr and Faraday rotations and linear dichroism in Topological Weyl Semimetals”, [Scientific Reports](#) **5**, 12683 (2015).
- [36] K. Sonowal, A. Singh, and A. Agarwal, “Giant optical activity and Kerr effect in type-I and type-II Weyl semimetals”, [Physical Review B](#) **100**, 085436 (2019).
- [37] J. F. Steiner, A. V. Andreev, and D. A. Pesin, “Anomalous Hall effect in Type-I Weyl metals”, [Physical Review Letters](#) **119**, 036601 (2017).
- [38] A. A. Burkov, “Anomalous Hall Effect in Weyl Metals”, [Physical Review Letters](#) **113**, 187202 (2014).
- [39] S. Iguchi et al., “Optical probe for anomalous hall resonance in ferromagnets with spin chirality”, [Physical Review Letters](#) **103**, 267206 (2009).
- [40] T. S. Seifert et al., “Frequency-Independent Terahertz Anomalous Hall Effect in  $\text{DyCo}_5$ ,  $\text{Co}_{32}\text{Fe}_{68}$ , and  $\text{Gd}_{27}\text{Fe}_{73}$  Thin Films from DC to 40 THz”, [Advanced Materials](#) **33**, 2007398 (2021).
- [41] F. E. Neumann, *Vorlesungen über mathematische Physik: 5. Vorlesungen über die Theorie der Elasticität der festen Körper und des Lichtäthers* (Teubner, gehalten an der Universität Königsberg, 1885).
- [42] K. Shinagawa, “Faraday and Kerr Effects in Ferromagnets”, in *Magneto-optics*, edited by S. Sugano and N. Kojima (Springer Berlin Heidelberg, Berlin, Heidelberg, 2000), pp. 137–177.
- [43] J. Kerr, “On rotation of the plane of polarization by reflection from the pole of a magnet”, [The London, Edinburgh, and Dublin Philosophical Magazine and Journal of Science](#) **3**, 321–343 (1877).
- [44] V. Antonov, B. Harmon, and A. Yaresko, *Electronic Structure and Magneto-Optical Properties of Solids* (Kluwer Academic Publishers, Dordrecht, 2004).
- [45] S. Wittekoek et al., “Magneto-optic spectra and the dielectric tensor elements of bismuth-substituted iron garnets at photon energies between 2.2-5.2 eV”, [Physical Review B](#) **12**, 2777 (1975).

- [46] F. J. Kahn, P. S. Pershan, and J. P. Remeika, “Ultraviolet magneto-optical properties of single-crystal orthoferrites, garnets, and other ferric oxide compounds”, *Physical Review* **186**, 891 (1969).
- [47] H. Kuzmany, *Solid-State Spectroscopy* (Springer International Publishing, 2009).
- [48] P. O. Nilsson and L. Munkby, “Investigation of errors in the Kramers-Kronig analysis of reflectance data”, *Physik der Kondensierten Materie* **10**, 290–298 (1969).
- [49] Oriel Instruments, *Cornerstone™ 260, User’s Manual* (2015).
- [50] Bruker Optik GmbH, *Vertex 80v User Manual*, 2nd ed. (Ettlingen, 2013).
- [51] P. R. Griffiths and J. A. De Haseth, *Fourier Transform Infrared Spectrometry*, Vol. 171 (John Wiley & Sons, Inc., Hoboken, NJ, USA, 2007).
- [52] K. Sato, “Measurement of Magneto-Optical Kerr Effect Using Piezo-Birefringent Modulator”, *Japanese Journal of Applied Physics* **20**, 2403–2409 (1981).
- [53] A. Lakhtakia and R. A. Depine, “On Onsager relations and linear electromagnetic materials”, *AEU - International Journal of Electronics and Communications* **59**, 101–104 (2005).
- [54] A. B. Kuzmenko, “Kramers-Kronig constrained variational analysis of optical spectra”, *Review of Scientific Instruments* **76**, 1–9 (2005).
- [55] M. Zabel, S. Wandering, and K.-J. Range, “Ternary Chalcogenides  $M_3M'_2X_2$  with Shandite-Type Structure”, *Z. Naturforsch.* **34b**, 238–241 (1979).
- [56] M. A. Kassem et al., “Low-field anomalous magnetic phase in the kagome-lattice shandite  $Co_3Sn_2S_2$ ”, *Physical Review B* **96**, 014429 (2017).
- [57] Z. Guguchia et al., “Tunable anomalous Hall conductivity through volume-wise magnetic competition in a topological kagome magnet”, *Nature Communications* **11**, 1–9 (2020).
- [58] J. R. Soh et al., “Magnetic structure of the topological semimetal  $Co_3Sn_2S_2$ ”, *Physical Review B* **105**, 094435 (2022).
- [59] C. Lee et al., “Observation of a phase transition within the domain walls of ferromagnetic  $Co_3Sn_2S_2$ ”, *Nature Communications* **13**, 6–11 (2022).
- [60] Q. Wang et al., “Large intrinsic anomalous Hall effect in half-metallic ferromagnet  $Co_3Sn_2S_2$  with magnetic Weyl fermions”, *Nature Communications* **9**, 3681 (2018).
- [61] S. Minami et al., “Enhancement of the transverse thermoelectric conductivity originating from stationary points in nodal lines”, *Physical Review B* **102**, 205128 (2020).

- [62] F. Schilberth et al., “Nodal-line resonance generating the giant anomalous Hall effect of  $\text{Co}_3\text{Sn}_2\text{S}_2$ ”, *Physical Review B* **107**, 214441 (2023).
- [63] I. Belopolski et al., “Signatures of Weyl Fermion Annihilation in a Correlated Kagome Magnet”, *Physical Review Letters* **127**, 256403 (2021).
- [64] D. F. Liu et al., “Magnetic Weyl semimetal phase in a Kagomé crystal”, *Science* **365**, 1282–1285 (2019).
- [65] E. Liu et al., “Giant anomalous Hall effect in a ferromagnetic kagome-lattice semimetal”, *Nature Physics* **14**, 1125–1132 (2018).
- [66] Y. Okamura et al., “Giant magneto-optical responses in magnetic Weyl semimetal  $\text{Co}_3\text{Sn}_2\text{S}_2$ ”, *Nature Communications* **11**, 4619 (2020).
- [67] M. Holder et al., “Photoemission study of electronic structure of the half-metallic ferromagnet  $\text{Co}_3\text{Sn}_2\text{S}_2$ ”, *Physical Review B - Condensed Matter and Materials Physics* **79**, 205116 (2009).
- [68] M. A. Kassem et al., “Single crystal growth and characterization of kagomé-lattice shandites  $\text{Co}_3\text{Sn}_{2-x}\text{In}_x\text{S}_2$ ”, *Journal of Crystal Growth* **426**, 208–213 (2015).
- [69] R. Yang et al., “Magnetization-Induced Band Shift in Ferromagnetic Weyl Semimetal  $\text{Co}_3\text{Sn}_2\text{S}_2$ ”, *Physical Review Letters* **124**, 077403 (2020).
- [70] D. Y. Smith, “Superconvergence and sum rules for the optical constants: natural and magneto-optical activity”, *Physical Review B* **13**, 5303–5315 (1976).
- [71] Y. Xu et al., “Electronic correlations and flattened band in magnetic Weyl semimetal candidate  $\text{Co}_3\text{Sn}_2\text{S}_2$ ”, *Nature Communications* **11**, 3985 (2020).
- [72] I. Kézsmárki et al., “Separation of orbital contributions to the optical conductivity of  $\text{BaVS}_3$ ”, *Physical Review Letters* **96**, 186402 (2006).
- [73] C. J. Tabert and J. P. Carbotte, “Optical conductivity of weyl semimetals and signatures of the gapped semimetal phase transition”, *Physical Review B* **93**, 085442 (2016).
- [74] C. Fang et al., “Topological nodal line semimetals”, *Chinese Physics B* **25**, 1–10 (2016).
- [75] M. P. Ghimire et al., “Creating weyl nodes and controlling their energy by magnetization rotation”, *Physical Review Research* **1**, 032044 (2019).
- [76] J.-X. Yin et al., “Giant and anisotropic many-body spin-orbit tunability in a strongly correlated kagome magnet”, *Nature* **562**, 91–95 (2018).
- [77] A. H. Mayo et al., “Magnetic Generation and Switching of Topological Quantum Phases in a Trivial Semimetal  $\alpha\text{-EuP}_3$ ”, *Physical Review X* **12**, 011033 (2022).

- [78] L. Ye et al., “Field-dependent Shubnikov-de Haas oscillations in ferromagnetic Weyl semimetal  $\text{Co}_3\text{Sn}_2\text{S}_2$ ”, [arXiv:2203.04254](#), 1–6 (2022).
- [79] A. Ozawa and K. Nomura, “Two-orbital effective model for magnetic weyl semimetal in kagome-lattice shandite”, [Journal of the Physical Society of Japan](#) **88**, 123703 (2019).
- [80] F. Schilberth et al., “Generation of Weyl points and a nodal line by magnetization reorientation in  $\text{Co}_3\text{Sn}_2\text{S}_2$ ”, [arXiv:2408.03575](#), 1–12 (2024).
- [81] J. Shen et al., “On the anisotropies of magnetization and electronic transport of magnetic Weyl semimetal  $\text{Co}_3\text{Sn}_2\text{S}_2$ ”, [Applied Physics Letters](#) **115**, 212403 (2019).
- [82] G. Y. Guo and H. Ebert, “Theoretical investigation of the orientation dependence of the magneto-optical Kerr effect in Co”, [Phys. Rev. B](#) **50**, 10377–10380 (1994).
- [83] D.-S. Wang, R. Wu, and A. J. Freeman, “First-principles theory of surface magnetocrystalline anisotropy and the diatomic-pair model”, [Phys. Rev. B](#) **47**, 14932–14947 (1993).
- [84] M.-C. Jiang and G.-Y. Guo, “Large magneto-optical effect and magnetic anisotropy energy in two-dimensional metallic ferromagnet  $\text{Fe}_3\text{GeTe}_2$ ”, [Phys. Rev. B](#) **105**, 014437 (2022).
- [85] H. Takayama, K.-P. Bohnen, and P. Fulde, “Magnetic surface anisotropy of transition metals”, [Phys. Rev. B](#) **14**, 2287–2295 (1976).
- [86] G. Le Caer, B. Malaman, and D. Fruchart, “Magnetic properties of  $\text{Fe}_3\text{Sn}_2$  II. Neutron diffraction study (and Mossbauer effect)”, [Journal of Physics F: Metal Physics Magnetic](#) **8**, 2389 (1978).
- [87] Z. Hou et al., “Observation of Various and Spontaneous Magnetic Skyrmionic Bubbles at Room Temperature in a Frustrated Kagome Magnet with Uniaxial Magnetic Anisotropy”, [Advanced Materials](#) **29**, 1701144 (2017).
- [88] K. Heritage et al., “Images of a First-Order Spin-Reorientation Phase Transition in a Metallic Kagome Ferromagnet”, [Advanced Functional Materials](#) **30**, 1–12 (2020).
- [89] L. A. Fenner, A. A. Dee, and A. S. Wills, “Non-collinearity and spin frustration in the itinerant kagome ferromagnet  $\text{Fe}_3\text{Sn}_2$ ”, [Journal of Physics Condensed Matter](#) **21**, 452202 (2009).
- [90] M. Althaler et al., “Magnetic and geometric control of spin textures in the itinerant kagome magnet  $\text{Fe}_3\text{Sn}_2$ ”, [Physical Review Research](#) **3**, 043191 (2021).
- [91] H. Tanaka et al., “Three-dimensional electronic structure in ferromagnetic  $\text{Fe}_3\text{Sn}_2$  with breathing kagome bilayers”, [Physical Review B](#) **101**, 161114 (2020).

- [92] A. Biswas et al., “Spin-Reorientation-Induced Band Gap in  $\text{Fe}_3\text{Sn}_2$ : Optical Signatures of Weyl nodes”, *Physical Review Letters* **125**, 076403 (2020).
- [93] Z. Lin et al., “Flatbands and Emergent Ferromagnetic Ordering in  $\text{Fe}_3\text{Sn}_2$  Kagome Lattices”, *Physical Review Letters* **121**, 096401 (2018).
- [94] M. Yao et al., “Switchable Weyl nodes in topological Kagome ferromagnet  $\text{Fe}_3\text{Sn}_2$ ”, *arXiv:1810.01514*, 1–19 (2018).
- [95] Q. Wang et al., “Anomalous Hall effect in a ferromagnetic  $\text{Fe}_3\text{Sn}_2$  single crystal with a geometrically frustrated Fe bilayer kagome lattice”, *Physical Review B* **94**, 075135 (2016).
- [96] F. Schilberth et al., “Magneto-optical detection of topological contributions to the anomalous Hall effect in a kagome ferromagnet”, *Physical Review B* **106**, 144404 (2022).
- [97] D. B. Tanner, “Use of x-ray scattering functions in Kramers-Kronig analysis of reflectance”, *Physical Review B* **91**, 035123 (2015).
- [98] H. Feil and C. Haas, “Magneto-Optical Kerr Effect, Enhanced by the Plasma Resonance of Charge Carriers”, *Physical Review Letters* **58**, 65–68 (1987).
- [99] S. A. Ekahana et al., “Anomalous electrons in a metallic kagome ferromagnet”, *Nature* **627**, 67–72 (2024).
- [100] J. Ebad-Allah et al., “Optical anisotropy of the kagome magnet  $\text{FeSn}$ : Dominant role of excitations between kagome and Sn layers”, *Physical Review B* **109**, 1201106 (2024).
- [101] M. Hirschberger et al., “Skyrmion phase and competing magnetic orders on a breathing kagomé lattice”, *Nature Communications* **10**, 5831 (2019).
- [102] E. Morosan et al., “Thermodynamic and transport properties of  $\text{RAgGe}$  ( $\text{R}=\text{Tb-Lu}$ ) single crystals”, *Journal of Magnetism and Magnetic Materials* **277**, 298–321 (2004).
- [103] K. Zhao et al., “Realization of the kagome spin ice state in a frustrated intermetallic compound”, *Science* **367**, 1218–1223 (2020).
- [104] A. S. Wills, R. Ballou, and C. Lacroix, “Model of localized highly frustrated ferromagnetism: The kagomé spin ice”, *Physical Review B - Condensed Matter and Materials Physics* **66**, 1–6 (2002).
- [105] K. Zhao et al., “Discrete degeneracies distinguished by the anomalous Hall effect in a metallic kagome ice compound”, *Nature Physics* **20**, 442–449 (2024).
- [106] N. Li et al., “Low-temperature transport properties of the intermetallic compound  $\text{HoAgGe}$  with a kagome spin-ice state”, *Physical Review B* **106**, 014416 (2022).

- [107] F. Schilberth et al., “Tracing Band Reconstructions across Metamagnetic Transitions in HoAgGe”, in preparation (2024).
- [108] T. Y. Yang et al., “Fermi-level flat band in a kagome magnet”, [Quantum Frontiers](#) **1**, 14 (2022).
- [109] Q. Du et al., “Topological Hall Effect Anisotropy in Kagome Bilayer Metal”, [Phys. Rev. Lett.](#) **129**, 236601 (2022).
- [110] B. C. Sales et al., “Electronic, magnetic, and thermodynamic properties of the kagome layer compound FeSn”, [Physical Review Materials](#) **3**, 114203 (2019).

## Acknowledgements

For the sake of completeness, let me first acknowledge the funding sources enabling this work. The research was supported by the Ministry of Culture and Innovation and the National Research, Development and Innovation Office within the Quantum Information National Laboratory of Hungary (Grant No. 2022-2.1.1-NL-2022-00004) and by the Deutsche Forschungsgemeinschaft (DFG, German Research Foundation) – TRR 360 – 492547816.

Finally, I sincerely hope that all the people I had the pleasure to meet know how grateful I am for the parts they played in creating this piece. So I keep the following short and just say thank you to

- ▷ Sándor and István, for all the small and big things,
- ▷ my colleagues and collaborators, many of whom turned into friends,
- ▷ all the members of the departments, without who no wheels would turn,
- ▷ my family, for love is the basis.